

UNIVERSITY OF CALIFORNIA
Santa Barbara

Synthesis, Characterization and Formation Mechanisms
of Inorganic Nanomaterials.

A Dissertation submitted in partial satisfaction
of the requirements for the degree of:

Doctor of Philosophy
in
Chemistry

by
Gregory A. Khitrov

Committee in charge:
Professor Geoffrey F. Strouse, Chairperson
Professor Peter C. Ford
Professor Steven K. Buratto
Professor William S. Kaska

December, 2003

The Dissertation of Gregory A. Khitrov is approved

Professor William S. Kaska

Professor Steven K. Buratto

Professor Peter C. Ford

Professor Geoffrey F. Strouse, Committee Chairperson

October, 2003

December, 2003

Copyright by

Gregory A. Khitrov

2003

“It is a thrilling ride to be participating as an actor or observer in the scientific revolution of our times, as science enters and transforms the life of man. Some are depressed by the hard work that must be done to make a world, and by the constant threat of failure and catastrophe. Some say philosophy has failed. I think this is only a momentary lapse between the old philosophy and the new one that rises already in the laboratories. I think this century marks in history a revolution of man’s outlook even more profound, if possible, than the accompanying revolution in science and technology. Man has suddenly found himself. He has explored all the earth and stepped outside it. He taps the sun’s source of energy and stands to manipulate the weather and use the oceans. He measures back to the beginning of time and out to the ends of space and sees his own sudden emergence, a thinking creature spun out of light and air and water and holding power in his hand, yet probably only one of millions of such creatures on other worlds.”

-John Rader Platt

from The Excitement of Science

Acknowledgements

My time in Santa Barbara would have been much less productive and enjoyable if it were not for the contributions of the following people.

I'd like to thank my research advisor Geoff Strouse for not giving up on me during the difficult years, for showing me how to think about a problem and, more importantly, when to stop thinking and forge ahead. Your ideas allowed me to rise above the daily grind; I've never lost anything by listening to you.

I'd like to thank the members of the Strouse group for the good company, good conversation and for being there when I needed help both in and out of the lab. Some special thanks are as follows.

Rob – the progenitor of the group's communication style and attitude, which show no signs of fading away. Rohohohooooiiiiight!

Steve – thanks for sharing the rough years, the bars, the Friday afternoons, and pointing out mistakes with the subtlety of a flanged mace.

Jeff – thanks for keeping my legacy alive, just be sure to kill it when the time is right.

Donny – thanks for your sense of humor, and your poignant observations.

Khalid – your approaches to research, driving, humor, and life in general have been nothing less than awe inspiring.

Scott, Orlando, Artjay, Melissa, Mia, Travis, Dan, Gary – I've enjoyed our time together immensely, I'm only sorry I didn't get to know you better (so I could really make fun of you).

I'd like to thank James Pavlovich for letting me occupy the best TA position ever invented, for our numerous discussion of movies, pop culture, and food, and for all your help with the MS instrumentation and data analysis.

I'd like to thank JJ Gaumet for all his help with the cluster MS experiments, the “petunk” games, and the French humor and attitude.

I'd like to thank my family for their faith and support throughout my graduate career even when I was distant and self absorbed.

I'd like to thank my partners in volleyball (Jesse, Grace, Mike, Kurt, Joe, Paul, Thomas, Margaret, Jen, Nancy & Brian, Marcia & Mike, Quian & Fong).for some of the most enjoyable relaxing mornings and evenings I experienced in this town.

Finally, I'd like to thank Professor Ford, Prof. Buratto, Prof. Stucky, and Prof. Kaska of my committee for taking the time to read and comment on my dissertation.

Curriculum Vitae

Education

- University of California, Santa Barbara, California, Ph. D. in Chemistry, Fall 2003. Thesis: Synthesis, characterization and formation mechanisms of semiconductor nanomaterials.
- Eastern Michigan University, Ypsilanti, Michigan, M.S. in Chemistry, June 21, 1996. Thesis: Investigation of restricted valence RSA processes on one dimensional lattices.
- Wayne State University, Detroit, Michigan, B.S. in Chemistry, May 5, 1992.

Work Experience

- 9/00 – present. Teaching assistant. Mass Spectrometry Laboratory, UCSB.
- 9/96 – 9/00 Teaching and research assistant. Department of Chemistry, UCSB.
- 1/95 – 5/96 Teaching assistant. Department of Chemistry, EMU.
- 5/92 – 1/95 Teaching and research assistant. Department of Chemistry, WSU.
- 6/88 – 1/90 Student assistant. Department of Biochemistry, WSU.

Research Skills

- Mass Spectrometric analysis.
 - MALDI – TOF of inorganic nanomaterials.
 - Maintenance and operation of ESI Quadrupole and Quadrupole – TOF instruments.
 - Inorganic molecular clusters.
 - Organic, inorganic, and biological molecules.
- Transmission Electron Microscopy analysis.
 - Nanomaterials
 - Bio-nanomaterial conjugates
- Optical spectroscopic analysis of inorganic nanomaterials.
 - Absorbance
 - Photoluminescence and Photoluminescence excitation.
- Synthesis
 - Inorganic molecular clusters
 - Nanomaterials.
- Theoretical work
 - Non equilibrium statistical thermodynamics system description and calculations.
 - *Ab initio* calculations using the Gaussian 92 program.

- Organizational and teaching skills
 - Teaching general, analytical, and inorganic chemistry laboratory courses.
 - Chair: research group meeting, equipment, student organization.
 - Mentorship of undergraduate researchers (2 yrs).

Honors/Awards

- Special contributor to the Research/Researchers Department of the “MRS Bulletin” May 2000 to present (21 published news items).
- ACS Huron Valley Section Teaching/Research Award for 1996.

Research Publications

1. Study of Gas Phase Fragmentation of the $Ti_6O_4(Ethoxy)_8(Methacrylate)_8$ Molecular Cluster by Electrospray TOF Mass Spectrometry. Khitrov, G. A.; Gaumet, J.J.; Strouse, G.F. *J. Am. Soc. Mass Spectrom.* Accepted Oct. 2003.
2. Mixed Metal Chalcogenide Clusters of $[Co_xCd_ySe_4(SPh)_{16}]^{n\pm}$. Robert W. Meulenberg, Khalid M. Hanif, Gregory A. Khitrov, Jean-Jacques Gaumet, Geoffrey F. Strouse. Manuscript in preparation.
3. II-VI Nanomaterial Characterization by MALDI-TOF Mass Spectrometry. Gregory A. Khitrov, Geoffrey F. Strouse. Manuscript in preparation.
4. ZnS Nanomaterial Characterization by MALDI-TOF Mass Spectrometry. Gregory A. Khitrov, Geoffrey F. Strouse. *J. Am. Chem. Soc.* 2003, *125*, 10465-10469.
5. "Mass Spectrometry Analysis of the 1.5 nm Sphalerite-CdS core of $[Cd_{32}S_{14}(SC_6H_5)_{36}^*DMF_4]$. Gaumet, J.J.; Khitrov, G.A.; Strouse, G.F. *Nano Lett.* 2002, *2*, 375-379.
6. Enzymatic Modulation of DNA-Nanomaterial Constructs. Yun, C.S.; Khitrov, G.A.; Vergona, D.E.; Reich, N.O.; Strouse, G.F. *J. Amer. Chem. Soc.* 2002, *124*, 7644-7645.
7. Inorganic Clusters as Single Source Precursors for Preparation of CdSe, ZnSe, CdSe/ZnS Nanomaterials. Scott L. Cumberland, Khalid M. Hanif, Artjay Javier, Gregory A. Khitrov, Geoffrey F. Strouse, Stephen M. Woessner, C. Steven Yun *Chem. Mater.* 2002, *14*, 1576-1584.
8. The $CF_3C(O)O_2$ radical: Its UV Spectrum, self reaction kinetics, and reaction with NO. M. Matti Maricq, Joseph J. Szenté, Gregory A. Khitrov, Joseph S. Francisco *J. Phys. Chem.* 100, 4514, 1996.
9. CF_3CO Dissociation Kinetics M. Matti Maricq, Joseph J. Szenté, Gregory A. Khitrov, Theodore S. Dibble, Joseph S. Francisco *J. Phys. Chem.* 99, 11875, 1995.

10. Temperature dependent kinetics of the formation and self reactions of FC(O)O_2 and FC(O)O radicals. M. Matti Maricq, Joseph J. Szente, Gregory A. Khitrov, Joseph S. Francisco *J. Chem. Phys.* 98, 9522, 1993.
11. An examination of the structure and inversion barrier for lithium and sodium phosphide. Gregory A. Khitrov, Joseph S. Francisco *Chem. Phys.* 17, 153, 1993
12. FCO: UV spectrum, self reaction kinetics and chain reaction with F_2 . Joseph J. Szente, Gregory A. Khitrov, Joseph S. Francisco *Chem. Phys. Lett.* 199, 71, 1992.

Research Presentations

1. Characterization of a Titanium Oxide Molecular Cluster by Electrospray TOF Mass Spectrometry. Khitrov, G. A.; Gaumet, J.J.; Strouse, G.F. Poster presentation at the 51st ASMS Conference. June 8-12, 2003.
2. ZnS Nanomaterial Characterization by MALDI-TOF Mass Spectrometry. Gregory A. Khitrov, Geoffrey F. Strouse. Poster presentation at the Spring 2002 meeting of the Materials Research Society. April 1- 5, 2002.
3. Novel synthesis of II-VI semiconductor nanocrystals. Gregory A. Khitrov, Geoffrey F. Strouse. Contributed paper at the “New Methods in Solid State Chemistry” symposium at the 219th National Meeting of the American Chemical Society. March 26-30, 2000.
4. Novel synthesis of II-VI semiconductor nanocrystals. Gregory A. Khitrov, Geoffrey F. Strouse. Poster presentation at the Fall 1999 meeting of the Materials Research Society. November 29- December 3, 1999.
5. Investigation of restricted valence RSA processes on one dimensional lattices. Gregory A. Khitrov, Ross S. Nord. Contributed paper (20 minute oral presentation) at the 29th Annual Great Lakes Regional Meeting of the ACS. May 19 - 22, 1996.
6. CF_3CO and $\text{CF}_3\text{C(O)O}_2$ reaction kinetics. M. Matti Maricq, Joseph J. Szente, Gregory A. Khitrov, Theodore S. Dibble, Joseph S. Francisco Poster presentation at the Regional ACS Meeting in Ann Arbor, Michigan in June 1994.

ABSTRACT

Synthesis, Characterization and Formation Mechanisms of Inorganic Nanomaterials.

By

Gregory A. Khitrov

We describe a synthesis of inorganic semiconductor nanomaterials by lyothermal degradation of a single source precursor cluster that provides both a seed nucleus to act as a structural template of the individual nanocrystals and a source of active species for their growth to the desired size.. We also describe a powerful mass spectrometric analytical method for rapid and accurate determination of the average size and size distribution of the resulting nanomaterial sample. Finally, we present a mass spectrometric method for investigating the chemistry of the transition between the precursor and product systems.

Inorganic semiconductor nanomaterials consist of a nano sized inorganic core and an organic passivating layer. The nano sized core endows these materials with useful optical and electronic properties and potential applications in device technology. The single source precursor based synthetic approach allows for controlled growth of high quality nanomaterials using safe and inexpensive starting materials. It is believed that the core of the precursor clusters forms a nucleation site, and the cluster degradation in the coordinating solvent provides a source of active species for nanomaterial growth.

The average size and size distributions of these materials can then be determined by matrix assisted laser desorption ionization mass spectrometry (MALDI-MS) characterization in much the same manner as for a large polymer or biomolecule. The MS approach allows the determination of these critical values in less time and with potentially higher accuracy than the TEM and pXRD methods currently in use.

The fragmentation mechanism of the molecular clusters in coordinating solvent that leads to nanomaterial formation can be investigated by electrospray MS, or ESMS by identifying the species in solution and controllably fragmenting them to determine their structure. The fragmentation pattern elucidated by this study provides insight into the mechanism of nanomaterial formation allowing the synthetic method to be understood and further optimized. The experiments also establish the ESMS analytical method as a viable tool in the investigation of molecular cluster to nanocrystal conversion.

Table of Contents

| | |
|--|----|
| Chapter 1. General Introduction | 1 |
| 1.1 Introduction | 1 |
| 1.2 Nanomaterials Synthesis | 2 |
| 1.2.1 Background information | 2 |
| 1.2.2 Arrested precipitation methods | 8 |
| 1.2.3 Lyothermal methods | 10 |
| 1.2.4 Molecular cluster precursor method | 14 |
| 1.3 Size and size dispersity analysis by MALDI-MS | 16 |
| 1.4 Inorganic molecular cluster degradation by ESI-MS | 18 |
| 1.5 References | 23 |
| | |
| Chapter 2. Synthesis of CdSe, ZnSe, and CdSe/ZnS Nanomaterials | 32 |
| 2.1 Introduction | 32 |
| 2.2 Experimental | 33 |
| 2.3 Results | 37 |
| 2.3.1 Synthesis and characterization | 37 |
| 2.3.2 Reaction mechanism | 45 |
| 2.4 Discussion | 58 |
| 2.4.1 Nanomaterial growth | 58 |
| 2.4.2 Mechanisms for growth | 68 |
| 2.5 Conclusion | 72 |
| 2.6 References | 73 |
| | |
| Chapter 3. Synthesis of CdS and ZnS Nanomaterials | 77 |
| 3.1 Introduction | 77 |
| 3.2 Experimental | 77 |
| 3.3 Results | 79 |

| | |
|--|-----|
| 3.4 Discussion | 84 |
| 3.5 Conclusion | 85 |
| 3.6 References | 87 |
| | |
| Chapter 4. Nanomaterial Characterization by MALDI-TOF MS | 88 |
| 4.1 Introduction | 88 |
| 4.2 Experimental | 89 |
| 4.3 Results | 91 |
| 4.3.1 ZnS | 91 |
| 4.3.2 CdSe and CdSe/ZnS | 98 |
| 4.4 Discussion | 108 |
| 4.4.1 ZnS | 108 |
| 4.4.2 CdSe and CdSe/ZnS | 114 |
| 4.5 Conclusion | 119 |
| 4.6 References | 120 |
| | |
| Chapter 5. Characterization of $\text{Ti}_6\text{O}_4(\text{EtO})_8(\text{McO})_8$ by ESI-TOF MS | 121 |
| 5.1 Introduction | 121 |
| 5.2 Experimental | 122 |
| 5.3 Results | 123 |
| 5.4 Discussion | 135 |
| 5.4.1 General comments | 135 |
| 5.4.2 Mass spectrum at +30 V | 136 |
| 5.4.3 Mass spectrum at +50 V | 138 |
| 5.4.4 Mass spectrum at +100 V | 140 |
| 5.4.5 MS analysis in non-coordinating solvent mixture | 143 |
| 5.5 Conclusion | 144 |
| 5.6 References | 145 |

Chapter 1. General introduction.

1.1 Introduction.

Inorganic semiconductor nanomaterials have been extensively investigated over the past two decades due to their novel optical and electronic properties and potential applications in device technology. This thesis describes novel approaches to the synthesis and characterization of nanocrystalline semiconductor materials. The first part of the thesis presents a single source precursor based approach towards the seeded growth of these materials (Chapters 2 – 3). It is believed that the core of these clusters forms a nucleation site, and the degradation of these clusters in the coordinating solvent provides a source of active species for nanomaterial growth. This method allows for controlled growth of high quality nanomaterials using safe and inexpensive starting materials. The second part of the thesis presents a matrix assisted laser desorption ionization mass spectrometry (MALDI-MS) characterization method by which the size and size distribution of the prepared nanocrystals may be determined (Chapter 4). This approach allows the determination of these critical values in less time and with higher accuracy than the TEM and pXRD methods currently in use. The third part of this thesis presents an investigation of the fragmentation mechanism of molecular clusters in coordinating solvent by electrospray MS, or ESMS (Chapter 5). The cluster fragmentation pattern elucidated by this study provides insight into the mechanism of nanomaterial formation allowing the synthetic method to be understood and optimized. The

experiments also establish the ESMS analytical method as a viable tool in the investigation of molecular cluster to nanocrystal conversion.

1.2 Nanomaterials Synthesis.

1.2.1 Background information.

Semiconductor nanomaterials consist of nano sized (1-100 nm) fragments of a bulk lattice (Figure 1.1) and occupy the size regime between molecular and bulk materials. While the electronic structure of these materials consists of a valence and conduction band, and is similar to that of the bulk lattice, the small size of the semiconductor lattice results in quantum confinement effects which are strongly size dependent. This size dependence allows the optical and electronic properties of nanomaterials to be accurately controlled simply by varying their size only (Figure 1.2); unlike bulk materials whose composition must be varied to achieve the same effect. Thus, quantum confinement adds another dimension to the engineering of semiconductor materials, and results in substantial interest for their applications in device technologies. Potential applications of nanomaterials have been found in the broad areas of biological labels, catalysis, energy conversion, and magnetic recording media.¹⁻² To fully exploit these materials, their optical and electronic properties must be understood. The large strides in understanding these physical

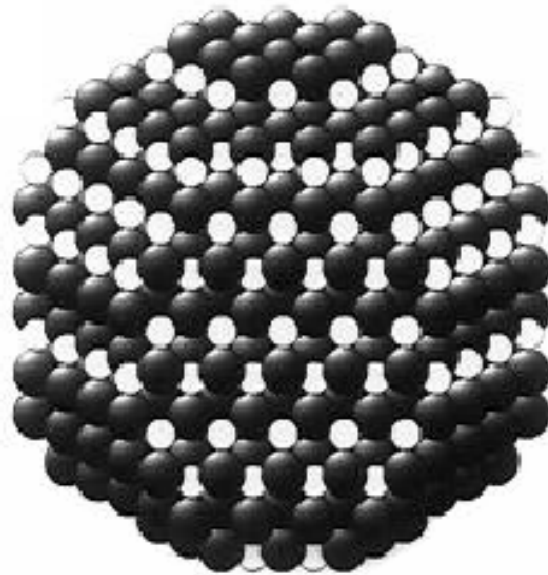


Figure 1.1. Model of a single nanocrystal core. Light and dark spheres represent different atoms.

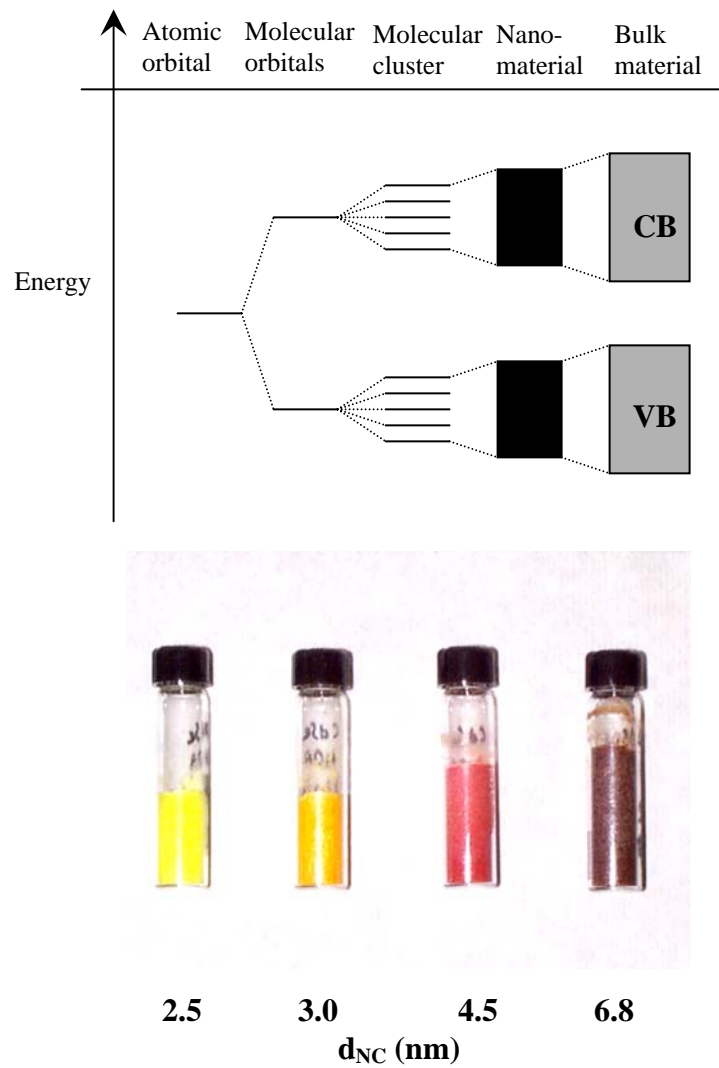
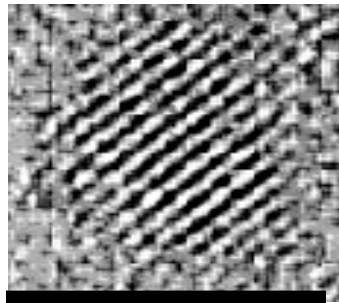
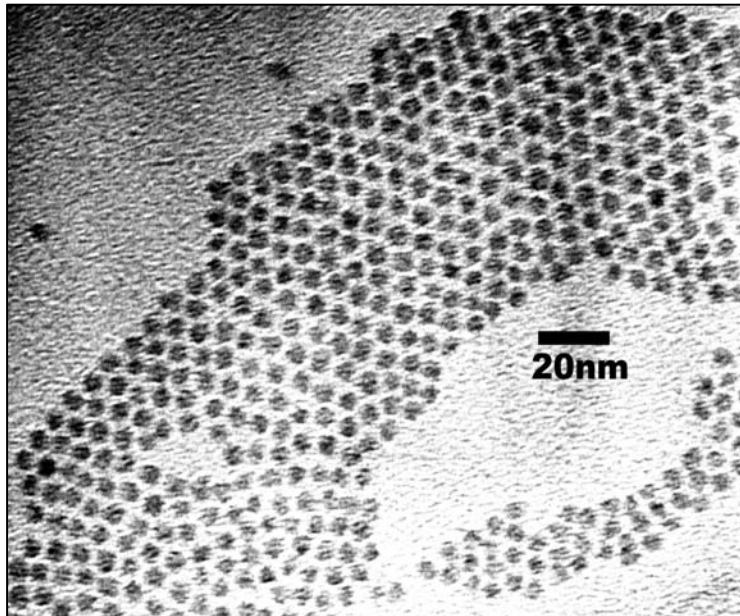


Figure 1.2. Effects of quantum confinement. Band structure (above) and its effects on absorbance of different sizes of CdSe-HDA nanomaterials (below).

properties can be linked to developments in preparative routes that allow the routine preparation of high quality nanocrystals.³

In order to undertake accurate studies of nanocrystals, high quality materials are necessary. The materials must be crystalline with a small number of lattice imperfections or stacking faults, monodisperse in size and shape ($< 5\%$ size dispersity)^{1m}, and well passivated (Figure 1.3). These requirements ensure that the nanocrystal sample exhibits a set of well defined electronic states (Figure 1.4). As the intended applications of these materials shift from fundamental studies to device applications, the synthetic focus has shifted to the development of a reliable and reproducible method for large-scale synthesis (greater than one gram from each reaction).

Any method for the preparation of nanomaterials must consist of the nucleation and growth steps. The nucleation step involves the formation of a small nanocrystal nucleus, and the growth step involves the addition of precursor material or active species to this nucleus in order to achieve the correct size. Because the formation of bulk materials is thermodynamically favored, an important aspect of nanomaterial synthesis involves controlling the rate of growth by either limiting the concentration of precursor or hindering its ability to access and bind the nanocrystal surface. Also, because the growth rate of a nanomaterial is highly dependent on its surface energy and, therefore, size it is crucial to achieve as complete separation as possible between the nucleation and growth stages to obtain a small size distribution in the final product. Finally, in order for the optical and electronic properties of



5nm

Figure 1.3. Examples of high quality nanomaterials. The sample exhibits a small size distribution and high crystallinity of individual nanocrystals.

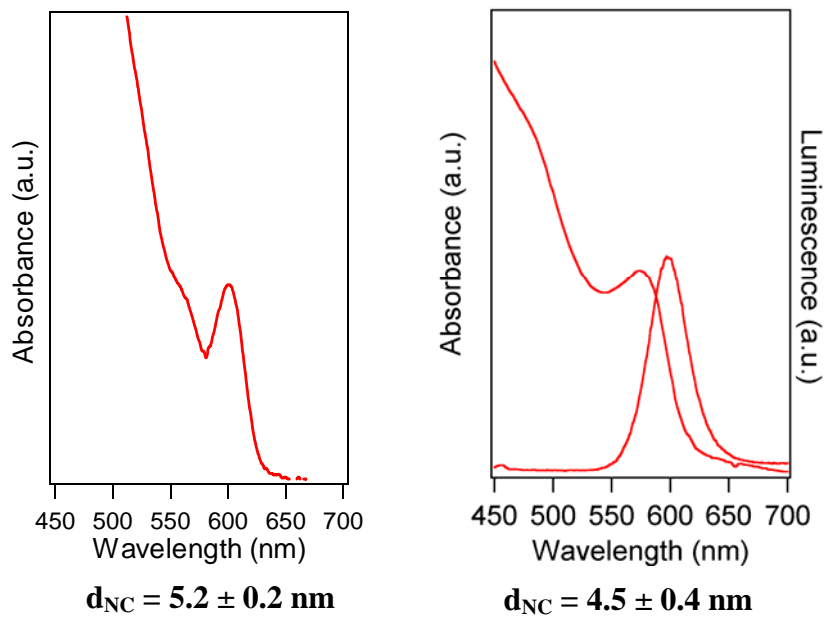


Figure 1.4. Effects of size distribution on the optical properties of a nanocrystal sample.

nanomaterials to be fully utilized it was important to develop a synthesis that allowed the nanomaterials to be isolated and processed following the synthesis.

1.2.2 Arrested precipitation methods.

The first reported synthetic route for nanocrystal (NC) preparation was the arrested precipitation method. In this method, the nucleation was effected by controlled precipitation of dilute precursor solutions with rapid termination of growth producing nano-sized crystallites.⁴⁻⁸ The metathesis reaction was initiated by mixing of the metal and chalcogenide precursors in a polar solvent (water, methanol, acetonitrile). NCs formed because the K_{sp} of the semiconductor materials in these solvents was very low. Initial NC size was determined by mixing kinetics, precursors, precursor concentrations, and temperature. The growth (aging) of these seeds was achieved by varying the solution temperature. The growth process was described as a thermodynamic competition between growth of larger particles and the dissolution of smaller (less stable) particles, known as Ostwald ripening. The average final size of the nanomaterials depended on initial size, growth time, growth temperature, precursor solubility, solvent dielectric constant, and pH. The colloid suspension was prevented from agglomerating by exploiting the Coulombic repulsion between the individual crystallites, with excess metal or chalcogenide ions added to enhance this effect. A more efficient way to prevent NC agglomeration was to add polymer or polyelectrolyte species to the reaction mixture. These species bound to the NC surfaces and prevented contact between the particles.

Stabilizer passivated NCs could be precipitated out of the growth solvent and dispersed in other solvents.

Attempts to control dispersity by growth in defined cavities resulted in the extension of arrested precipitation studies to growth of nanoscale materials in zeolites,⁹⁻¹⁰ molecular sieves,¹¹ polymers,¹² micelles,¹³ and reverse micelles¹⁴⁻¹⁶ with the latter method being particularly well developed. In this method a large number of micelle coated polar solvent droplets (typically water) were formed in a solution of a nonpolar nonsolvent (typically heptane); the solution was stirred continuously to prevent the solvent drops from coalescing. A small amount of surfactant (typically the disodium salt of bis(ethylhexyl)sulfosuccinate, or AOT) was added to form an inverse micelle layer around each water droplet with the polar head groups on the inside of the micelle. The size of the solvent droplets was controlled by varying the ratio of [water]/[AOT]. The metal and chalcogenide precursors were then introduced and allowed to react in the solvent droplets. Nucleation was achieved by introducing a chalcogenide anion solution into an existing inverse micellar suspension charged with the metal cation. Growth took place by addition of more precursor materials with the droplet controlling the size of the nanomaterial, with the inverse micelle layer preventing particle aggregation. Surface functionalization of the nanomaterials was achieved by adding an organic capping ligand such as thiophenol to the reaction after desired core size was obtained. These colloidal methods allowed both semiconductor and metal nanomaterials to be produced from readily available precursors, and allowed the

crystallites to be isolated for further investigation by evaporating the solvent. Material quality, however, left room for improvement as most of the confined cavity preparations yielded nanoparticles with large size dispersities on the order of 10-20%, and because the synthesis was carried out at low temperatures, the products exhibited poor crystallinity. Some improvement in the crystallinity of the products was obtained by annealing the crystallites in high boiling non coordinating solvents following synthesis and isolation.^{14a} Another significant drawback of this synthetic method was the low yield of product. Because of the low solubility of the semiconductor materials and the large volume of nonsolvent needed to maintain an inverse micellar suspension, typically a few 10s of mg could be isolated from several liters of reaction.

1.2.3 Lyothermal methods.

Problems with NC size dispersity and crystallinity were largely surmounted by the development of lyothermal synthetic techniques, with the nanomaterials grown by thermal degradation of organometallic precursors in coordinating solvents at temperatures in the 280 – 350°C range.³⁻¹⁷ The high temperatures proved to be critical in separating the nucleation and growth stages of synthesis resulting in improved dispersity of the final product, and allowing lattice defects to anneal out so that high crystallinity was obtained. Analysis of the reaction mechanism indicates selection of the passivating solvent, reaction precursors, reaction

conditions are all critical to control of the material dispersities and material topologies.¹⁸⁻²⁰

The first lyothermal synthetic method was reported by Murray and co-workers.³ Nucleation was carried out by a fast injection of a tri-n-octyl phosphine (TOP) solution containing Me_2Cd and TOPSe precursors into 300°C tri-n-octyl phosphine oxide (TOPO). The fast injection resulted in a homogeneous nucleation producing a suspension of small, uniform nuclei. Also, the injection of room temperature precursors into the hot coordinating solvent caused the reaction temperature to decrease below the point where the nanocrystals could grow allowing the nucleation and growth stages to be effectively separated. Nanomaterial growth took place when the reaction temperature was slowly raised to 280-300°C with the growth mechanism believed to be Ostwald ripening. The nanomaterials could be isolated from the growth solution by precipitation and redispersed in nonpolar solvents such as hexanes or toluene. Solubility of the prepared nanomaterials could be altered by ligand exchange. Even though this early version of lyothermal growth shared its growth mechanism with the arrested precipitation method, the stronger binding organic ligands and tighter size distribution of the nuclei, resulted in a smaller size distribution in the final product. Size distribution could be further improved by taking advantage of the slight decrease in solubility of the larger nanocrystals to size selectively precipitate specific fractions of the product by slow addition of a nonsolvent. This size selective precipitation allowed the researchers to achieve near monodisperse nanomaterial materials.

The Murray method was modified by Alivisatos and co-workers one year later to allow the production of near monodisperse nanomaterials directly out of batch, without the need for post synthetic size selection.¹⁷ To achieve this result, the injection of precursors was performed at 350°C, with higher nucleation temperature resulting in lower nucleus dispersity. This lower dispersity was maintained through the growth phase of the synthesis by subsequent addition of small amounts of precursor materials at 300°C. The maintenance of high precursor concentration throughout the synthesis prevented the growth of larger nanomaterials at the expense of the small ones as a result of Ostwald ripening and the resultant increase in size distribution thus allowing near monodisperse materials to be produced out of batch.¹⁸ Further modifications of the lyothermal synthesis allowed the use of the Ostwald ripening and sequential injection growth mechanisms in conjunction with different coordinating solvent mixtures to prepare a large variety of nanocrystal sizes and shapes.^{19, 20} The drawback of these modified methods was that the reduction of reaction volume necessary to achieve controlled nucleation and growth precursor injection also resulted in reduced materials yield from each synthesis.

A significant drawback of all the lyothermal methods was the necessity of using unstable, air sensitive, and highly reactive precursors which were difficult to store and handle. The extreme reactivity of the precursors also made each reaction a gamble with variables such as fractions of a second differences in injection speed and minor contaminants in the coordinating solvent drastically affecting the

outcomes of reactions. Finally, the high cost of the precursors resulted in expensive nanomaterials even though the yields were much improved over those typical of the arrested precipitation methods. Lyothermal routes are highly dependent on the nature of the materials being prepared, with CdSe exhibiting the greatest control and InP far less control over growth.²¹ In the case of the Cd chalcogenide II-VI materials, CdSe is more easily controlled lyothermally, in comparison to CdS and CdTe. Much of the differences in reaction behavior arise from the nature of the metals or binary semiconductor constituents due to differences in the chemical reactivity. In particular differences in reactivity, material quality, particle size, and particle dispersities can be roughly correlated to the differences in Bohr radius, oxidative stability, the strength of electron-electron interactions, electron-phonon interactions, and the ionicity of the respective metal-chalcogenide lattices.²² Some improvement in the reproducibility of lyothermal methods has been achieved by modifying the solvent mixture to include amine ligands which to slow down the growth and allow for near monodisperse nanomaterials to be grown more consistently.²³ Also, the use of air-stable, non-organometallic precursors based on CdO and Cd(OAc)₂ in the traditional phosphine solvent have been shown to produce high quality CdSe materials by a similar pyrolytic nucleation event.^{24,25} Both of these methods, however, are still sensitive to the exact temperature of nucleation and limited in the quantities of materials that can be produced from one reaction.

1.2.4. Molecular cluster precursor method.

A new direction for nanomaterial preparation being pursued is the use of single source precursors that are stable under ambient conditions, and have the metal-chalcogenide bond already templated in the molecular precursor. The use of pyrolyzable single source precursors with pre-formed metal-chalcogenide bonds provides a convenient reactive intermediate for growth under lyothermal conditions, allowing the preparation of nanomaterials from relatively innocuous reagents at somewhat lower temperatures than required for the lyothermal syntheses described in the previous section. These molecular single source precursors have been successfully used to prepare a wide variety of nanomaterials.³⁶⁻²⁸ Additional advantages of a single source precursor synthetic method are the potential for preparation of materials that would not be stable at high temperatures, or cannot form by metathesis of multiple precursor molecules. Single source precursor syntheses also offer the possibility of an additional level of synthetic control over the product material by precursor modification. Despite their proven and potential advantages, however, these syntheses still rely on the high temperature precursor addition to achieve nucleation. To circumvent this step, a precursor with a pre-formed nucleus is needed.

Inorganic clusters are a class of materials that may potentially be ideal for application as single source precursors. The clusters exist as discrete units with structures related to a fragment of a bulk lattice.²⁹⁻⁴¹ Previous NMR and mass

spectroscopy studies on exchange dynamics in metal chalcogenide clusters comprised of $[M_{10}Se_4(SPh)_{16}]^{4-}$ (where M = Cd, Zn and SPh is thiophenolate) suggest rapid ligand and metal exchange at room temperature occurs in solution, coupled with a propensity to rearrange to form larger molecular clusters with the loss of $Cd(SPh)_3^-$. The rearrangement to form more thermodynamically stable species proceeds through a non-stoichiometric reaction mechanism with the formation of phenyl disulfide and $Cd(SPh)_3^-$ species.^{37b, 37c} Due to the inherent thermodynamic instability of the clusters, several researchers have used the $[M_{10}Se_4(SPh)_{16}]^{4-}$ clusters as an inorganic precursors for growth of bulk semiconductors via direct thermal decomposition of the solid powders, as well as solvothermal decomposition in pyridine.^{37d}

The propensity for formation of thermodynamically stable clusters of larger nuclearity in solvents and bulk structures in solid state reactions suggest these inorganic molecular clusters, although non-stoichiometric with respect to the ratio of Cd and Se in the final nanomaterials, may allow controlled growth of II-VI nanomaterials if the kinetic and thermodynamic reactions are controlled by the choice of the reaction conditions.^{37, 39, 42} In this process, the cluster would act as a preformed nucleus capable of structural rearrangement without dissolution, thus allowing separation of the nucleation from the growth step using a single source precursor without a requisite pyrolytic event to initiate nucleation.

The successful utilization of these precursors to the growth of CdSe, ZnSe, CdS, and ZnS nanomaterials is presented in Chapters 2 and 3 of this thesis.⁴³ For

each material, a range of crystallite sizes exhibiting low size distributions could be prepared. The materials exhibited good crystallinity. As previously observed for other synthetic methods, the largest range of sizes was obtained for CdSe dots so most of the work was carried out with these materials. The CdSe materials could be isolated, annealed, subjected to size selective precipitation and capped with a layer of inorganic passivant to improve their PL properties.

1.3 Size and size dispersity analysis by MALDI-MS.

As stated above, the size dependent nature of nanoscale materials requires that the size, shape, and dispersity are accurately known for optical and electronic property investigation as well as applications in device technology.¹ Traditionally, optical spectroscopy coupled to either TEM or powder XRD (pXRD) analysis has been employed as a measure of shape, size, and size distributions for semiconductor nanocrystal samples. Calculation of size from pXRD data by fitting to the Scherer equation has inherent inaccuracies, as the pXRD peak width is also affected by the shape and size distribution of the nanocrystals.⁴⁴ Measuring the shape, size, and size distribution from transmission electron microscope (TEM) images involves another set of uncertainties, as the measurement of size and size distribution is very subjective and the resolution is dependent on the contrast, which can be low for nanomaterials of lighter elements. Attempts to utilize high performance liquid chromatography (HPLC) have shown promise for determination of size and size distribution for several metal and semiconductor nanomaterials, but the technique

suffers from the strong dependence of the sample retention time on the interaction of the capping ligands with the separation column.⁴⁴ An alternative analytical technique, which is often used for compositional analysis is mass spectrometry. Mass spectrometric methods can provide a very accurate method for measuring mass and, therefore, sizes and size distributions of nanomaterial samples.

Mass spectrometric methods has been demonstrated to provide valuable insight into the structure of a wide range of materials at the nanoscale,⁴⁵⁻⁵² biological^{45,46}, polymer⁴⁷, and nanoscale materials.⁵¹⁻⁵² Thiol passivated Au nanocrystals, prepared in solution, were analyzed in the 1.5 – 3.5 nm size range (10 –1000 Au atoms) by laser desorption ionization (LDI) mass spectrometry resulting in a very accurate analysis of the size, shape, and passivation of these nanomaterials.⁵² In addition, Martin, et al, observed MS data for <2.0 nm ZnS clusters generated in the gas phase demonstrating that MS techniques are applicable to II-VI materials.⁵¹ These studies suggest that MS methods can be used to investigate the mass, size and size dispersity of nanomaterials.

The application of the mass spectrometric method to nanomaterials is less straightforward than the analysis of the systems described above because of the added complications of size distribution and surface ligands, however, promising results could be obtained. Chapter 4 will discuss the characterization of CdSe and ZnS nanomaterials by MALDI-MS. The method yielded average size and size distribution measurements that compared well to those obtained by optical and TEM methods. In addition to the sample characterization, insights into the effect of core

material, the nature of the capping ligands, the nature of the matrix used, the analyte:matrix ratio, and effects of ionizing radiation intensity were obtained. Overall, MALDI-MS seems to have a lot of potential as a rapid screening tool for inorganic nanomaterials.

1.4 Inorganic molecular cluster degradation by ESI-MS.

In order to fully develop the potential of the single source precursor synthetic method, the mechanism by which the molecular cluster is converted to the nanocrystal needs to be better understood. In particular the active species in solution need to be identified and their chemistry studied. Once this information is available, the synthetic variables like temperature, precursor concentration, coordinating solvent, and reaction time can be optimized for each material to obtain the best possible results.

The use of the electrospray ionization (ESI) method for inorganic-organic hybrid materials has allowed for the mass spectral analysis of ions from the liquid phase with minimal fragmentation.⁵³ Coupling ESI with the use of tandem MS (MS/MS) is of even greater usefulness for the characterization of complicated chemical systems. The technique allows for the isolation of a single ion from an analyte mixture and the systematic degradation of this ion to establish its composition. In this way relationships between chemical species detected by MS may be established.

Because the reaction mixture is an overly complicated system, it is best to begin with the analysis of known intermediates in the formation of inorganic nanomaterials. We have previously published an ESMS study of $[\text{Cd}_{32}\text{S}_{14}(\text{SPh})_{36}\text{DMF}_4]$ which is a known intermediate in the solid state conversion of $[\text{Cd}_{10}\text{S}_4(\text{SPh})_{16}]^{4-}$ to bulk CdS (Figure 1.5).^{37d} In addition to identifying a large number of potential active species in the reaction mixture, the data for cluster degradation suggest that the intermediate cluster fragments along a pseudo lattice plane in the high energy environment of the ESMS source (Figure 1.6).⁵⁴

Chapter 5 of this thesis will report the ESMS and MS/MS characterization of the $[\text{Ti}_6\text{O}_4(\text{EtO})_8(\text{McO})_8]$ cluster where EtO and McO denote ethoxide and methacrylate ligands, respectively (Figure 1.7).⁵⁵ Discrete $[\text{Ti}_x\text{O}_y\text{L}_z]$ clusters are stable materials, consisting of a titanium oxide core surrounded by alkoxy or carboxylic acid ligands, that are important intermediates in the conversion of $\text{Ti}(\text{OR})_4$ precursors to TiO_2 glasses and sol-gel materials by either acid or base catalyzed hydrolysis.^{56,57} These clusters are obtained by in-situ hydrolysis of $\text{Ti}(\text{OR})_4$ in the presence of an n-alkyl carboxylic acid. The bulky carboxylate ligands stabilize small titanium oxide clusters and prevent the formation of bulk TiO_2 . Fragmentation analysis in the MS/MS indicates formation of a family of species related to titanium oxide architectures commonly observed in bulk lattices. This suggests a surprising level of insight into structure stability can be gained by inspection of the fragmentation pattern in inorganic clusters. These clusters are potentially useful as building blocks in hybrid materials as it is possible to

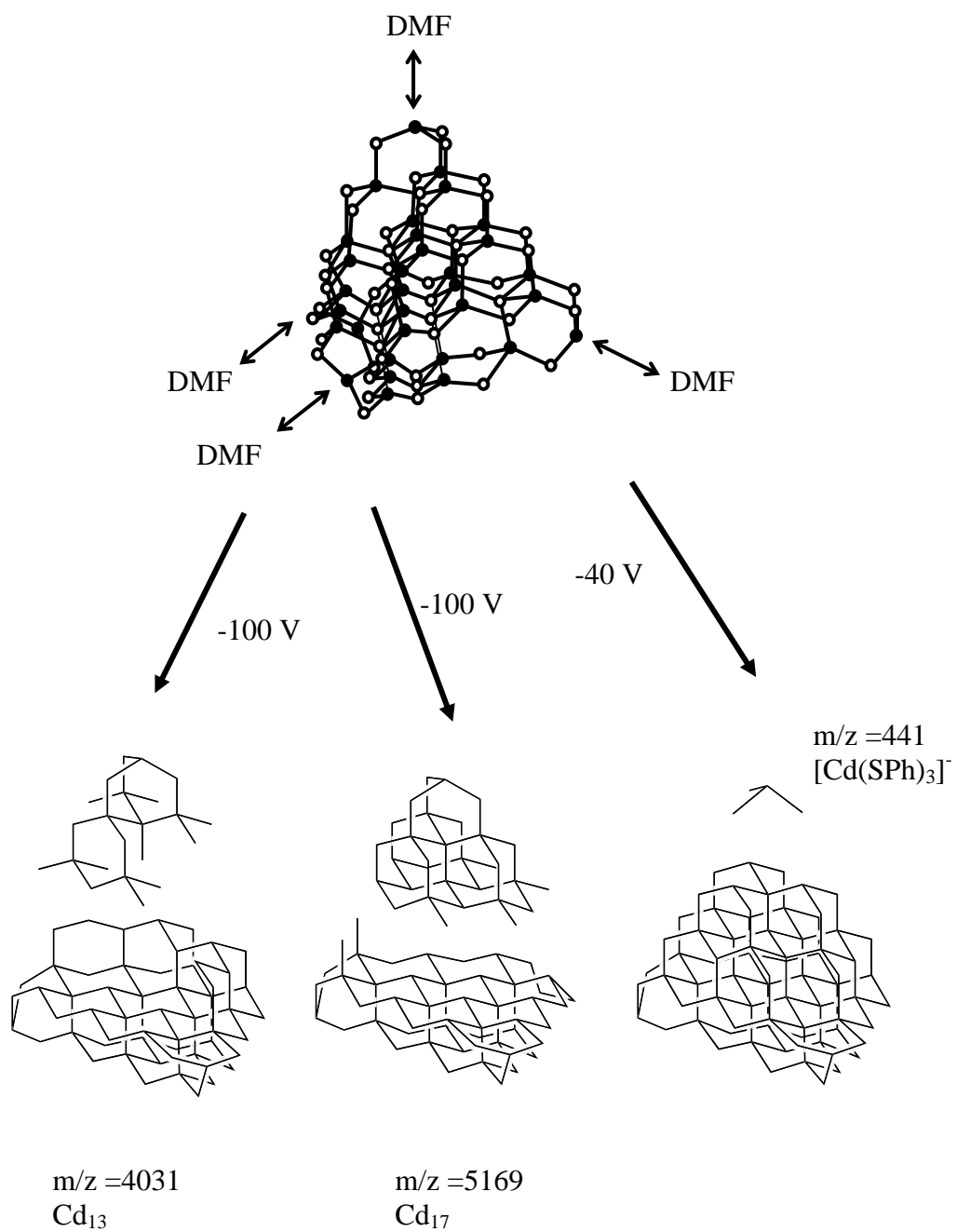


Figure 1.5. Major ESMS fragmentation products of $[Cd_{32}S_{14}(SPh)_{36}DMF_4]$.

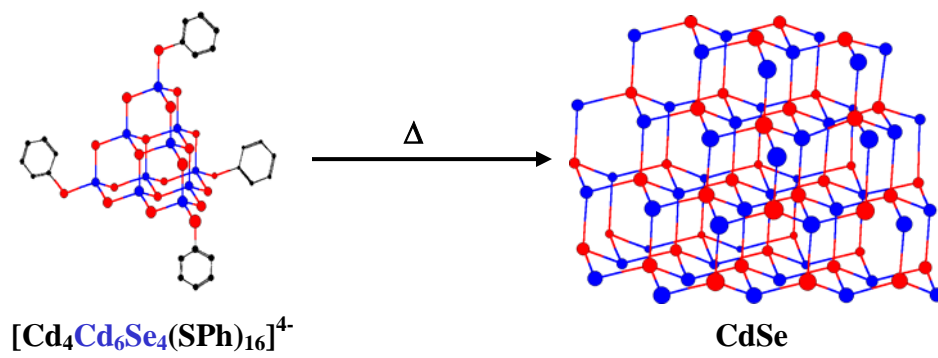


Figure 1.6. Conversion of molecular clusters to bulk lattice semiconductors.

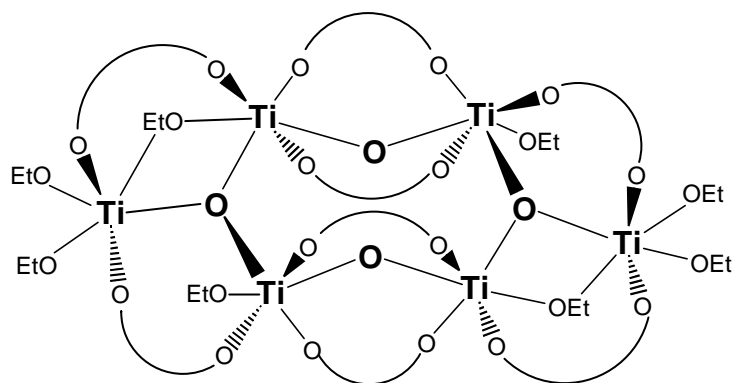


Figure 1.7. Structure of $\text{Ti}_6\text{O}_4(\text{EtO})_8(\text{McO})_8$. The methacrylate ligands are represented by curves for clarity.

incorporate the organic capping groups into a polymer network while maintaining the integrity of the core.^{56,57} While XRD, NMR, and spectroscopic studies exist, there are no published reports of a MS characterization of a discrete cluster with a Ti_xO_y core.

The data for both species identifies a large number of potential active species. The observed fragmentation pattern for the cluster in coordinating solvent compares very well to the chemistry observed for similar clusters in solution. The fragmentation pattern in non-coordinating solvent suggests that the fragmentation in the source and collision cell of the mass spectrometer take place by the same chemical processes that occur in solution. This last observation makes ESMS a very useful tool in the study of solution mediated nanomaterial formation.

1.5. References.

- 1) (a) Eychmuller, A. *J. Phys. Chem.* **2000**, *104*, 6514. (b) Brus, L. *J. Phys. Chem.* **1986**, *90*, 2555. (c) Brus, L. E. *Appl. Phys. A.* **1991**, *53*, 465. (d) Nirmal, M.; Brus, L. *Acc. Chem. Res.* **1999**, *32*, 407. (e) L. E. Brus, L. E.; Trautman, J. K. *Philosoph. Trans. R. Soc. London. Sect. A* **1995**, *353*, 313. (f) Wang, Y.; Herron, N. *J. Phys. Chem.* **1991**, *95*, 525. (g) Banyai, L.; Koch, S. W. *Semiconductor Quantum Dots*; World Scientific: Singapore, **1993**. (h) Weller, H. *Angew. Chem., Int. Ed. Engl.* **1993**, *32*, 41. (i) Weller, H. *Adv. Mater.* **1993**, *5*, 88. (j) Alivisatos, A. P. *J. Phys. Chem.* **1996**, *100*, 13226. (k) Waggon, U. *Optical Properties of Semiconductor Quantum*

- Dots*. Springer-Verlag: Berlin, **1997**. (l) Gaponenko, S. V. *Optical Properties of Semiconductor Nanocrystals*. Cambridge University Press: Cambridge **1998**. (m) Green, M.; O'Brien, P. *Chem. Commun.* **1999**, 2235. (n) Henglein, A. *Top. Curr. Chem.* **1988**, *143*, 113. (o) Henglein, A. *Chem. Rev.* **1989**, *89*, 1861.
- 2) (a) Klein, D. L.; Roth, R.; Lim, A. K. L.; Alivisatos, A. P.; McEuen, P. L. *Nature* **1997**, *389*, 699. (b) Feldheim, D. L.; Keating, C. D. *Chem. Soc. Rev.* **1998**, *28*, 1. (c) Colvin, V. L.; Schlamp, M. C.; Alivisatos, A. P. *Nature*, **1994**, *370*, 354. (d) Dabbousi, B. O.; Bawendi, M. G.; Onitsuka, O.; Rubner, M. F. *Appl. Phys. Lett.* **1995**, *66*, 1316. (e) Cordero, S. R.; Carson, P. J.; Estabrook, R. A.; Strouse, G. F.; Buratto, S. K. *J. Phys. Chem. B* **2000**, *104*, 12137-42.
- 3) Murray, C. B.; Norris, D. J.; Bawendi, M. G. *J. Am. Chem. Soc.* **1993**, *115*, 8706.
- 4) (a) La Mer, V. K.; Dinegar, R. H. *J. Am. Chem. Soc.* **1950**, *72*, 4847. (b) Johnson, T.; La Mer, V. K. *J. Am. Chem. Soc.* **1947**, *69*, 1184.
- 5) Hunter, R. J. *Foundations of Colloid Science*, Oxford University Press, 6th edn., Oxford, 1993, vol. 1, pp. 13-17.
- 6) (a) Rossetti, R.; Nakahnara, S.; Brus, L. E. *J. Chem. Phys.* **1983**, *79*, 1986. (b) Rossetti, R.; Ellison, J. L.; Gibson, J. M.; Brus, L. *J. Chem. Phys.* **1984**, *80*, 4464.
- 7) Henglein, A. *Pure Appl. Chem.* **1984**, *56*, 1215.

- 8) Rossetti, R.; Hull, R.; Gibson, J. M.; Brus, L. E. *J. Chem. Phys.* **1985**, *82*, 552.
- 9) (a) Wang, Y.; Herron, N. *J. Phys. Chem.* **1987**, *91*, 257. (b) McDougall, J. E.; Eckert, H.; Stucky, G. D.; Herron, N.; Wang, K.; Moller, T.; Bein, T.; Cox, D. *J. Am. Chem. Soc.* **1989**, *111*, 8006.
- 10) Brigham, E. S.; Weisbecker C. S.; Rudzinski, W. E.; Mallouk, T. E. *Chem. Mater.* **1996**, *8*, 2121.
- 11) Abe, T.; Tachibana, Y.; Uematsu, T.; Iwamoto, M. *J. Chem. Soc., Chem. Commun.* **1995**, 1617.
- 12) (a) Wang, Y.; Suna, A.; Mahler, W.; Kasowski, R. *J. Chem. Phys.* **1987**, *87*, 7315. (b) Fotjik, A.; Weller, H.; Koch, U.; Henglein, A. *Ber. Bunsenges. Phys. Chem.* **1984**, *88*, 969. (c) Haggata, S. W.; Cole-Hamilton, D. J.; Fryer, J. R. *J. Mater. Chem.* **1996**, *7*, 1969.
- 13) Watzke, H. J.; Fendler, J. H. *J. Phys. Chem.* **1987**, *91*, 854.
- 14) (a) Kortan, A. R.; Hull, R.; Opila, R. L.; Bawendi, M. G.; Stiegerwald, M. L.; Carroll, P. J.; Brus, L. E. *J. Am. Chem. Soc.* **1990**, *112*, 1327. (b) Steigerwald, M. L.; Alivisatos, A. P.; Gibson J. M.; Harris, T. D.; Kortan, R.; Muller, A. J.; Thayer, A. M.; Duncan, T. M.; Douglass, D. C.; Brus, L. E. *J. Am. Chem. Soc.* **1988**, *110*, 3046.
- 15) Meyer, M.; Walberg, C.; Kurihara, K.; Fendler, J. H. *J. Chem. Soc., Chem. Commun.* **1984**, 90.

- 16) Lianos, P.; Thomas, J. K. *Chem. Phys. Lett.* **1986**, *125*, 299. Inger, D;
Pileni, M. P. *Adv. Func. Mater.* **2001**, *11*, 136 and references herein.
- 17) Katari, J. E. B.; Colvin, V. L.; Alivisatos, A. P. *J. Phys. Chem.* **1994**, *98*,
4109.
- 18) Peng, X.; Wickham, J.; Alivisatos, A. P. *J. Am. Chem. Soc.* **1998**, *120*, 5343.
- 19) Manna, L.; Scher, E. C.; Alivisatos, A. P. *J. Am. Chem. Soc.* **2000**, *122*,
12700.
- 20) (a) Peng, X.; Manna, L.; Yang, W.; Wickham, J.; Scher, E.; Kadavanich, A.;
Alivisatos, A. P. *Nature*, **2000**, *404*, 59. (b) Peng, Z. A.; Peng, X. *J. Am.*
Chem. Soc. **2002**, *124*, 3343-53.
- 21) Guzelian, A. A.; Katari, J. E. B.; Kadavanich, A. V.; Banin, U.; Hamad, K.;
Juban, E.; Alivisatos, A. P.; Wolters, R. H.; Arnold, C. C.; Heath, J. R. *J.*
Phys. Chem. **1996**, *100*, 7212-9.
- 22) Abrikosov, N. Kh.; Bankina, V. F.; Poretskaya, L. V.; Shemilova, L. E.;
Skudnova, E. V.; translated by Tybulewicz, A. *Semiconducting II-VI, IV-VI,*
and V-VI Compounds, Plenum: New York, 1969.
- 23) Talapin, D. V.; Rogach, A. L.; Kornowski, A.; Haase, M.; Weller, H. *Nano*
Letts. **2001**, *1*, 207-11.
- 24) (a) Peng, Z. A.; Peng, X.; *J. Am. Chem. Soc.* **2001**, *123*, 183. (b) Peng, Z.
A.; Peng, X.; *J. Am. Chem. Soc.* **2001**, *123*, 1389. (c) Qu, L.; Peng, Z. A.;
Peng, X.; *Nano Letts.* **2001**, *1*, 333.
- 25) Yang, C.; Awschalom, D. D.; Stucky, G. D. *Chem. Mater.* **2001**, *13*, 594.

- 26) (a) Trindade, T.; O'Brien, P. *Adv. Mater.* **1996**, *8*, 161. (b) Trindade, T.; O'Brien, P.; Zhang, X. *Chem. Mater.* **1997**, *9*, 523. (c) Ludolph, B.; Malik, M. A.; O'Brien, P.; Revaprasadu, N. *Chem. Commun.* **1998**, 1849. (d) Malik M. A.; Revaprasadu, N.; O'Brien, P. *Chem. Mater.* **2001**, *13*, 913.
- 27) (a) Brennan, J. G.; Siegrist, T.; Carroll, P. J.; Stuczynski, S. M.; Brus, L. E.; Stiegerwald, M. L. *J. Am. Chem. Soc.* **1989**, *111*, 4141-43. (b) Brennan, J. G.; Siegrist, T.; Carroll, P. J.; Stuczynski, S. M.; Reynders, P.; Brus, L. E.; Stiegerwald, M. L. *Chem. Mater.* **1990**, *2*, 403-409. (c) Stiegerwald, M. L.; Stuczynski, S. M.; Kwon, Y. U.; Vennos, D. A.; Brennan J. G. *Inorg. Chim. Act.* **1993**, *212*, 219-224.
- 28) Jun, Y. W.; Lee, S. M.; Kang, N. J.; Cheon, J. *J. Am. Chem. Soc.* **2001**, *123*, 5150-51.
- 29) Dance, I.; Fisher, K. *Prog. Inorg. Chem.* **1994**, *41*, 637 and references herein.
- 30) Dance, I. G.; Choy, A.; Scudder, M. L. *J. Am. Chem. Soc.* **1984**, *106*, 6285.
- 31) (a) Zhu, N.; Fenske, D. *J. Chem. Soc. Dalton Trans.* **1999**, 1067. (b) Zhu, N.; Fenske, D. *J. Clust. Sci.* **2000**, *11*, 135. (c) Muller, A.; Fenske, D.; Kogerler, P. *Curr. Opin. Solid State Mater. Sci.* **1999**, *4*, 141.
- 32) (a) Schmid, G.; Chi, L. F. *Adv. Mater.* **1998**, *10*, 515. (b) Schmid, G. J. *Chem. Soc. Dalton Trans.* **1998**, 1077.
- 33) Brown, K. R.; Natan, M. J. *Langmuir* **1998**, *14*, 726.
- 34) Gaumet, J. J.; Strouse, G. F. *J. Am. Soc. Mass. Spectrom.* **2000**, *11*, 338.

- 35) Metallothionein: Synthesis, Structure, and Properties of Metallothioneins, Phytochelatins, and Metal-Thiolate Complexes; (Eds.: M. J. M. Stillman, C. F. Shaw III, K. T. Suzuki) VCH Publishers, New York, **1992**.
- 36) Hagen, K. S.; Holm, R. H. *Inorg. Chem.* **1983**, *22*, 3171. Christou, G.; Hagen, K. S.; Bashkin, J. K. Holm, R. H. *Inorg. Chem.* 1985, *24*, 1010. Watson, A. D.; Rao, C. P.; Dorfman, J. R.; Holm, R. H. *Inorg. Chem.* **1985**, *24*, 2820.
- 37) (a) Wang, Y.; Herron, N. *J. Phys. Chem.* **1991**, *95*, 525. (b) Herron, N.; Suna, A.; Wang, Y. *J. Chem. Soc. Dalton Trans.* **1992**, 2329. (c) Wang, Y.; Harmer, M.; Herron, N. *Israel J. Chem.* **1993**, *33*, 31-39. (d) Herron, N.; Calabrese, J. C.; Farneth, W. E.; Wang, Y. *Science* **1993**, *259*, 1426.
- 38) Hagen, K. S.; Stephan, D. W.; Holm, R. H. *Inorg. Chem.* **1982**, *21*, 3928-36.
- 39) Hernandez-Molina, R.; Sykes, A. G. *J. Chem. Soc. Dalton Trans.* **1999**, 3137.
- 40) Stiefel, E. I.; Halbert, T. R.; Coyle, C. L.; Wei, L.; Pan, W. H.; Ho, T. C.; Chianelli, R. R.; Daage, M.; *Polyhedron* **1989**, *8*, 1625.
- 41) Diemann, E.; Muller, A.; Aymonino, P. J. *Z. Anorg. Allg. Chem.* **1981**, *479*, 191.
- 42) Løver, T.; Bowmaker, G.; Seakins, J. M.; Cooney, R. P.; Henderson, W. J. *Mater. Chem.* **1997**, *7*, 647.
- 43) Cumberland, S. L.; Hanif, K. M.; Javier, J.; Khitrov, G. A.; Strouse, G. F.; Woessner, S. M.; Yun, C. S. *Chem. Mater.* **2002**, *14*, 1576-1584.

- 44) (a) Wilcoxon, J. P.; Martin, J. E.; and Provencio, P. *Langmuir* **2000**, *16*, 9912-9920. (b) Wilcoxon, J. P.; Martin, J. E.; and Provencio, P. *J. Chem. Phys.* **2001**, *115*, 998-1008. (c) Wilcoxon, J. P.; and Craft, S. A. *Nanostructured Materials* **1997**, *9*, 85-88.
- 45) (a) Lay, J. O. *Mass Spec. Rev.* **2001**, *20*, 172-194. (b) Fuerstenau, S. D.; Benner, W. H.; Thomas, J. J.; Brugidou, C.; Bothner, B. Siuzdak, G.; *Angew. Chem. Int. Ed.* **2001**, *40*, 542-544. (c) Maleknia, S. D.; Downard, K. *Mass Spec. Rev.* **2001**, *20*, 388-401. (d) Veenstra, T. D. *Biophys. Chem.* **1999**, *79*, 63-79.
- 46) (a) Beck, J.L.; Colgrave, M. L.; Ralph, S. R.; Sheil, M. M. *Mass Spec. Rev.* **2001**, *20*, 61. (b) Koomen, J. M.; Russel, W. K.; Tichy, S. E.; Russel, D. H. *J. Mass Spec.* **2002**, *37*, 357-371.
- 47) (a) Belu, A. M.; DeSimone, J. M.; Linton, R. W.; Lange, G. W.; Friedman, R. M. *J. Am. Soc. Mass. Spec.* **1996**, *7*, 11-24. (b) Scrivens, J. H.; Jackson, A. T. *Int. J. Mass Spec.* **2000**, *200*, 261-276. (c) Nielen, M. W. F. *Mass Spec. Rev.* **1999**, *18*, 309-344. (d) Schwartz, B. L.; Rockwood, A. L.; Smith, R. D.; Tomalia, D. A.; Spindler, R. *Rapid Commun. Mass. Spectrom.* **1995**, *9*, 1552-55. (e) Kriesel, J. W.; Konig, S.; Freitas, M. A.; Marshall, A. G.; Leary, J. A.; Tilley, T. D. *J. Am. Chem. Soc.* **1998**, *120*, 12207-15.
- 48) Serna, R.; Dreyfus, R. W.; Solis, J.; Afonso, C. N.; Allwood, D. A.; Dyer, P. E.; Petford-Long, A. K. *Appl. Surf. Sci.* **1998**, *127-129*, 383-387.

- 49) (a) Fasce, D. P.; Williams, R. J. J.; Erra-Balsells, R.; Ishikawa, Y.; Nonami, H. *Macromolecules*, **2001**, *34*, 3534-3539. (b) Smet, P.; Devreese, B.; Verpoort, F.; Pauwels, T.; Svoboda, I.; Foro, S.; Van Beeumen, J.; Verdonck, L. *Inorg. Chem.* **1998**, *37*, 6583-6586. (c) Dyson, P. J.; Johnson, B. F. G.; McIndoe, J. S.; Langridge-Smith, P. R. R. *Inorg. Chem.* **2000**, *39*, 2430-2431. (d) Ruiz-Molina, D.; Gerbier, P.; Rumberger, E.; Amabilino, D. B.; Guzei, I. A.; Folting, K.; Huffman, J. C.; Rheingold, A.; Christou, G.; Veciana, J.; Hendrickson, D. N. *J. Mat. Chem.* **2002**, *12*, 1152-1161.
- 50) (a) Brown, T.; Clipston, N. L.; Simjee, N.; Luftmann, H.; Hungerbuhler, H.; Drewello, T. *Int. J. Mass. Spec.* **2001**, *210/211*, 249-263. (b) Rogner, I.; Birkett, P.; Campbell, E. E. B. *Int. J. Mass Spec. Ion Proc.* **1996**, *156*, 103-108.
- 51) Martin, T. P. *Phys. Rep.* **1996**, *273*, 199-241.
- 52) (a) Whetten, R. L.; Khoury, J. T.; Alvarez, M. A.; Murthy, S.; Vezmar, I.; Wang, Z. L.; Stephens, P. W.; Cleveland, C. L.; Luedtke, W. D.; Landman, U. *Adv. Mater.* **1996**, *8*, 428-433. (b) Arnold, R. J.; Reilly, J. P.; *J. Am. Chem. Soc.* **1998**, *120*, 1528-1532.
- 53) Colton, R.; D'Agostino, A.; Traeger, J. C. *Mass Spectrom. Rev.* **1995**, *14*, 79-106.
- 54) Gaumet, J. J.; Khitrov, G. A.; Strouse, G. F. *Nano Letts* **2002**, *2*, 375-379.
- 55) Schubert, U.; Arpac, E.; Glaubitt, W.; Helmerich, A.; Chau, C.; *Chem. Mater.* **1992**, *4*, 291-295.

- 56) (a) Moraru, B.; Husing, N.; Kickelbick, G.; Schubert, U.; Fratzl, P.; Peterlik, H. *Chem. Mater.* **2002**, *14*, 2732-2740. (b) Kickelbick, G.; Schubert, U.; *Monatsh. Chem.* **2001**, *132*, 13-30. (c) Schubert, U. *Chem. Mater.* **2001**, *13*, 3487-3494.
- 57) Day, V. W.; Eberspacher, T. A.; Klemperer, W. G.; Park, C. W.; *J. Am. Chem. Soc.* **1993**, *115*, 8469-8470.

Chapter 2. Inorganic Clusters as Single Source Precursors for Preparation of CdSe, ZnSe, CdSe/ZnS Nanomaterials.

2.1 Introduction

In this chapter, the results on a series of nanoscale metal chalcogenide materials prepared by a single source precursor methodology are presented, based on the introduction of a finite sized inorganic metal chalcogenide cluster into an alkylamine solvent. Owing to the rapid ligand and metal exchange for these clusters, nucleation occurs instantly at low temperatures followed by growth of nanomaterials under thermal control. This allows preparation of large scale (> 50g/L) reactions of organically passivated, spherical nanomaterials of CdSe (2-9 nm) and ZnSe (2-5 nm). The CdSe materials have size distributions <5% rms size selectively precipitated, ~5% thermally annealed or 6-12% out of batch. The CdSe can be recapped with an inorganic ZnS passivant layer following traditional lyothermal techniques via the injection of dimethyl zinc and bis (trimethylsilane) sulfide to yield CdSe/ZnS core-shell structures. A major advantage of this new methodology is the attainment of greater synthetic control. The use of a cluster based single source precursor allows nanomaterial growth to be initiated at low temperature without a requisite pyrolytic step for nucleus formation traditionally required for lyothermal growth processes. The elimination of the pyrolytic step allows greater synthetic control, slow thermodynamic growth at lower temperatures, high crystallinity, and reaction scalability.

2.2 Experimental.

2.2.1 Materials

$(X)_4[M_{10}Se_4(SPh)_{16}]$ ($X = Li^+$ or $(CH_3)_3NH^+$ and $M = Cd$ or Zn and SPh is phenyl thiolate) were prepared by literature methods¹ with the exception of using a Li^+ cation instead of a tetramethylammonium cation for isolation of $[Cd_{10}Se_4(SPh)_{16}]^{4-}$.² Hexadecylamine (HDA, 90%), and bis(trimethylsilyl sulfide) was purchased from Acros Chemical and used without further purification. Dimethyl zinc (2M solution in toluene), and trioctylphosphine (TOP, 90%) were purchased from Aldrich Chemical and used without further purification. Further purification of the precursors did not influence the reaction yields or material quality.³

2.2.2 Measurements

Ultraviolet and visible absorption spectra in chloroform or toluene were recorded using a fiber optic Ocean Optics S2000 CCD spectrophotometer. Instrument response corrected photoluminescence (PL) spectra were measured on a SPEX-fluorolog equipped with a 400W xenon lamp, and a cooled Hamamatsu R928 photomultiplier tube (PMT). PL measurements were conducted on N_2 sparged, dilute solutions with an absorption at the wavelength of excitation below 0.1 absorbance and under front face conditions to minimize self-absorption from the

quantum dot solution. PL response correction files were generated with a NIST traceable 200W quartz-halogen tungsten filament lamp (Model 220M) and steady power supply using hardware and software supplied by SPEX. Correction files are routinely generated yearly for the instrumentation.

Photoluminescence quantum yield values (ϕ_{em}) were measured relative to Rhodamine 590 in methanol for CdSe and anthracene in toluene for ZnSe systems and were calculated using equation 1.⁴

$$\phi_{em} = \phi'_{em}(I/I')(A'/A)(n/n')^2 \quad (1)$$

In equation 1, I (sample) and I' (standard) are the integrated emission peak areas, A (sample) and A' (standard) are the absorbances at the excitation wavelength, and n (sample) and n' (standard) are the refractive indices of the solvents.

Transmission electron microscopy (TEM) was performed on a JEOL 2000 microscope operating at either 100 or 200 kV in the bright field mode. The TEM magnification was calibrated by measuring the lattice fringe spacing on Au nanocrystals. TEM grids were 400 mesh Cu, coated with a 5nm layer of holey carbon, and purchased from SPI. TEM samples were prepared using standard techniques. Size and size distributions were obtained by manual measurement of nanocrystal images obtained by digitizing the micrograph negatives.

The powder X-ray diffraction patterns (pXRD) of the nanocrystals were obtained on a Scintag X2 diffractometer using Cu K α radiation, excited at 45 kV

and 35 mA. The x-rays were collimated at the source with 2 mm divergence and 4 mm scatter slits. The detector had 0.5 mm scatter and 0.2 mm receiving slits.

XPS samples were prepared by pressing a small amount of isolated nanomaterial against graphite adhesive tape. XP spectra were collected on a Kratos Axis Ultra instrument with an efficient charge balance system.

2.2.3 Preparation of amine-capped CdSe Nanoparticles.

Approximately 55g of HDA was degassed under vacuum at 120 °C. To the melted and stirred HDA, 1.0 g (0.28 mmol) of $(\text{Li})_4[\text{Cd}_{10}\text{Se}_4(\text{SPh})_{16}]$ was added using standard airless techniques under N_2 and the solution temperature raised to 220-240°C (1°C/minute). Growth rates depend on the initial reactant concentration and can be followed by absorption spectroscopy. At the desired size, the reaction was cooled by 20 °C, and left overnight to narrow the size distribution by annealing the nanocrystals. The CdSe can be isolated by selective precipitation by addition of 100 ml of anhydrous MeOH, and isolating via centrifugation. Excess HDA is removed by subsequent re-suspension in MeOH and isolation by centrifugation.

2.2.4 Preparation of amine-capped ZnSe Nanoparticles.

Approximately 55g of HDA was degassed at 120 °C for 2 hours. To the stirred solution of HDA under N_2 , 600 mg (0.20 mmol) of $(\text{TMA})_4[\text{Zn}_{10}\text{Se}_4(\text{SPh})_{16}]$ was added and the solution temperature was raised to 220-280°C (1°C/minute). Analogous to the above reaction, the nanomaterial growth can be monitored by

absorption spectroscopy and isolated by cooling the reaction to 80 °C, adding 100 ml anhydrous methanol, and centrifugation of the precipitated ZnSe nanomaterials.

2.2.5 Preparation of CdSe/ZnS core/shell Nanostructures.

The core/shell structures were prepared by a modification of the procedure developed by Hines and co-workers.⁵ At the desired nanomaterial size, a four fold excess of a TOP solution containing equimolar dimethylzinc and bis(trimethylsilyl) sulfide was injected into the reaction mixture at 250°C. The product was collected as described above. The amounts of dimethylzinc and bis(trimethylsilyl) sulfide were determined from the estimate of the core diameter based on absorption spectroscopy and the requisite concentration of precursor required to obtain the desired shell thickness.

2.2.6 Size Selective Precipitation.

Depending on the temperature ramp rate, nanomaterials can be isolated from the batch without size-selection with a dispersity of 6-8% based on correlating the results of TEM, absorption, and PXRD linewidths in comparison to reported literature.⁶ Thermal annealing of the reaction mixture for 24 h allows the nanomaterials to be isolated with 5% dispersity without size selective precipitation. For non-annealed batches 5% dispersity is achieved by narrowing the distribution by size-selective precipitation from toluene. This procedure results in center

enrichment with the isolation of ~50% of the batch with ~ 5% rms size distribution based on TEM analysis of the samples.

2.3 Results.

2.3.1 Synthesis and characterization.

Selected absorption and emission spectra of CdSe, and ZnSe nanocrystals grown from $[M_{10}Se_4(SPh)_{16}]^{4+}$ ($M = Cd$ or Zn , SPh is thiophenol) are shown in Figure 2.1 and Figure 2.2. The two growth progressions show well-defined excitonic structure and size quantization. The sizes of the CdSe nanoparticles were estimated using absorption spectroscopy,⁷ and verified by TEM analysis. Representative TEM analysis of CdSe, ZnSe, and CdSe/ZnS core-shell nanocrystals exhibiting lattice fringes are illustrated in Figure 2.3. The absorption data for size selection of a typical reaction batch of 5.6 nm CdSe (12% batch size dispersity) is shown in Figure 2.4. TEM size-distribution analysis of the size selected batch (Figure 2.4b) shows ~5% size dispersity can be achieved, as observed previously in TOP/TOPO grown materials. Table 2.1 lists the exciton absorption maxima, exciton FWHM, and TEM distribution analysis for several sizes of CdSe and ZnSe nanoparticles. The observed quantum yields for the CdSe and CdSe/ZnSe samples are comparable to the reported quantum yields for lyothermally grown materials^{6,8} Quantum yields for emission on the core/shell materials indicate an enhancement of the emission in the 3.7 nm and 4.5 nm CdSe/ZnS core/shell (QY = 20%) samples by

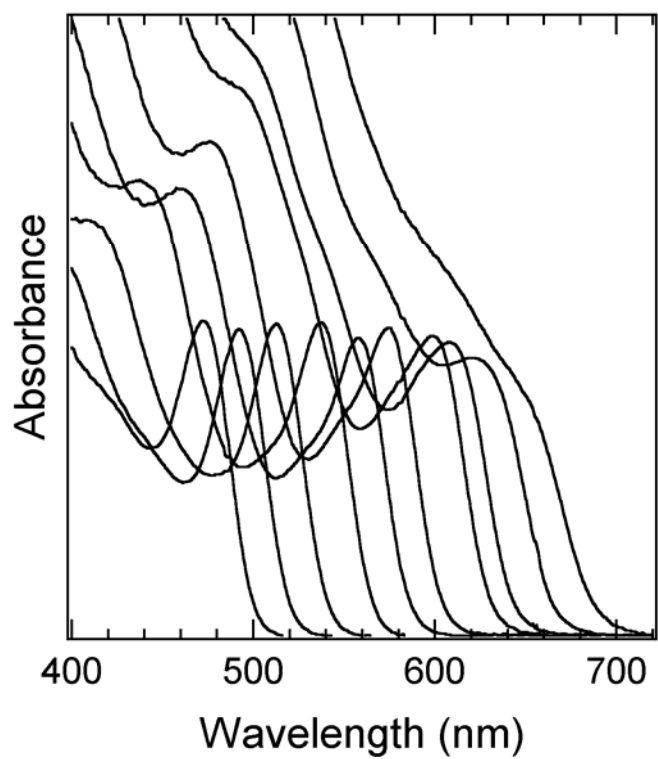


Figure 2.1a. Normalized absorbance spectra of 2.5 – 9 nm CdSe-HDA. Spectra were measured in toluene at 298 ± 2 K. Nanocrystals were prepared by the single-source precursor route.

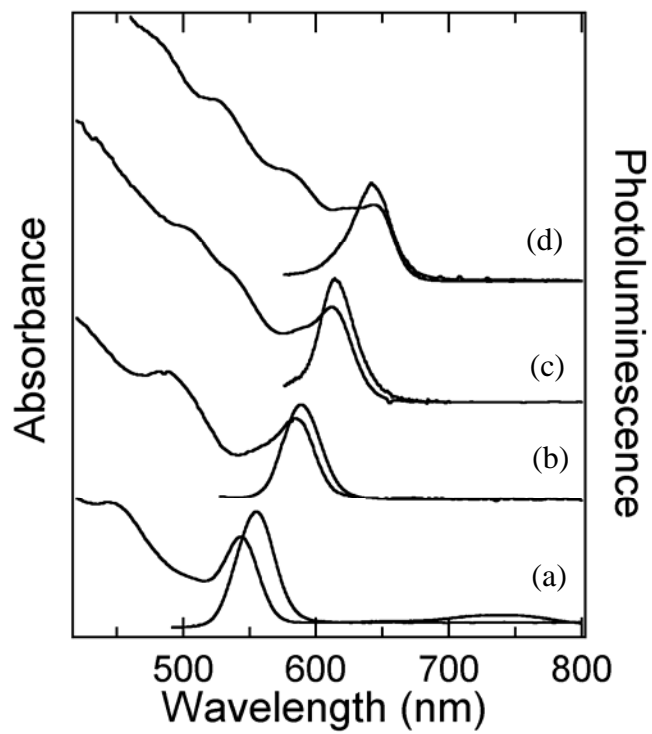


Figure 2.1b. Normalized absorbance and PL spectra of CdSe-HDA. Measured in toluene at 298 ± 2 K. Size selected (a) 3.7, (b) 4.5, (c) 6.0, and (d) 8.0 nm CdSe-HDA nanocrystals prepared by the single-source precursor route. Excitation was carried out at 488.0 nm and 1 mW of power.

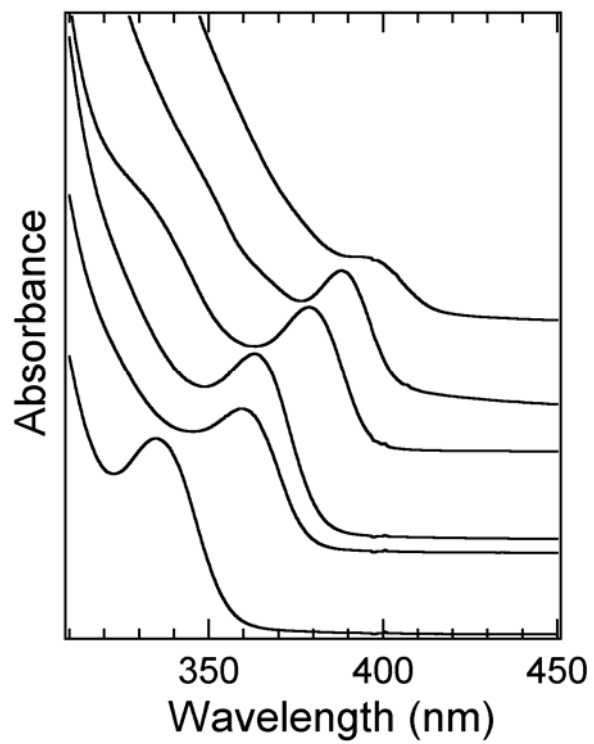


Figure 2.2a. Normalized absorbance spectra in toluene at 298 ± 2 K of batch <math>3.0 - 5.0 nm ZnSe-HDA nanocrystals prepared by the single source precursor route.

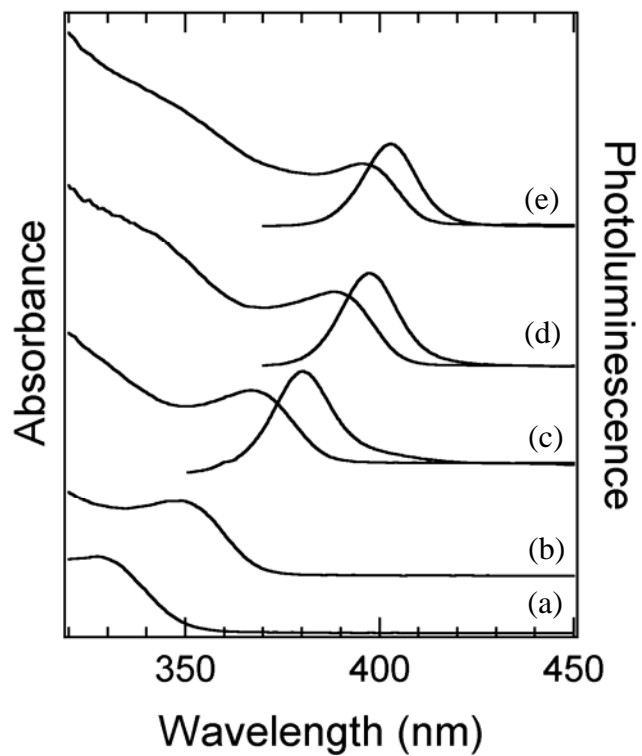


Figure 2.2b. Normalized absorbance and PL spectra in toluene at 298 ± 2 K of <3.0 (a) and (b), (c) 3.0, (d) 4.7, and (e) 5.0 nm ZnSe-HDA nanocrystals prepared by the single source precursor route. Excitation was carried out at 325.0 nm and 1 mW of power.

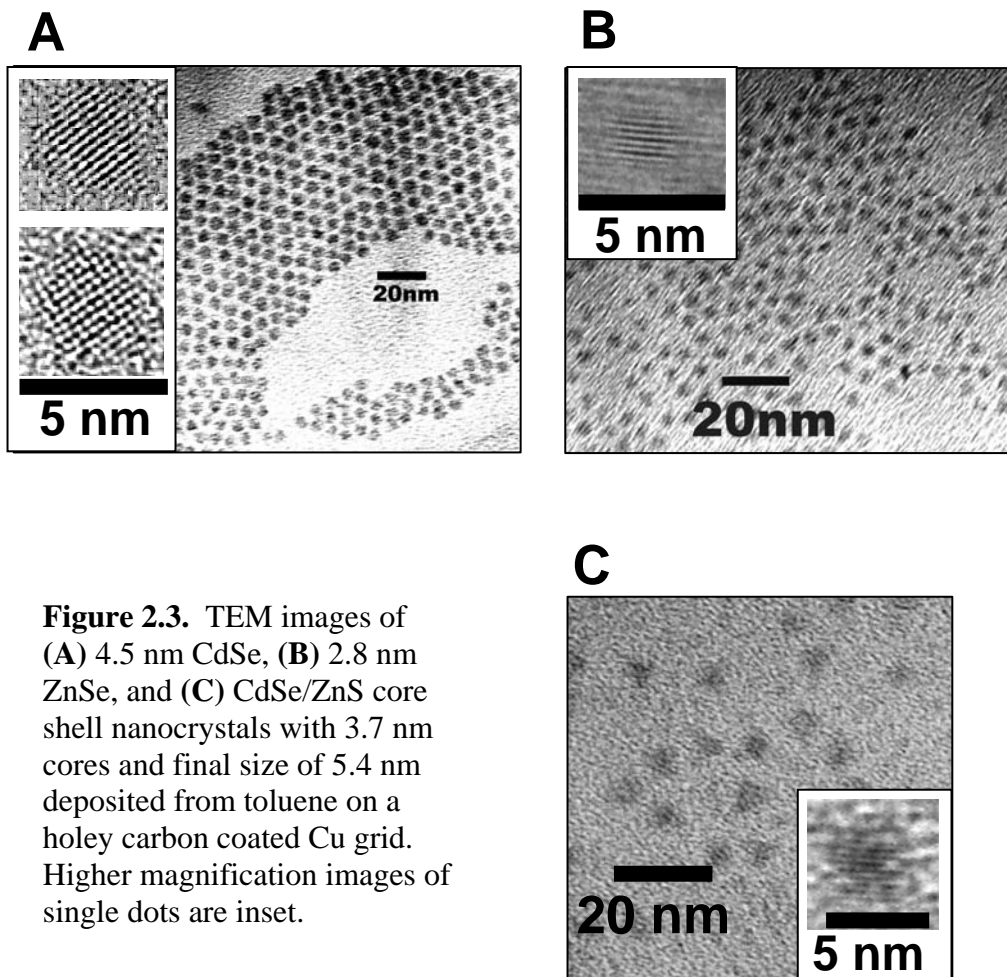


Figure 2.3. TEM images of (A) 4.5 nm CdSe, (B) 2.8 nm ZnSe, and (C) CdSe/ZnS core shell nanocrystals with 3.7 nm cores and final size of 5.4 nm deposited from toluene on a holey carbon coated Cu grid. Higher magnification images of single dots are inset.

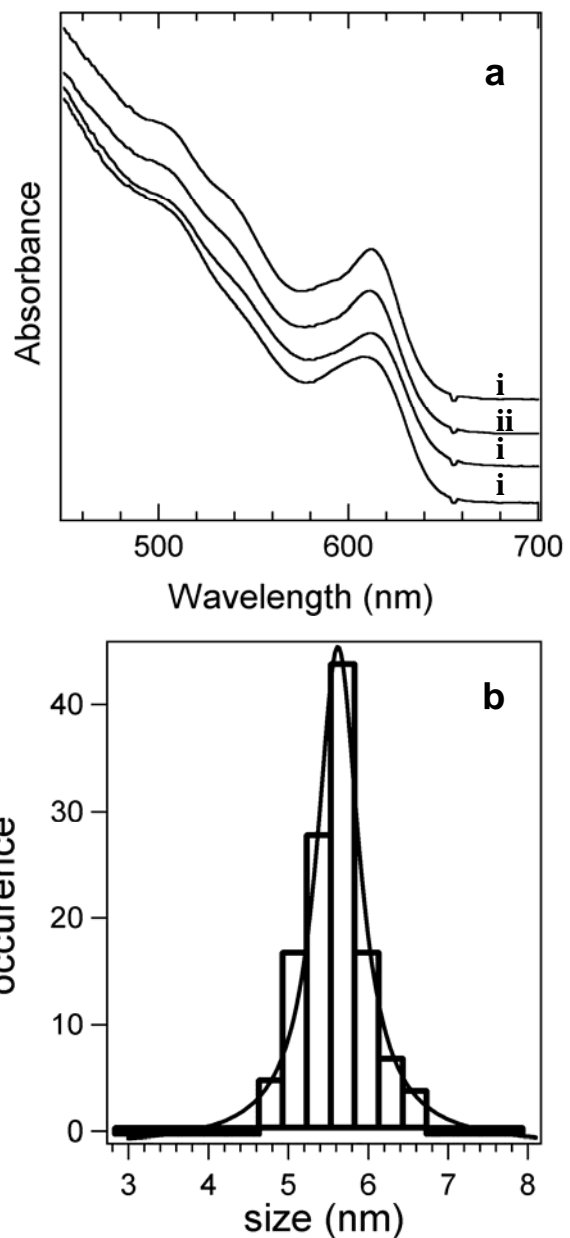


Figure 2.4. CdSe-HDA size dispersy. **(a)** Absorption spectrum in toluene at 298K showing selective precipitation of 6.0 nm CdSe-HDA showing dispersy ranging from 12% for out of batch sample (i) to 5% for a size selected sample (iv). **(b)** Size distribution of the final size selected sample was 6.0 ± 0.30 nm and was obtained by fitting a Lorentzian function to the data (shown).

Table 2.1. Statistics for II-VI nano-materials prepared from single source precursors.

| Size (nm) | Size dispersity | λ_{abs} (nm) | FWHM (nm) |
|------------------|----------------------|-----------------------------|-----------|
| CdSe | | | |
| 2.5 ^b | 5 % ^c | 472 | 33 |
| 3.7 | ~5 % ^a | 543 | 30 |
| 4.5 ^b | 5 % ^c | 574 | 32 |
| 5.5 | 5 % | 601 | 30 |
| 6.0 | 5 % | 612 | 36 |
| 8.0 | 5 % | 644 | 34 |
| 9.0 ^b | 5 % ^c | 655 | 33 |
| ZnSe | | | |
| <2.8 | ~ 10 % ^c | 328 | 26 |
| <2.8 | ~ 10 % ^c | 348 | 26 |
| 2.8 | ~ 7 % ^{a,c} | 363 | 22 |
| 4.5 ^b | ~7 % ^c | 388 | 22 |
| 4.8 | 7 % | 393 | 18 |

^aTEM image limits the accuracy of the dispersity analysis.

^bEstimated from λ_{abs}

^cEstimated from FWHM.

approximately a factor of two relative to the 3.7 nm (QY = 6%) and 4.5 nm (QY = 10%) HDA-passivated CdSe, consistent with earlier literature findings for inorganically vs. organically passivated materials.^{5, 9-15}

Both CdSe (hexagonal) and ZnSe (cubic zinc blende) exhibit pXRD diffraction patterns consistent with spherical nanoparticles.^{6, 16} In Figures 2.5a and 2.6, the observed diffraction features can be assigned to lattice reflections for CdSe and ZnSe. For comparison, a pXRD spectrum and TEM image of CdSe nano-rods is shown in figures 2.5b and c. In Figure 2.7, the observed diffraction features correspond to contributions from the CdSe and ZnS overlayer. The diffraction feature at 20.62 in 2θ (0.43 nm) corresponds to the hexadecylamine spacing on the surface of the nanocrystal.³¹⁻³²

The stoichiometry of the nanomaterials was observed to be Cd_{1.02}Se₁ based on peak area analysis of the Cd 3p and Se 4p spectral features from XPS data (Figure 2.8).

2.3.2 Reaction Mechanism.

The evolution of CdSe nanomaterials as a function of temperature in HDA is plotted in Figure 2.9. The formation of larger nanomaterials is reproducibly achieved above 220° C. ZnSe growth follows similar size versus temperature behavior, however the onset of growth occurs at higher temperature. Consistent with a thermodynamically driven reaction, the batch size-distribution broadens as the temperature increases. The nanomaterial reactions can be scaled between 1g/L

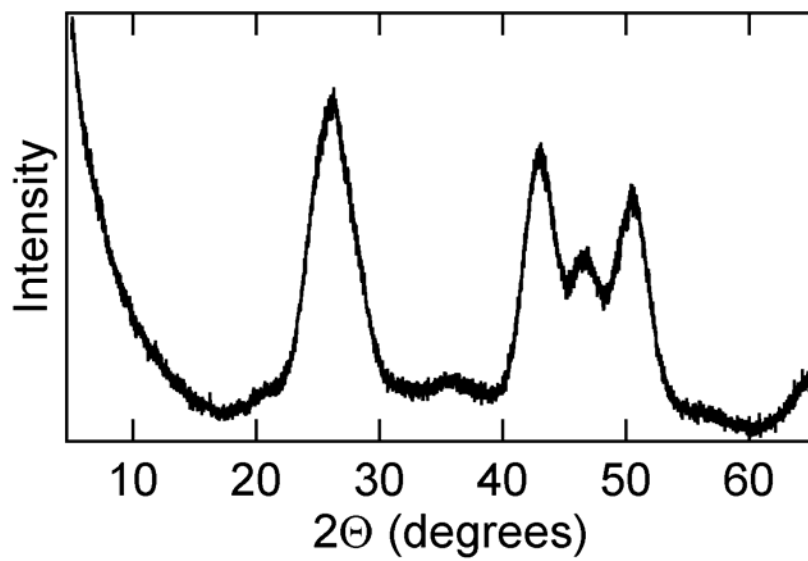


Figure 2.5a. PXRD of 4.0 nm CdSe prepared by the single source precursor method.

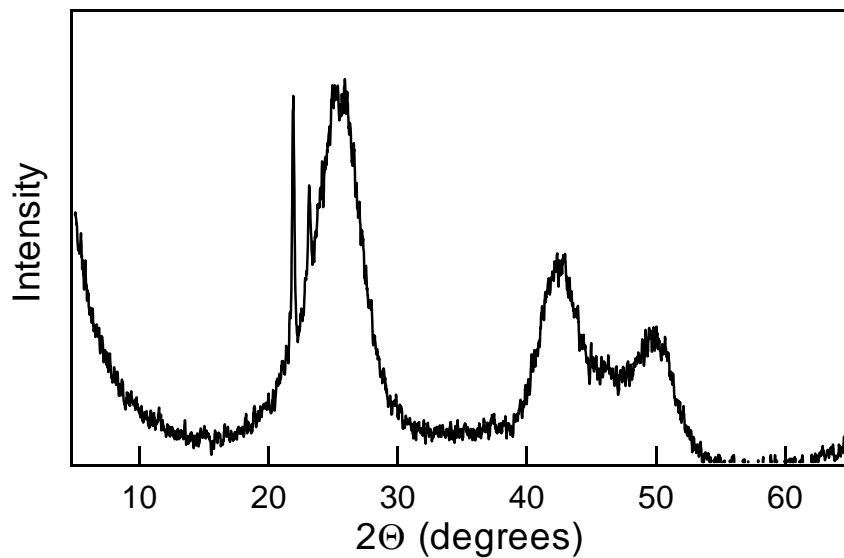


Figure 2.5b. PXR D of CdSe exhibiting rod morphology. Materials prepared by the single source precursor method.

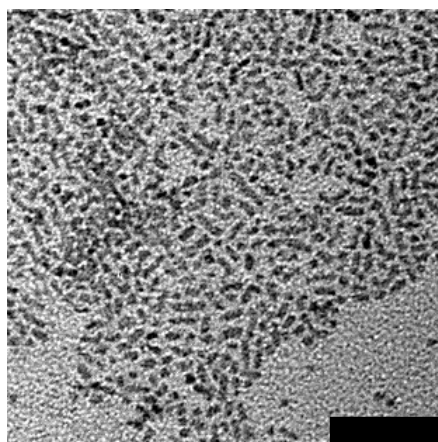


Figure 2.5c. TEM image of CdSe exhibiting rod morphology. Materials prepared by the single source precursor method. Scale bar is 50 nm.

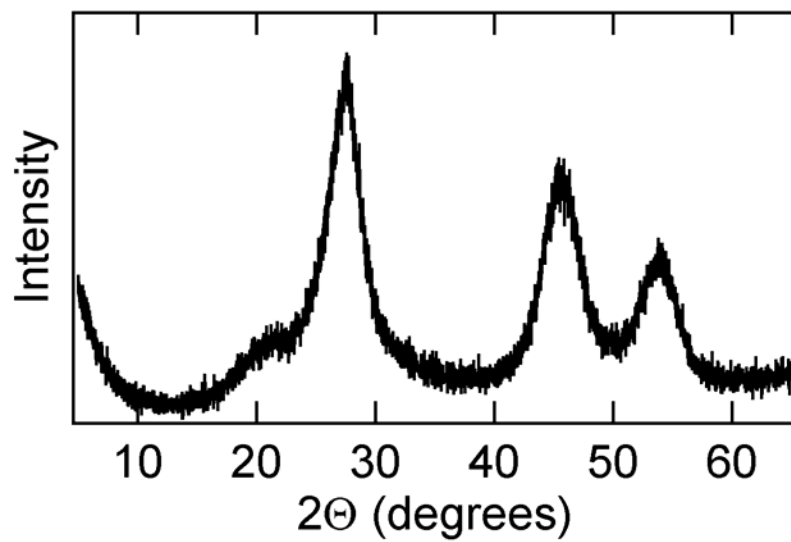


Figure 2.6. PXRD of 5.0 nm ZnSe. Material prepared by the single source precursor method.

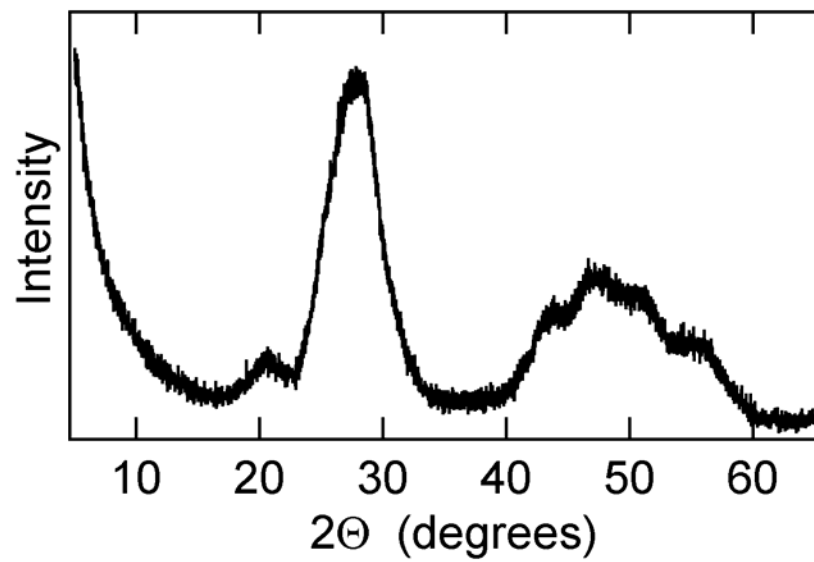


Figure 2.7. XRD of CdSe/ZnS nanomaterials. The materials have a 3.7 nm core, and a final diameter of 5.4 nm.

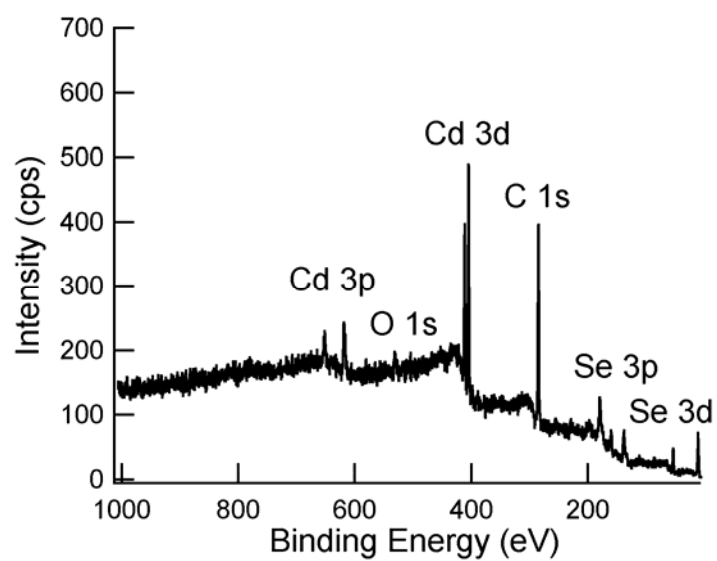


Figure 2.8. XPS survey spectrum of 7.0 nm CdSe. Material prepared in HDA. The peak positions are normalized to the C 1s position to minimize contributions from sample charging.

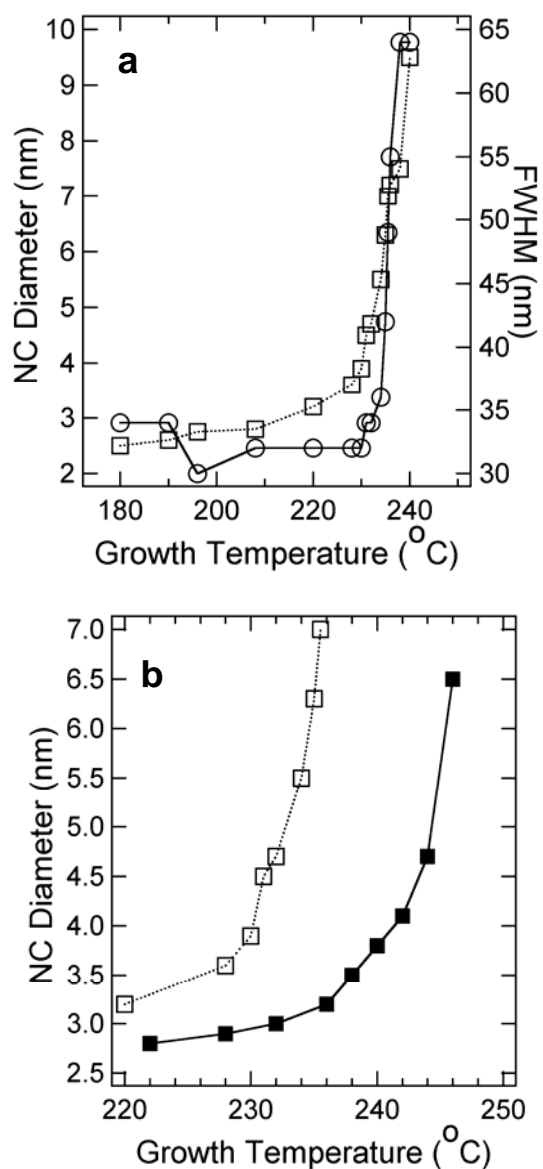


Figure 2.9. CdSe-HDA growth vs. temperature and precursor concentration. (a) Evolution of the size of the CdSe-HDA nanocrystals (squares) and the FWHM (circles) of the exciton absorbance band with growth temperature. Concentration of the single source precursor was 6 g/L in HDA. Nanocrystal size was determined from the position of the exciton band. (b) Concentration dependence of the growth rate for CdSe-HDA. Hollow and solid markers represent concentrations of 6 and 17 g/L of single source precursor in HDA respectively.

and 50 g/L, however it should be noted that 9.0 nm CdSe is achieved only in lower concentration reactions due to the higher thermal energy required for large concentration reaction batches. In Figure 2.9b, the dependence of concentration on the temperature for nanomaterial growth is indicated for reactions on the 6g/L and 17g/L scale.

Nanomaterials prepared from inorganic clusters exhibit size-dispersity annealing over a 24h period by lowering reaction temperatures to 180-190°C (Figure 2.10) as evidenced by the decrease in the FWHM of the band gap exciton peak. Additionally, a small (~ 3 nm) decrease is observed in the FWHM of the photoluminescence peak. No observable changes in size or absorption linewidth occurs for the nanomaterials under room temperature annealing conditions (Figure 2.11).¹⁶ Although the nanomaterials can be annealed for periods in excess of 48h, practical annealing times depend on the concentration of the reaction with the typical annealing time for the 6g/L synthesis being ~12-24h. A likely reaction mechanism for nanomaterial formation, based on the earlier studies of ring-opening and reconstruction of metal chalcogenide clusters, is proposed in Figure 2.12.

Growth of nanomaterials is observed in OA, DDA and TOP/TOPO but solvent choice influences size, size distribution, and stability of nanomaterials during growth. In OA and DDA, absorbance peaks attributable to large molecular clusters or very small nanomaterials were observed when CdSe nanomaterials were grown at lower temperatures (Figures 2.13 and 2.14, respectively). Nanomaterials grow to 3.7 nm in OA, while the largest sizes can be obtained in DDA and HDA.

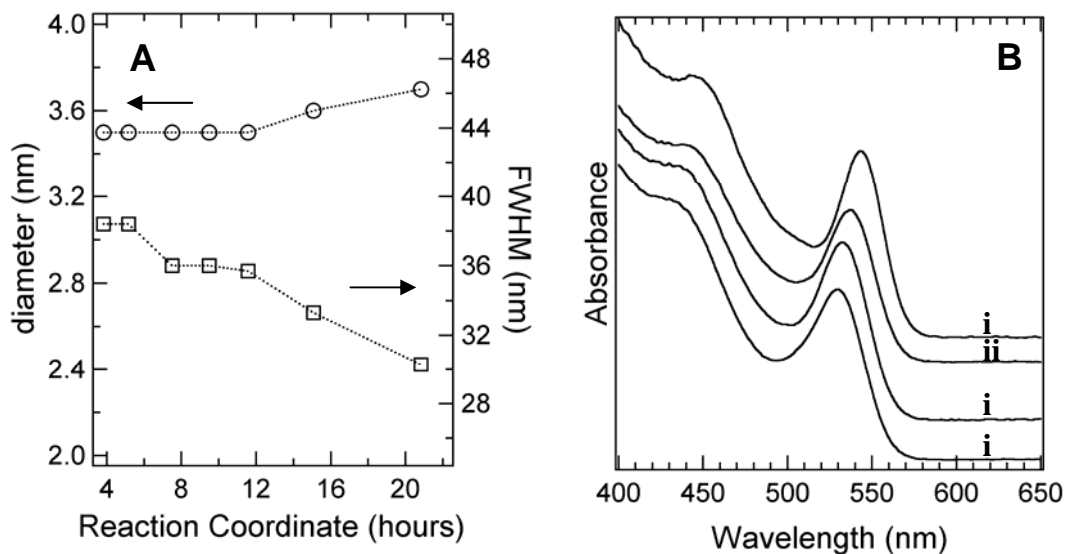


Figure 2.10. Temporal batch annealing of 3.5 nm CdSe-HDA nanocrystals at 180-190°C. **(A)** Change in diameter (circles) and FWHM of the exciton peak (squares) corresponding to a change in distribution from roughly 12% to roughly 5-6%. **(B)** Change in absorbance spectrum with temporal annealing at (i) 4 h, (ii) 11.5 h, (iii) 15 h, iv) 20 h. **(C)** Change in the photoluminescence spectrum with temporal annealing at (i) 4 h and (ii) 20 h.

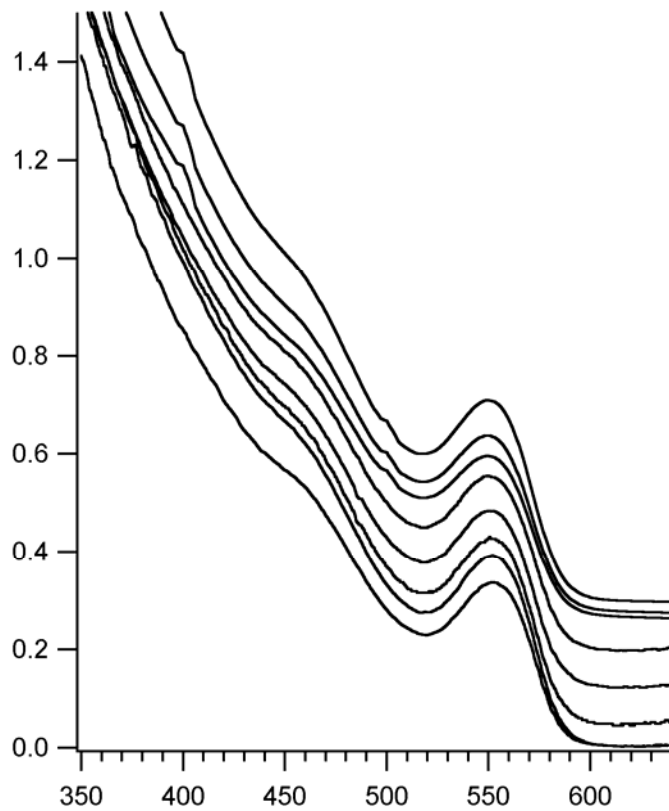


Figure 2.11. Ambient temperature annealing. Absorbance spectra in toluene at 298K of 4.0 nm CdSe-HDA nanocrystals prepared by the single-source precursor route and annealed in octylamine at room temperature for (lowest to highest traces) 0, 4, 18, 50, 75, 334, 363, and 403 hr.

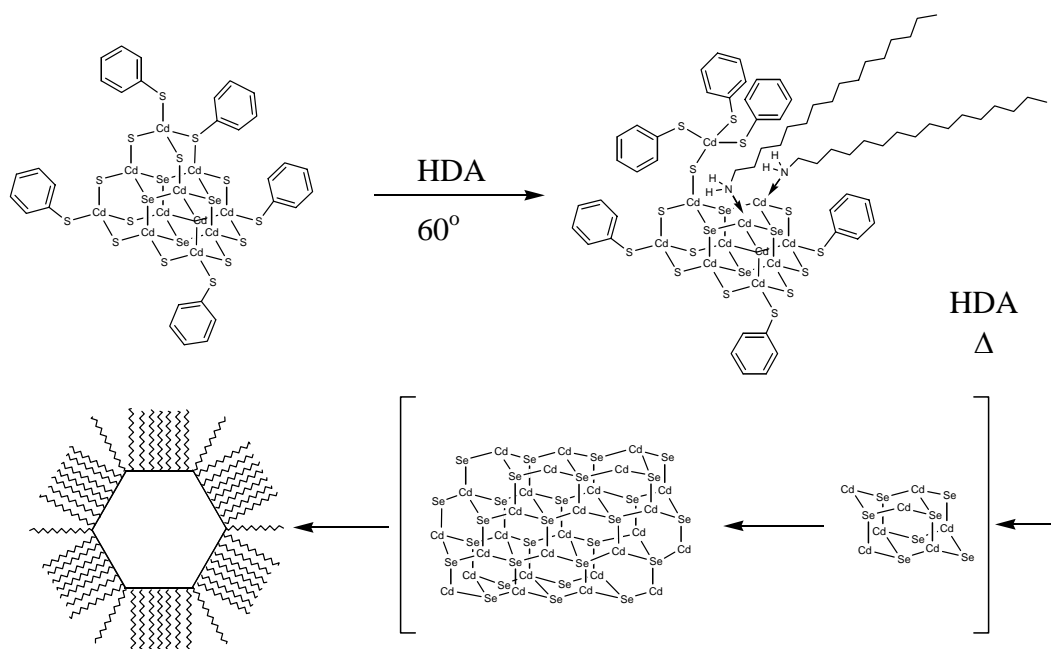


Figure 2.12. The proposed reaction mechanism for formation of CdSe nanocrystals from cluster precursors. The thiol and amine ligands for the clusters and nano-materials have been minimized for clarity.

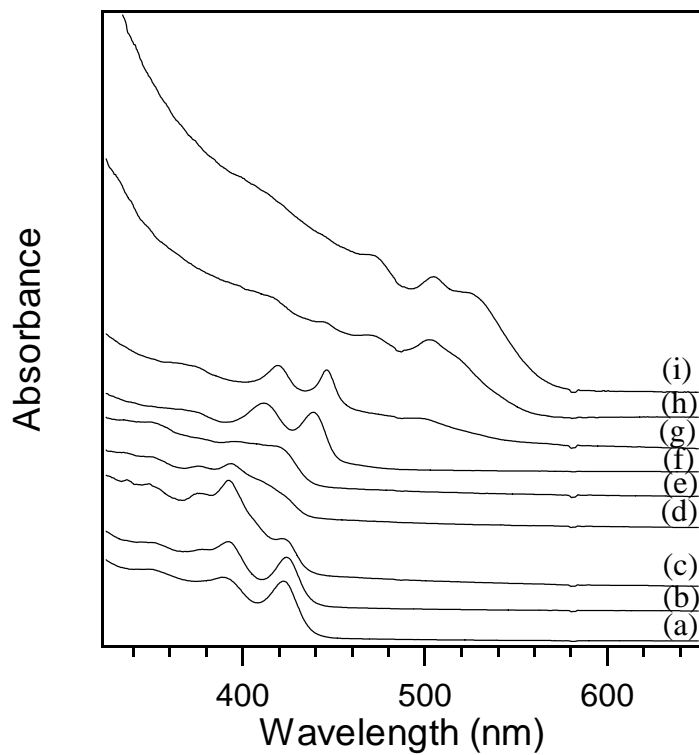


Figure 2.13. CdSe growth in octylamine solvent. The spectra were collected with the temperature of the reaction at (a) 25, (b) 45, (c) 62, (d) 74, (e) 85, (f) 130, (g) 172, (h) 174, and (i) 175°C.

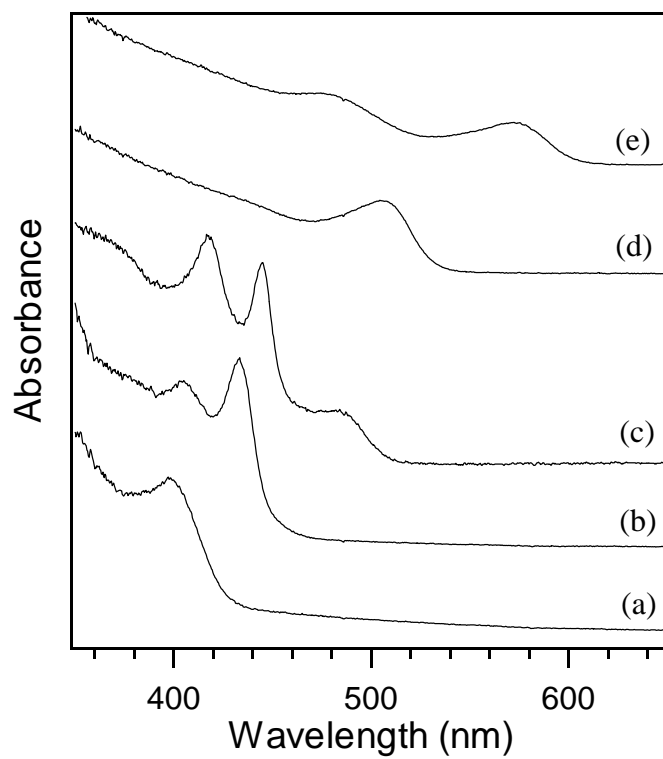


Figure 2.14. CdSe growth in dodecylamine solvent. The spectra were collected with the temperature of the reaction at (a) 44, (b) 102, (c) 148, (d) 172, and (e) 194°C.

Attempts to carry out this growth in TOP/TOPO resulted in broad absorbance peaks (Fig 2.15). Furthermore, growth of nanomaterials by directly introducing separate Cd and Se sources into the coordinating solvent, rather than single source precursors did result in nucleation, but was followed by uncontrolled growth, based on the absorption profiles (Fig 2.16). Attempts to re-initiate growth by introduction of the isolated nanomaterials into TOP/TOPO resulted in dissolution, while in HDA they grow but exhibit poor growth control (Figure 2.17).

Upon addition of additional cluster precursor to the reaction mixture a new nucleation event occurs. The nucleation is followed by growth with no evidence of particle dissolution (Figure 2.18). Intriguingly the new batch of nanocrystals grow to the same size as the nanomaterials already in the reaction rather than dissolve as would be expected from the Ostwald ripening mechanism.

2.4 Discussion.

2.4.1 Nanomaterial Growth.

Several lyothermal techniques, and simple ionic salt based growth techniques in coordinating solvents have been shown to produce high quality CdSe, CdS, CdTe, and ZnSe nanomaterials.^{6, 16, 18, 19} These methods are generalizable, but are often limited to smaller scale reactions due to the nature of the solvents, precursors, and reaction rates. Lyothermal methods typically require a pyrolytic step between 300 and 350°C, followed by sustained growth at temperatures in excess of 200°C.

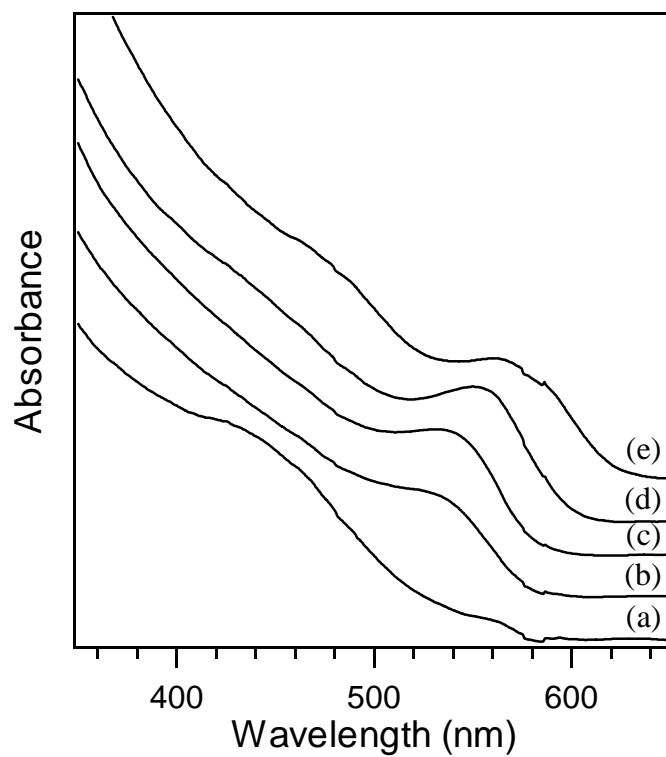


Figure 2.15. CdSe growth in TOP / TOPO solvent mixture. The spectra were collected with the temperature of the reaction at (a) 142, (b) 192, (c) 202, (d) 218, and (e) 250°C. Approximately 20 minutes after the collection of trace (e), the nanocrystals dissolved.

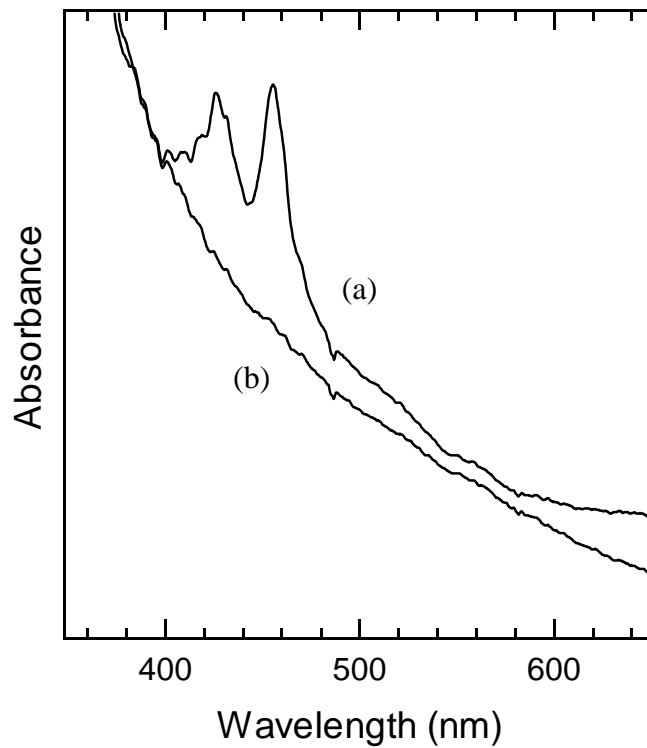


Figure 2.16. CdSe growth in hexadecylamine using $\text{Cd}(\text{NO}_3)_2$ and Se powder precursors. Absorbance spectrum (a) was collected with reaction mixture at 90°C . The absorbance of the reaction remained unchanged until 220°C when spectrum (b) was collected.

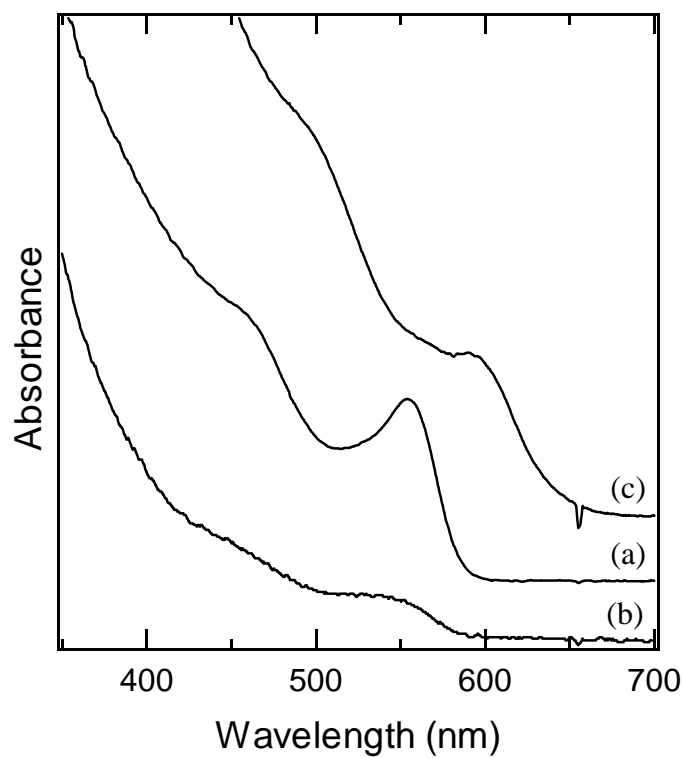


Figure 2.17. Heating isolated CdSe-HDA nanocrystals in coordinating solvents (a) TOP/TOPO resulted in dissolution of the materials after only 4 hours at 150°C (b). Heating the same materials in HDA resulted in the increase in the average nanocrystal size and size distribution as the temperature was maintained between 150 and 190°C for 11 days (c).

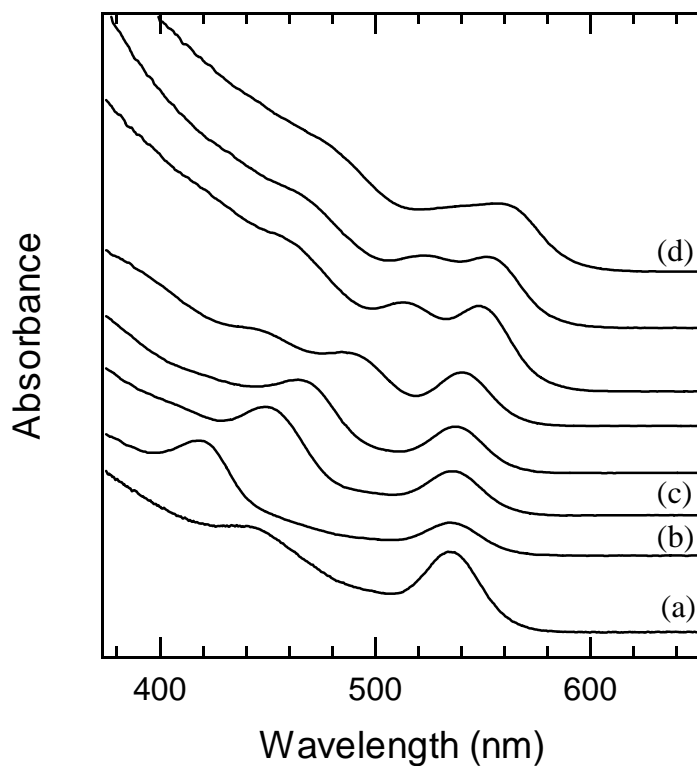


Figure 2.18. Addition of cluster precursors to a reaction in progress at 130°C (a) results in a second nucleation, and gives rise to two independent product distributions in one reaction mixture (b). Additional heating between 150 and 250°C over two days brings the second batch close in size to the first (c) – (d).

Synthetic preparations at room temperature in pyridine have produced CdSe materials of high quality, although the extrapolation to other II-VI materials has not been demonstrated and the reported sizes are below 5 nm. Application of a molecular cluster based single source precursor for nanomaterial growth offers an alternative synthetic methodology for material preparation that is readily generalized to both Cd and Zn chalcogenide systems, which exhibits neither size restrictions on nanoparticle growth or reaction scale restrictions due to associated dangers of pyrolytic starting materials or hazardous growth solvents. Furthermore, the lowered growth temperatures allow reasonably priced solvents to be employed, as long as the boiling points exceed 260°C.

The development of synthetic methodologies that allow generalizable, large scale reactions for the production of nanomaterials is important for the application of these materials in device technologies. The application of molecular cluster based single source precursors is an ideal approach for use as single source precursors since they can be prepared under ambient conditions, and purified by recrystallization techniques. This leads to an inorganic single source precursor that exhibits a long-term shelf-life under ambient conditions. Introduction of the precursor to a growth solvent at lower temperature (below 100°C) allows controlled growth of the desired II-VI (CdSe or ZnSe) nanomaterial through thermodynamic control. This results in a highly scalable and versatile synthetic methodology, allowing growth of well-formed CdSe and ZnSe nanomaterials (Figures 2.1-2.3). CdSe, ZnSe, CdSe/ZnS nanomaterials can be grown from inorganic clusters in

alkylamine solvents to produce materials that exhibit very narrow size dispersities (Figures 2.1-2.4) based on FWHM analysis of the exciton absorbance and emission band, and TEM analysis of the final product (Figure 2.3). The out-of batch samples exhibit size dispersities on the order of 10-12% (Figure 2.4a, trace (i)) with a significant improvement following selective precipitation of the materials from the reaction mixture (Figure 2.4a, trace (iv)). In Figures 2.1 and 2.2, the normalized absorbance and photoluminescence of size selectively precipitated CdSe and ZnSe nanocrystals exhibits a series of exciton bands, consistent with < 5% distribution in the nanomaterial size. Consistent with literature reports, the resolution of the second, third, fourth and fifth exciton are more clearly resolved in the larger nanomaterials.⁶ In figure 2.2, the broader absorptions for ZnSe arise from poorer size distributions, as well as complications arising from the inherent oxygen instability of ZnSe nanomaterials.

TEM data on samples isolated from the reaction mixture by selective precipitation for 4.5 nm CdSe, 5.4 nm CdSe/ZnS core shell, and 2.8 nm ZnSe exhibit distinct lattice fringes and well developed patterns that are consistent with the formation of a hexagonal (CdSe) or zinc blende (ZnSe) crystal lattice (Figure 2.3). The lack of observable glide plane defects in single QD TEM images, indicate the single source precursor method allows controlled growth to be achieved. Based on TEM analysis the nano-materials grow as spherical crystals. The average size and size distribution for the nanocrystals determined from the micrographs correlate well with those predicted from the position and line width of the exciton absorption

and photoluminescence band in Figure 2.1 and 2.2. The lack of observable defect emission for nanomaterials larger than 4.0 nm suggests well-formed II-VI materials can be prepared in HDA.

Due to the air-stability of the inorganic clusters, the reactions can be readily scaled to large-scale quantities (1-50g/L) without substantial adjustment to the growth methodology (Figure 2.9). Eliminating the pyrolytic event for QD formation lowers the temperatures for nanomaterial growth ($\sim 50 - 75^{\circ}\text{C}$) providing greater synthetic control and milder reaction conditions without a decrease in material crystallinity. Evidence for nanocrystal growth of CdSe arises from inspection of the absorption data as a function of the growth temperature in Figure 2.9a. Onset of nanomaterial growth occurs at temperatures in excess of 180°C . The increase in size of CdSe with increasing reaction temperature illustrates sustained growth is achievable in HDA for growth of particles up to 9 nm. Similar results are observed for ZnSe growth conditions except the upper limit for growth is ~ 5 nm under the above reaction conditions.

Alkylamines offer a convenient, inexpensive ligand for nanomaterial passivation, and have previously been employed as a solvent in the lyothermal preparation of ZnSe,¹⁶ and as a co-solvent in the synthesis of CdSe and CdSe/ZnS core/shell nanomaterials.³³ Due to the weaker interaction strength of the amine in comparison to a phosphine or thiol, the ligand (solvent) was expected to provide the necessary level of kinetic control to allow the use of inorganic clusters as a single source precursor for the growth of nanomaterials. The validity of this expectation

was demonstrated when isolated nanocrystals dissolved in a TOP/TOPO mixture upon heating, but appeared to undergo poorly controlled growth when heated in HDA (Figure 2.17). Hexadecylamine was chosen as the growth solvent due to moderate coordinating capability, its high boiling point, low cost, and evidence for surface stabilization of the product due to the chain-chain interactions on the surface, similar to observations in self-assembled monolayers on bulk Au surfaces and Au nanomaterials.^{20, 21} We have investigated octylamine (Fig. 2.13) and dodecylamine (Fig. 2.14) solvents with similar results, however lower boiling points tend to lead to smaller nanomaterials, or slower growth rates. Growth of materials in trioctyl phosphine (Fig. 2.15) also leads to nanomaterials, although the reactions require higher temperature and exhibit poor size and size distribution control. There is also a tendency of the product nanomaterials to dissolve at advanced stages of the reaction when the precursors are depleted. Reactions in DMF and pyridine do not lead to large materials, possibly due to the lower boiling points of the solvent or stronger coordinating ability of the solvent.

Intriguingly, the nanomaterials exhibit stability in the reaction mixture for extended periods of time (>72 h), allowing nanomaterial preparation in a batch reactor configuration. At temperatures below 100°C, no change or loss of the nanomaterials occur for extended periods of time in the reaction batch. Storage of the NC's either in hexadecylamine or in octylamine for extended periods under N₂ results in no degradation of either the optical absorption or luminescence properties for periods exceeding 400h. (Figure 2.11). Degradation studies under oxygen

indicate the material quality degrades rapidly with a broadening of the absorption, loss of solubility, and a shift to the blue, presumably from oxidation or ligand loss as previously observed in the literature. ZnSe material degradation is extremely rapid, requiring storage under anaerobic conditions.

The as grown nanomaterials exhibit annealing behavior at the desired size by lowering the growth temperature $\sim 30 - 40^{\circ}\text{C}$ and reacting for 6 – 12 h to achieve 5% size-dispersity out-of-batch (Figure 2.9). The change in linewidth from the absorption corresponds to a reduction in linewidth from 38 nm FWHM to 30 nm FWHM for the exciton (Figure 2.10) and an improvement in the resolution of the second excitonic transition (Figure 2.10b iv). The annealing may be attributable to either changes in the size distribution or improvement in the topology of the nanomaterials due to thermodynamically driven redistribution of the surface atoms. Thermal annealing of the reaction mixture (Figure 2.10) lowers the size distribution to $\sim 5\%$, allowing $\sim 90\%$ of the material to be collected with better optical properties. The annealing step presumably allows surface reconstruction eliminating vacancy sites³⁴ and/or glide plane defects in the nanomaterial core.¹¹ Further tightening of the distribution to $\leq 5\%$ by selected precipitation results in isolation of $\sim 50\%$ of the original product yield in the reaction batch.

Recapping CdSe nanomaterials with ZnS can be achieved by modification of the standard dimethylzinc organometallic routes.⁵ Capping of the nanomaterial surface with an inorganic shell (CdSe/ZnS) gives rise to an increase in the emission QY for CdSe from 6-10% to 20% as has been observed previously, corroborating the

formation of the inorganic layer. Close inspection of the XRD data in Supplemental Figure 2.3 indicates contributions from both the CdSe core and the ZnS overlayer. The absorption data for the core shell material predict a 3.7 nm CdSe nanomaterial, however, TEM imaging reveals materials of ~5.4 nm, further corroborating the inorganic capping. The low contrast for ZnS makes assignment of the shell-thickness difficult based on TEM analysis. This is in accord with previous results on inorganically passivated materials, which exhibit larger crystallite diameters in TEM arising from the shell. Interestingly, the core/shell materials appear triangular in the TEM image, suggesting lattice strain may influence the nanomaterial morphology via constraints on lattice plane capping.

2.4.2 Mechanisms for Growth

The Cd:Se ratio in CdSe nanomaterials has been reported to be 1.02 based on XPS analysis.¹⁸ The reaction of an $[M_{10}Se_4(SPh)_{16}]^{4-}$ cluster to form a MSe nanomaterial results in a stoichiometry for the reaction of M:Se 2.5:1, significantly higher than expected for the final product. Earlier studies suggest lability of the $Cd(SPh)_3^-$, which would still yield a M:Se stoichiometry of 1.5:1 based on the M_6Se_4 core of the cluster. XPS analysis of the CdSe nanomaterials grown in HDA show an ~1:1 ratio of Cd to Se in the final product (Figure 2.8). The absence of product stoichiometry in the precursor species requires the formation of Cd byproducts, which have not been identified. Several possibilities including Cd amine compounds, Cd thiophenolate and disulfide species are expected form and be

removed with the excess coordinating solvent during nanomaterial isolation. Excess thiol appears to form disulfide byproducts that precipitate as a white solid in the reaction mixture. In order to achieve the proper stoichiometry in the final materials a thermodynamic nucleus formation step must initiate the reaction followed by a reconstruction of the materials to a thermodynamically favored structure.

Several mechanisms for nucleus formation based upon various degrees of cluster fragmentation can be proposed. The mechanism for nucleus formation and growth of nanomaterials must account for the observation of a tight batch distribution, low temperature nanomaterial growth, and the capacity to reconstruct from a zinc blende core in the clusters to a hexagonal lattice in the CdSe nanomaterial.

One potential mechanism involves the fragmentation of the M_{10} cluster into M^{2+} and Se^{2-} or poly metal-chalcogenide active species, similar to those of a traditional lyothermal synthesis, followed by nucleation and growth. Because the cluster precursors are more stable than the pyrophoric starting materials normally used in such syntheses and the degradation takes place at a considerably lower temperature than normally employed in such reactions, the introduction of active species into the reaction mixture would be very slow resulting in poor separation of nucleation and growth steps and limiting the quality of the product nanomaterials. The fragments would be expected to produce larger size distributions than observed in the absorption spectra and TEM in Figure 2.1 – 2.3, due to virtually uncontrolled epitaxial growth. Attempts to prepare CdSe nanomaterials from the direct addition of either $Cd(NO_3)_2$ or $[Cd_4(SPh)_{12}]^{4+}$ and Se powder or triphenylphosphine selenide

in HDA result in the formation of what appears to be a large CdSe cluster at lower reaction temperatures followed by the appearance of a featureless spectrum indicative of a nanomaterial with a wide size distribution as reaction temperature is increased (Figure 2.16) supporting the lack of complete cluster fragmentation as the initiation step. Broad distributions arising from poor nuclei formation resulting in failure to separate growth have been observed previously in the literature.²² Intriguingly, addition of HDA solubilized Se or Cd in the form of $[M_4(\text{SPh})_{12}]^{4-}$ to growing CdSe nanomaterials has no observable effect on nanomaterials growth rate suggesting neither Cd thiophenolate cluster byproducts or complete cluster fragmentation may not be a significant contributor to nanomaterial growth. Another result that is inconsistent with extensive degradation of clusters in solution is presented in Figure 2.18. When a sample of $\text{Li}_4[\text{Cd}_{10}\text{Se}_4(\text{SPh})_{16}]$ was added to a CdSe growth in progress, a second nucleation event was observed. Subsequent absorbance spectra suggest that the reaction mixture contains two nanomaterial growth reactions simultaneously. The smaller nanomaterials grow faster at the same temperature, as is expected from their higher surface energies, with the average nanocrystal diameter of the second reaction eventually catching up to that of the first.

An alternative mechanism is the cluster degradation is very slow, with the mostly intact core acting as a partial nucleus and nanomaterial growth proceeds by scavenging free M and Se atoms in solution. This mechanism is unsupported by the exchange dynamics of the individual clusters as observed in previous NMR and

ESMS analysis.²³⁻²⁵ The M_{10} systems in a donor solvent, such as CH_3CN , DMF, pyridine, DMSO, exhibit rapid ligand and metal ion exchange at the apex of the clusters, which suggests the clusters will not remain intact upon addition to a nucleophilic solvent.²⁵ Although, the lack of fragmentation would produce well formed materials, the mechanism is inconsistent with exchange dynamic studies on clusters and can not account for the structural change from a cubic zinc blende for the Cd_{10} cluster to the hexagonal crystallographic structure for the nanocrystals.

A more likely mechanism for nanomaterial growth can be proposed based upon a combination of fragmentation via ring opening and subsequent ligand exchange (Figure 2.12). A similar mechanism involving facile ring opening, followed by metal or ligand exchange, has been proposed for a series of metal-chalcogenide clusters of various nuclearity based upon NMR and ESMS analysis of Cd and Zn clusters in solution in the presence of incoming ligands or metal ions.²³⁻²⁵ In fact, several researchers have proposed that formation of Cd_{20} and Cd_{32} clusters from Cd_{10} is initiated by ring opening, followed by attack of the exposed Cd atom at the electron rich, triply bound chalcogenide ion, and subsequent loss of the apical $[\text{Cd}(\text{SPh})_3]^-$ caps.^{26, 27} In effect, the cluster acts as a template for formation of a larger nuclearity structure. This mechanism would result in the formation of uniform nuclei when the cluster is introduced into the solvent at low temperature. The absorbance features observed at low temperatures during nanomaterial synthesis in OA and DDA (Figs. 2.13 and 2.14) could be assigned to large clusters or small (1.8 nm diameter) nanocrystals. This explanation accounts for the observed

nanomaterial monodispersity, while allowing structural reorganization to arise from a series of ring-opening events that produce a thermodynamically favored lattice configuration. Although the initial Cd₁₀ structure is a cubic zinc blende lattice, the surface energetics of nucleation leads to formation of a hexagonal lattice for the nanomaterials of CdSe. In ZnSe, the cubic zinc blende lattice of the Zn₁₀ precursor is maintained in the final structure. It is interesting to observe the rate of this process

2.5 Conclusion.

Molecular clusters of metal chalcogenide systems, which exhibit facile ligand exchange and structural rearrangements, are analogues of the bulk metal chalcogenide semiconductor lattice.^{25, 28} Application of molecular inorganic precursors offers a unique opportunity for growth of nanomaterials at lowered temperatures by providing intact nuclei in HDA for the formation of CdSe nanocrystals. The precursor, (Li)₄[Cd₁₀Se₄(SPh)₁₆] can be envisioned as a fragment of the bulk structure, that acts as an effective molecular template for growth.^{1,29,30} Controlled growth of nano-crystalline II-VI materials is then achieved by thermal control in a moderately coordinating solvent to produce large quantities of nanocrystals that exhibit well defined crystalline faces, and narrow size / shape dispersion. The use of inorganic clusters in a 'seeded growth' approach results in an inherent versatility of this method. Extension of this methodology allows formation

of novel binary and ternary semiconductor systems at the nano-scale, currently being pursued in our group.

2.6 References.

- 58) Dance, I. G.; Choy, A.; Scudder, M. L. *J. Am. Chem. Soc.* **1984**, *106*, 6285.
- 59) Crystalline $[\text{Cd}_{10}\text{Se}_4(\text{SPh})_{16}]^{4-}$ may be prepared in a 2-step synthetic reaction to form an air stable, crystalline inorganic cluster. Briefly the reaction is carried out through the formation of $[\text{Cd}_4\text{SPh}_{12}]^{2-}$ by the direct addition of a stoichiometric amount of $\text{Cd}(\text{NO})_2$ to a methanol solution containing a 1:1 mole ratio of triethylamine and thiophenol under ambient conditions. Triethylamine is added to deprotonate the thiophenol. Addition of either LiNO_3 or TMACl (tetramethyl ammonium chloride) allows isolation of a crystalline product. Conversion of $[\text{Cd}_4\text{SPh}_{12}]^{2-}$ to $[\text{Cd}_{10}\text{Se}_4\text{SPh}_{16}]^{4-}$ is accomplished by treatment of a room temperature acetonitrile solution of $[\text{Cd}_4\text{SPh}_{12}]^{2-}$ with Se under N_2 . Single crystals can be generated by recrystallization from hot acetonitrile..
- 60) Dimethylzinc is pyrophoric in the presence of O_2 due to the highly exothermic formation of ZnO. TOP is oxygen sensitive with a propensity for formation of the phosphine oxide and should therefore be handled under airless conditions.
- 61) Demas, J. N.; Crosby, G. A. *J. Phys. Chem.* **1971**, *75*, 991.
- 62) Hines, M. A.; Gytot-Sionnest, P. *J. Phys. Chem.* **1996**, *100*, 468-71.

- 63) Murray, C. B.; Norris, D. J.; Bawendi, M. G. *J. Am. Chem. Soc.* **1993**, *115*, 8706.
- 64) Steigerwald, M. L. *Polyhedron* **1994**, *13*, 1245.
- 65) Katari, J. E. B.; Colvin, V. L.; Alivisatos, A. P. *J. Phys. Chem.* **1994**, *98*, 4109.
- 66) (a) Danek, M.; Jensen, K. F.; Murray, C. B.; Bawendi, M. G. *Chem. Mater.* **1996**, *8*, 173-80. (b) Dabbousi, B. O.; Rodrigues-Viejo, J.; Miculek, F. V.; Heine, J. R.; Mattousi, H.; Ober, R.; Jensen, K. F.; Bawendi, M. G. *J. Phys. Chem. B.* **1997**, *101*, 9463.
- 67) Hoener, C. F.; Allan, K. A.; Bard, A. J.; Campion, A.; Fox, M. A.; Mallouk, T. E.; Webber, S. E.; White, J. M. *J. Phys. Chem.* **1992**, *96*, 3812.
- 68) Kortan, A. R.; Hull, R.; Opila, R. L.; Bawendi, M. G.; Stiegerwald, M. L.; Carroll, P. J.; Brus, L. E. *J. Am. Chem. Soc.* **1990**, *112*, 1327-32.
- 69) Tian, Y.; Newton, T.; Kotov, N. A.; Guldi, D. M.; Fendler, J. H. *J. Phys. Chem.* **1996**, *100*, 8927.
- 70) Peng, X.; Schlamp, M. C.; Kadavanich, A. V.; Alivisatos, A. P. *J. Am. Chem. Soc.* **1997**, *119*, 7019.
- 71) Revaprasadu, N.; Malik, M. A.; O'Brien, P.; Wakefield, G. *Chem. Com.* **1999**, 1573-74.
- 72) Talapin, D. M.; Rogach, A. L.; Kornowski, A.; Haase, M.; Weller, H. *Nano Lett.* **2001**, *1*, 207.
- 73) Hines, M. A.; Gyot-Sionnest, P. *J. Phys. Chem.* **1998**, *102*, 3655.

- 74) For room temperature annealing, a hexadecylamine dispersion of CdSe was diluted threefold with dry octylamine. Dilution in octylamine allows the reaction to be maintained at RT without solidification of the HDA. Room temperature annealing was carried out for 400 hours under an N₂ atmosphere with no observable change to the absorbance.
- 75) Katari, J. E. B.; Colvin, V. L.; Alivisatos, A. P. *J. Phys. Chem.* **1994**, *98*, 4109.
- 76) (a) Peng, Z. A.; Peng, X.; *J. Am. Chem. Soc.* **2001**, *123*, 183. (b) Peng, Z. A.; Peng, X.; *J. Am. Chem. Soc.* **2001**, *123*, 1389. (c) Qu, L.; Peng, Z. A.; Peng, X.; *Nano Letts.* **2001**, *1*, 333.
- 77) Alvarez, M. M.; Khoury, J. T.; Schaaff, T. G.; Shafigullin, M.; Vezmar, I.; Whetten, R. L. *Chem. Phys. Letts* **1997**, *266*, 91-98.
- 78) Hostetler, M. J.; Wingate, J. E.; Zhong, C-J.; Harris, J. E.; Vachet, R. W.; Clark, M. E.; Londono, J. D.; Green, S. J.; Stokes, J. J.; Wignall, G. D.; Glish, G. L.; Porter, M. D.; Evans, N. D.; Murray, R. W. *Langmuir*, **1998**, *14*, 17-30.
- 79) Peng, X.; Wickham, J.; Alivisatos, A. P. *J. Am. Chem. Soc.* **1998**, *120*, 5343.
- 80) Gaumet, J. J.; Strouse, G. F. *J. Am. Soc. Mass. Spectrom.* **2000**, *11*, 338.
- 81) Løver, T.; Bowmaker, G.; Seakins, J. M.; Cooney, R. P.; Henderson, W. J. *Mater. Chem.* **1997**, *7*, 647.
- 82) Løver, T.; Henderson, W.; Bowmaker, G.; Seakins, J. M.; Cooney, R. P. *Inorg. Chem.* **1997**, *36*, 3711.

- 83) Raola, O. E.; Woessner, S. M.; Strouse, G. F. *manuscript in progress*.
- 84) Wang, Y.; Harmer, M.; Herron, N. *Israel J. Chem.* **1993**, *33*, 31-39.
- 85) Hagen, K. S.; Stephan, D. W.; Holm, R. H. *Inorg. Chem.* **1982**, *21*, 3928-36.
- 86) Dance, I.; Fisher, K. *Prog. Inorg. Chem.* **1994**, *41*, 637 and references herein.
- 87) Metallothionein: Synthesis, Structure, and Properties of Metallothioneins, Phytochelatins, and Metal-Thiolate Complexes; (Eds.: M. J. M. Stillman, C. F. Shaw III, K. T. Suzuki) VCH Publishers, New York, **1992**.
- 88) Chen, S.; Liu, W. *Mater. Res. Bull.* **2001**, *36*, 137-43.
- 89) Yun, S. K.; Maier, J. *Inorg. Chem.* **1999**, *38*, 545-49.
- 90) Talapin, D.V.; Rogach, A.L.; Kornowski, A.; Haase, M.; Weller, H. *Nano Letts* **2001**, *1*, 207-211
- 91) Donega, C. M.; Hickey, S. G.; Wuister, S. F.; Vanmaekelbergh, D.; Meijerink, A. *J. Phys. Chem. B* **2003**, *107*, 489-96.

Chapter 3. Synthesis of CdS and ZnS nanomaterials.

3.1 Introduction

The most thoroughly investigated II-VI nanomaterial has been CdSe. The more ionic sulfide semiconductor materials received less attention because the synthetic methods are less developed and the materials are more susceptible to photodegradation.¹ The more ionic character of these materials, however, results in larger band gap energies which makes the nanomaterials potentially more useful in areas like catalysis and energy exchange.

This chapter presents an extension of the seeded growth method using inorganic molecular clusters to the sulfide family of II-VI nanomaterials. The general procedure for the sulfide synthesis is the same as for the selenide materials. The $L_4[M_{10}S_4(SPh)_{16}]$ precursors are placed into a dry long chain amine coordinating solvent and the temperature raised to achieve growth. The quality of product materials, however, is not as good as for CdSe. The size range of product materials is much smaller and the band gap photoluminescence much less intense.

3.2 Experimental.

$(X)_4[M_{10}S_4(SPh)_{16}]$ ($X = Li^+$ or $(CH_3)_3NH^+$ and $M = Cd$ or Zn and SPh is phenyl thiolate) were prepared as described in Chapter 2 by using a Li^+ cation instead of a tetramethylammonium cation for isolation of the product cluster. Hexadecylamine (HDA, 90%), was purchased from Acros Chemical and used

without further purification. Solvents used for nanomaterials isolation and spectroscopy were purchased from Fisher Scientific and used without further purification. Absorbance, photoluminescence, TEM, and pXRD measurements were carried out as described in Chapter 2 for the metal selenide nanomaterials.

Preparation of amine capped CdS nanomaterials. Approximately 24 g of HDA was degassed under vacuum at 120°C. The temperature of the solution was then lowered to 65-70°C. To the stirred solution of HDA under N₂, 300 mg (0.10 mmol) of (Li)₄[Cd₁₀S₄(SPh)₁₆] was added using standard airless techniques and the solution temperature raised to 190-200°C (0.2°C / minute). Growth rates depend on the initial reactant concentration and can be followed by absorption spectroscopy. The temperature ramp rate can be increased and the nanomaterials can be grown at higher temperatures, but it is observed that those conditions always result in a relatively large size distribution and absence of PL in the product nanomaterials. The CdS can be isolated by selective precipitation by addition of 100 ml of anhydrous MeOH, and isolating via centrifugation. Excess HDA is removed by subsequent re-suspension in toluene and isolation by centrifugation.

Preparation of amine capped ZnS nanomaterials. An N₂(g) degassed sample of the molecular cluster Li₄[Zn₁₀S₄(SPh)₁₆] (where ⁻SPh is the thiophenylate group) was added to molten hexadecylamine (160°C) under N₂(g). The temperature of the reaction was slowly increased and nanocrystal growth was monitored by periodic removal of small aliquots of the reaction mixture and measurement of their UV absorbance. Since ZnS nanomaterials absorb in the same region as HDA, it is

important to carry out a crude isolation of ZnS materials before a spectrum is collected. Larger aliquots of the reaction mixture were collected when a desired nanomaterial size was reached. The nanomaterials were stored under N₂ in the dark in the solidified growth solution at -20 °C. Isolation of the nanomaterials from the growth solution by methyl alcohol induced precipitation was carried out under airless conditions due to the high propensity for particle oxidation.

3.3 Results

Selected absorption and emission spectra of CdS, and ZnS nanocrystals grown from $[M_{10}S_4(SPh)_{16}]^{4-}$ (M = Cd or Zn, SPh is thiophenol) are shown in Figures 3.1 and 3.2. The two growth progressions show well-defined excitonic structure and size quantization. The average nanoparticle diameters were estimated using absorption spectroscopy,²⁻⁵ and verified by TEM analysis. Representative TEM analyses of ZnS nanocrystals exhibiting uniform spherical morphology and lattice fringes which indicate a high degree of crystallinity are illustrated in Figure 3.3. Statistical analysis of out-of-batch materials by TEM (Figure 3.3) shows that ~12% size dispersities for the zinc sulfide can be achieved without any post synthesis size selection. A thorough study of the average sizes and size distributions of 2.5 to 3.7 nm ZnS-HDA samples by a novel mass spectrometric method is presented in Chapter 4. Neither CdS nor ZnS gave reproducible band gap photoluminescence. Powder XRD analysis of CdS shows that the nanomaterials exhibit the cubic zinc blende PXRD diffraction patterns (Figures 3.4).

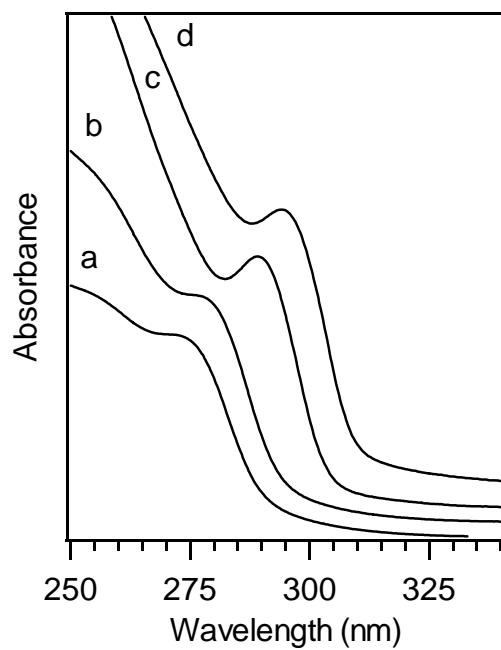


Figure 3.1. Normalized absorbance spectra in chloroform at 298 ± 2 K of batch a) 2.5, b) 2.9, c) 3.5 and d) 3.7 nm ZnS-HDA nanocrystals.

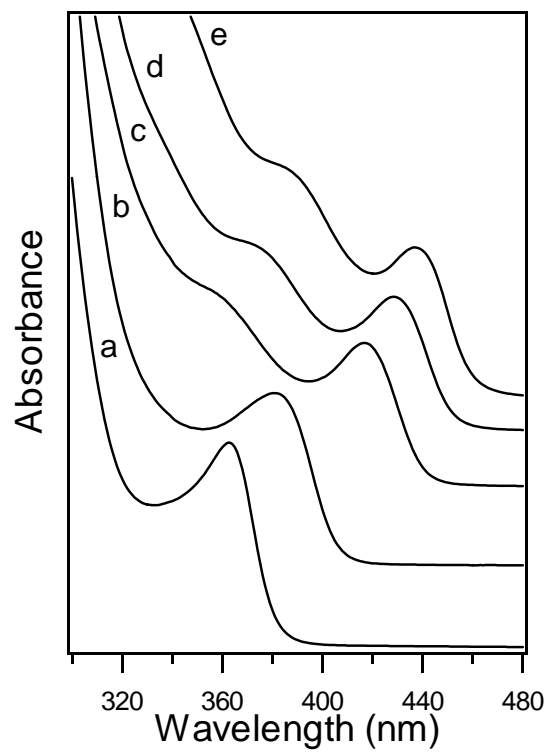


Figure 3.2. Normalized absorbance spectra in chloroform at 298 ± 2 K of batch a) 2.5, b) 3.0, c) 4.2, d) 4.5, and e) 5.0 nm CdS-HDA nanocrystals.

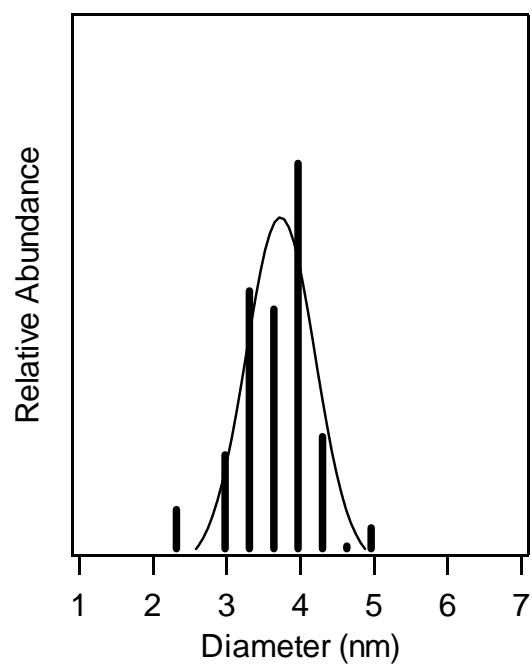


Figure 3.3. Size distribution of 3.7 ± 0.47 nm ZnS-HDA nanocrystals. Curve is a Gaussian function fit to the data. Inset shows one of the micrographs used to measure the size distribution. Scale bar is 20 nm.

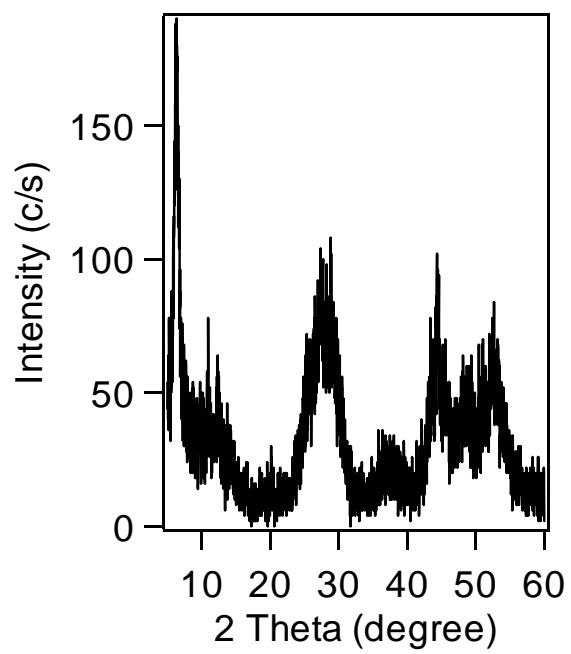


Figure 3.4. pXRD of 4.4 nm CdS-HDA nanocrystals.

3.4 Discussion.

It is important to initiate CdS growth at low temperatures and increase the temperature slowly. Increasing the reaction temperature too quickly results in the formation of materials that exhibit photoluminescence from trap states only. ZnS nanomaterials growth follows a similar trend in size with increasing temperature, however the onset of growth occurs at higher temperature. Consistent with a thermodynamically driven reaction, the batch size-distribution in both materials broadens as the temperature increases. The nanomaterial reactions can be scaled between 1g/L \rightarrow 25 g/L, however it should be noted that larger nanomaterial sizes are achieved only in lower precursor concentration reactions due to the higher thermal temperatures required for large concentration reaction batches.

Unlike the CdSe nanomaterials described in chapter 2, annealing of the products (lowering of the absorbance FWHM) does not occur when the temperature of the CdS reaction mixture is lowered for extended periods of time. Annealing experiments were carried out for several weeks with CdS nanocrystals without yielding any results. Attempts to anneal ZnS nanomaterials by letting them at a lower-than-growth temperature resulted in broadening of the absorbance features within minutes. This low stability in the amine solvent is most likely the result of the weak interaction between surface Zn atoms and the amine head group. The weakness of this interaction also makes it impossible to carry out ligand exchange on ZnS nanomaterials. While they can easily be isolated from the HDA growth

solution and dispersed in pyridine, the first flocculation step with a non solvent renders them insoluble in any common laboratory solvent. The weak passivating action of the amine also makes it necessary to store ZnS materials at low temperatures to prevent uncontrolled growth and size distribution broadening.

The growth mechanism of the CdS nanomaterials is most likely similar to the mechanism previously proposed for CdSe. It is observed that if additional precursor materials are added to a growth in progress the clusters don't dissolve to form Cd and S monomer species like those present in the lyothermal synthesis. Instead, a second nucleation event is observed as evidenced by the formation of an absorbance feature of small CdS nanocrystals to the blue of the feature present in the growth mixture (Figure 3.5). Much like was observed in the CdSe materials, the newly nucleated product grows until it reaches the same size as the materials already in solution.

3.5 Conclusion

The results presented in this section demonstrate the applicability of the molecular cluster precursor method to the synthesis of a wide variety of II-VI nanomaterials. While the quality of the products was lower than that observed for

the ubiquitous CdSe, the crystallinity and size distributions were better than those reported for products of various arrested precipitation syntheses carried out at room temperature.⁶

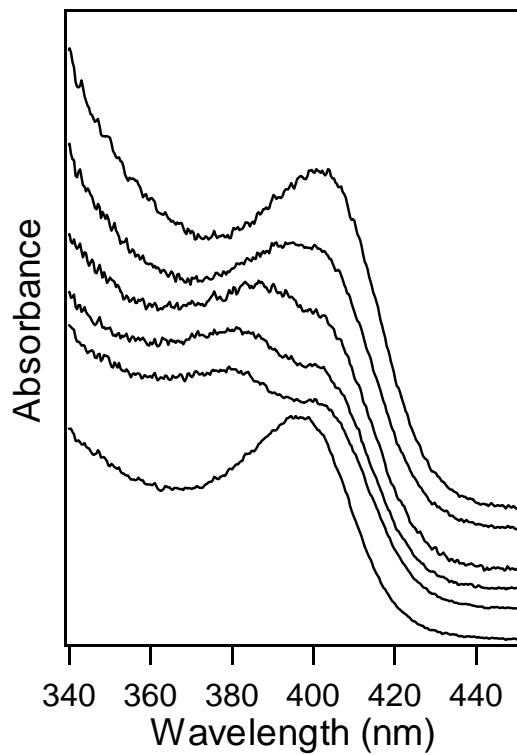


Figure 3.5. Effect of additional precursor on a CdS-HDA synthesis in progress. Bottom trace shows reaction before addition. Remainder of traces collected as temperature slowly ramped from 120°C to 174°C over the course of 90 min.

3.6 References

1. Henglein, A. *Ber. Bunsenges. Phys. Chem.* **1982**, *86*, 301-305.
2. Inoue, H.; Ichiroku, N.; Torimoto, T.; Sakata, T.; Mori, H.; Yoneyama, H. *Langmuir* **1994**, *10*, 4517-22.
3. Nanda, J.; Sapra, S.; Sarma, D. D.; Chandrasekharan, N.; Hodes, G. *Chem. Mater.* **2000**, *12*, 1018-1024.
4. Vossmeier, T.; Katsikas, L.; Giersig, M.; Popovic, I. G.; Diesner, K. Chemseddine, A.; Eichmuller, A.; Weller, H. *J. Phys. Chem.* **1994**, *31*, 7665-7673.
5. Rossetti, R.; Ellison, J. L.; Gibson, J. M.; Brus, L. *J. Chem. Phys.* **1984**, *80*, 4464.
6. See references 9 – 16 in Chapter 1 of this dissertation.

Chapter 4. Nanomaterial Characterization by MALDI-TOF Mass Spectrometry.

4.1 Introduction

We present a methodology for mass, and size dispersity analysis by MALDI-TOF mass spectrometry of lyothermally grown 2.5 – 5.5 nm CdSe nanocrystals and 2.5 –3.7 nm ZnS nanocrystals exhibiting wurtzite and zinc blende crystal structures, respectively. These results correlate with information obtained by TEM and absorption spectroscopy. The use of MS methods to probe size and size dispersity provide a convenient method to rapidly analyze II-VI materials at the nanoscale. We believe these results represent the first mass spectrometric analysis of size and size dispersities on II-VI nanocrystals.

Although the mass range needed to analyze organically passivated semiconductor nanomaterials is similar to ranges employed in the earlier applications of mass spectrometry, the isotopic contributions in II-VI materials and the mass distributions of the nanomaterial samples complicate the application of mass spectrometry techniques to these systems. The effect of size distributions on the mass spectral features for a 3.5 nm spherical ZnS particle (cubic Zn-blende structure) is easily envisioned. A 3.5 nm n-hexadecylamine (HDA) passivated nanomaterial consists of ~10 lattice planes (3.12\AA) along the [111] direction or 554 Zn-S units with ~146 HDA ligands, based on complete coverage of the surface Zn atoms.^{1a} Ignoring isotopic contributions, the nanomaterial mass would be 54,000 Da for the unpassivated ZnS core or 89,200 Da for the fully passivated particle. A

10% size distribution of the sample (3.5 ± 0.35 nm diameter) complicates the measurement resulting in a mass range for *only* the ZnS core between 35,700 and 77,600 Da. These effects would lead to a mass peak for a singly charged species on a linear time-of flight (TOF) MS instrument having a broad Gaussian peak shape without significant resolution. A MS peak for a ZnS nanocrystal in the 3.7 to 2.5 nm size range will be further broadened by 0.12 to 0.30 % of the average mass by the isotopic distributions of Zn and S, depending on size. On the other hand, the potentially high sensitivity that is achievable for the analysis of average size and size distributions experimentally by treating the FWHM of the observed Gaussian peak shape could provide a rapid and reliable analytical tool for synthetic sample analysis and quality control, a very important development in nanotechnology.

In this study we present the accurate determination of mass and mass distribution of a series of 2.5-3.7 nm ZnS nanocrystals using MALDI-TOF Mass Spectrometry. Size and size distributions are extracted from the MS data by modeling the particles as spherical Zn blende or wurtzite crystalline lattices with complete loss of surface passivation. These results correlate with the observed TEM, and optical data for the samples.

4.2 Experimental

HDA passivated CdSe (2.5-4.5 nm), CdS (2.4 – 4.9 nm), and ZnS (2.5-3.7 nm) nanocrystals were prepared using the single source precursor methodology previously described in Chapters 2 and 3.² Ligand exchange on CdSe was carried

by previously published methods.³ CdSe and CdSe/ZnS core/shell nanomaterials were prepared by the lyothermal method described by Hines, et. al.⁴

Ultraviolet and visible absorption spectra in chloroform were recorded using a Jasco 530 spectrophotometer. Transmission electron microscopy (TEM) was performed on a JEOL 1230 microscope operating at 80 kV in the bright field mode. TEM grids were 400 mesh Cu, coated with a 5 nm layer of Holey carbon, and purchased from SPI Inc. TEM samples were prepared using standard techniques. Size and size distributions were obtained by manual measurement of nanocrystal images from the digitized micrograph negatives.

MALDI-TOF MS was performed on a Micromass ToFSpec 2E instrument using dithranol or anthracene as the matrix. Nanocrystal samples were dispersed in dry chloroform, mixed with chloroform solutions of the matrix, and spotted onto a stainless steel target plate. CdSe and CdS samples with finite absorbance cross section in the desorption laser wavelength range were also analyzed in the absence of matrix. Desorption and ionization of the samples were achieved by irradiation with a pulsed nitrogen laser (337 nm, 180 μ J/pulse, 4 nsec pulses). The fixed energy laser was coupled to a stepped neutral density filter and a continuously variable iris to control the laser energy that reached the sample as a 150 x 250 μ m spot on the target plate. Nanocrystal mass spectra were measured with the laser at 50 and 100% full power. After desorption, a 20 kV potential accelerated the ions into a 1.5 m flight tube (linear TOF mode) which yielded a resolution of 100-200 m/z in the final mass spectrum. The accuracy of the measured peaks was

determined by external calibration against the ubiquitous MALDI-MS standards trypsinogen, horse heart myoglobin, cytochrome C, and bovine serum albumin.

4.3 Results

4.3.1 ZnS

The size and size dispersity of the lyothermally prepared, n-hexadecylamine passivated ZnS nanocrystals was estimated from the optical absorbance data for the samples (Figure 4.1 and Table 4.1) by comparison to previously published results.¹ A representative TEM analysis (Figure 4.2) of the 3.7 nm (3.7 ± 0.48 nm) ZnS was used to verify the size estimates from absorption spectroscopy. Materials below 3.7 nm are difficult to obtain an accurate size analysis in the TEM images due to low contrast and a propensity for ablation in the electron beam. MALDI – TOF mass spectra for the 2.5, 2.9, 3.5, and 3.7 nm diameter ZnS nanocrystals are presented in Figure 4.3a. The data for each nanocrystal sample exhibits a single high intensity, Gaussian shaped peak centered at m/z values of roughly 12000, 16000, 26500, and 37500 Da, respectively. Increased laser flux causes an increase in this feature's intensity without significantly altering the average m/z position or FWHM of the peak (Figure 4.4). The use of a less polar matrix, on the other hand, results in a shift to higher m/z at 50% laser power and lower m/z at 100% laser power (Figure 4.5).

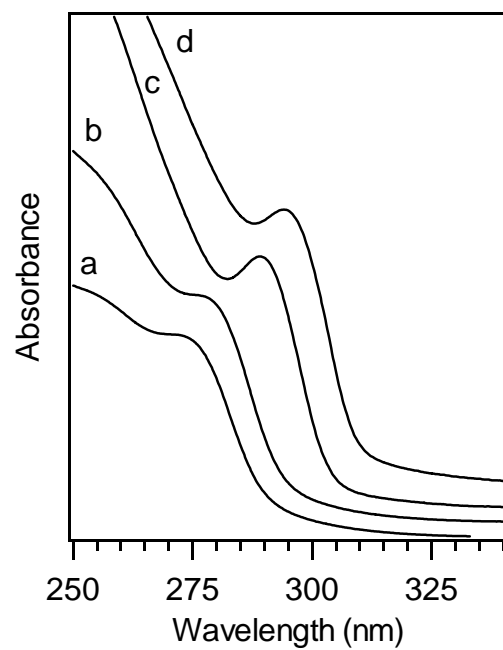


Figure 4.1. Normalized absorbance spectra in chloroform at 298 ± 2 K of batch a) 2.5, b) 2.9, c) 3.5 and d) 3.7 nm ZnS-HDA nanocrystals.

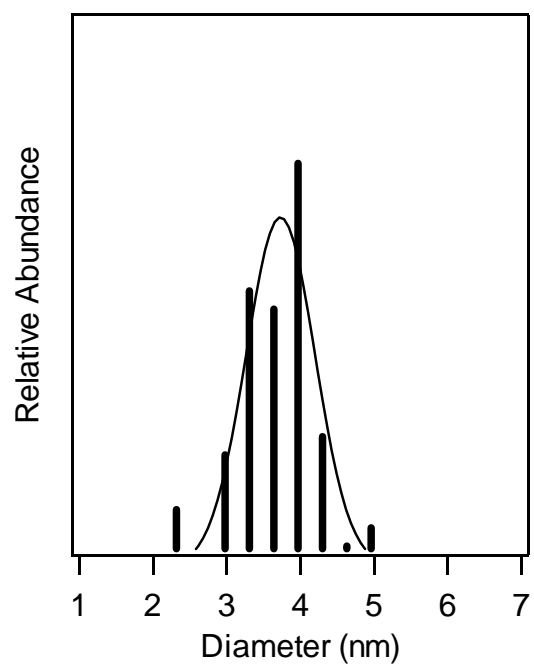


Figure 4.2. Size distribution of 3.7 ± 0.47 nm ZnS-HDA nanocrystals. Curve is a Gaussian function fit to the data. Inset shows one of the micrographs used to measure the size distribution. Scale bar is 20 nm.

Table 4.1. Statistics for ZnS nano-materials MALDI-MS characterization.

| Abs Size (nm) ^a | TEM Size dispersity ^b | MS M/Z (k amu) | MS FWHM (k amu) | Calculated Size (nm) (prolate) ^c | Calculated Size (nm) (sphere) ^c | MS Size dispersity ^d |
|----------------------------|----------------------------------|----------------|-----------------|---|--|---------------------------------|
| 2.5 | --- | 12.0 | 7.4 | 2.49 (2.99) | 2.64 | 10% |
| 2.9 | --- | 16.0 | 9.5 | 2.74 (3.29) | 2.91 | 10% |
| 3.5 | --- | 26.5 | 20.0 | 3.25 (3.90) | 3.45 | 13% |
| 3.7 | 13 % | 37.5 | 29.8 | 3.65 (4.37) | 3.87 | 13% |

^aSize estimated from the position of the absorbance exciton by comparison to previously reported TEM measurements.

^bMeasured from TEM measurements in this work.

^cCalculated from MS peak m/z using the appropriate model.

^dCalculated from MS peak FWHM using the spherical model.

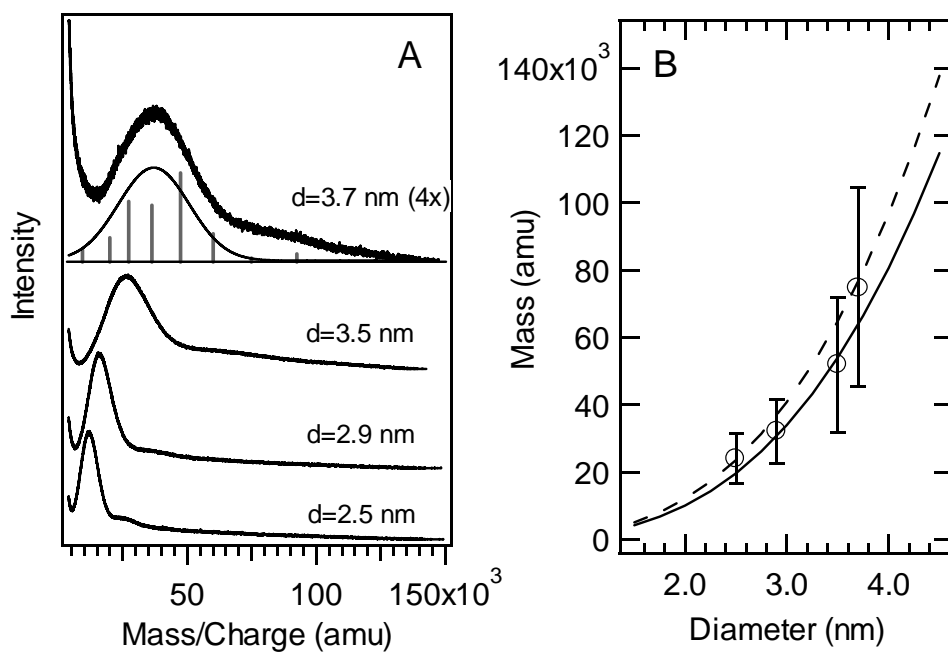


Figure 4.3. (A) MALDI-MS spectra of 2.5, 2.9, 3.5 and 3.7 nm ZnS-HDA nanocrystals using dithranol as the matrix. The mass distribution for 3.7 nm materials was extrapolated from the size distribution data presented in figure 3. (B) Nanocrystal masses projected from MS data assuming +2 species vs. masses calculated by assuming spherical (solid line) and prolate (dashed line) nanocrystal morphologies.

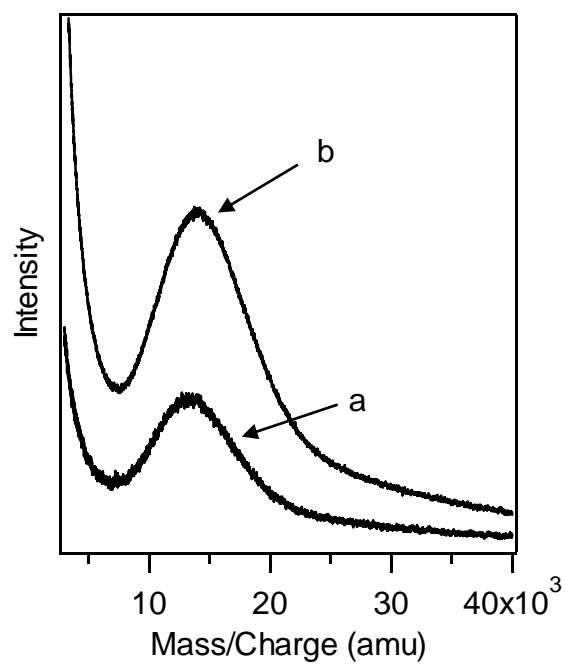


Figure 4.4. MALDI-MS spectra of 2.5 nm ZnS-HDA nanocrystals using dithranol as the matrix and a) 50% and b) 100% laser power.

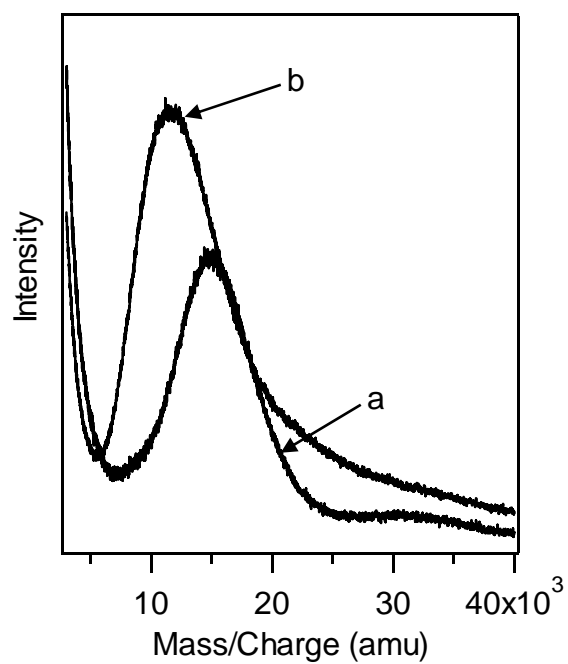


Figure 4.5. MALDI-MS spectra of 2.5 nm ZnS-HDA nanocrystals using anthracene as matrix, and a) 50% and b) 100% laser power.

4.3.2 CdSe

The average sizes and size dispersities of the CdSe-HDA materials were estimated from optical absorbance data (Figure 4.6) by comparison to previously published results³, and verified by TEM measurements presented in Figure 4.7. MALDI-TOF mass spectra for the 2.5, 3.2, 4.0, 4.9, and 5.5 nm diameter nanocrystals appear in figure 4.8. The spectrum for each sample exhibits an intense feature that corresponds to a nanocrystal bearing a single positive charge and lower intensity features that were assigned to +1, +2, +3, +4, and +5 charged nanocrystals as well as nanocrystal dimers and trimers. Similar features were also observed in the mass spectra of TOPO capped CdSe and CdSe/ZnS core/shell nanomaterials (Figure 4.9). The values of average size and size distribution calculated from the m/z value and FWHM of the MS features were found to be in good agreement with the values obtained from optical and TEM measurements (Table 4.2).

Increasing the concentration of CdSe-HDA nanocrystals in the analyte mixture results in a shift of the most intense feature to lower m/z with the largest shift observed when no matrix was used at all (Figure 4.10). Higher nanomaterial concentrations also resulted in increased intensity of mass spectral features assigned to multiply charged species and nanocrystal multimers. Increasing the laser flux without altering the [CdSe] resulted in an increase in peak intensity with negligible change in m/z ; the same as for ZnS nanomaterials (Figure 4.11). The higher stability of CdSe nanomaterials relative to ZnS with respect to ligand exchange also allowed the investigation of surface ligand effects on the outcome of MALDI-MS

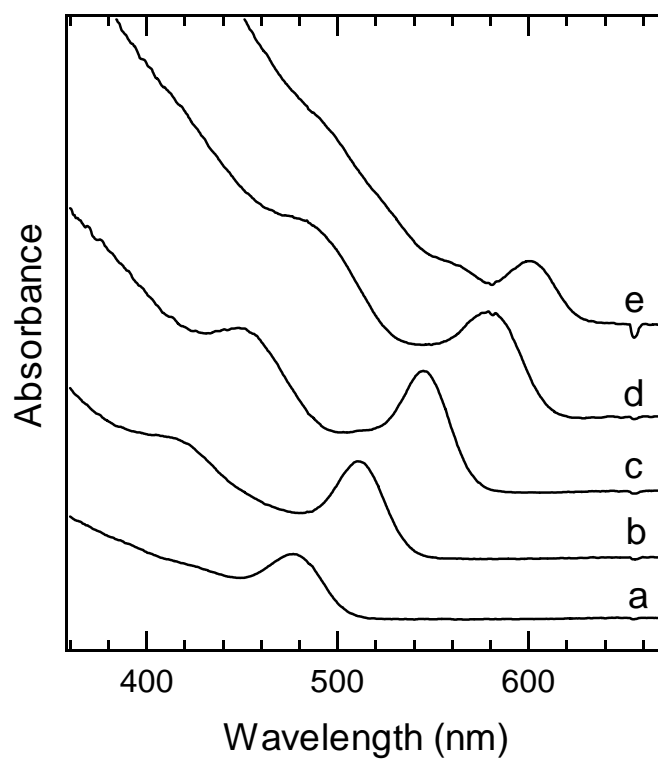


Figure 4.6. Absorbance spectra of (a) 2.5, (b) 3.2, (c) 4.0, (d) 4.9, and (e) 5.5 nm diameter CdSe-HDA. Spectra collected in chloroform under ambient conditions.

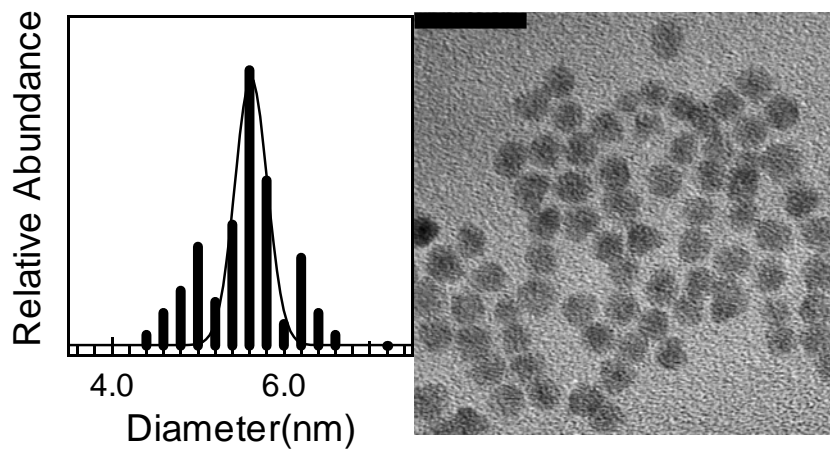


Figure 4.7. TEM Size distribution of 5.6 ± 0.3 nm CdSe-HDA nanocrystals. Curve is a Gaussian function fit to the data. Inset shows one of the micrographs used to measure the size distribution. Scale bar is 20 nm.

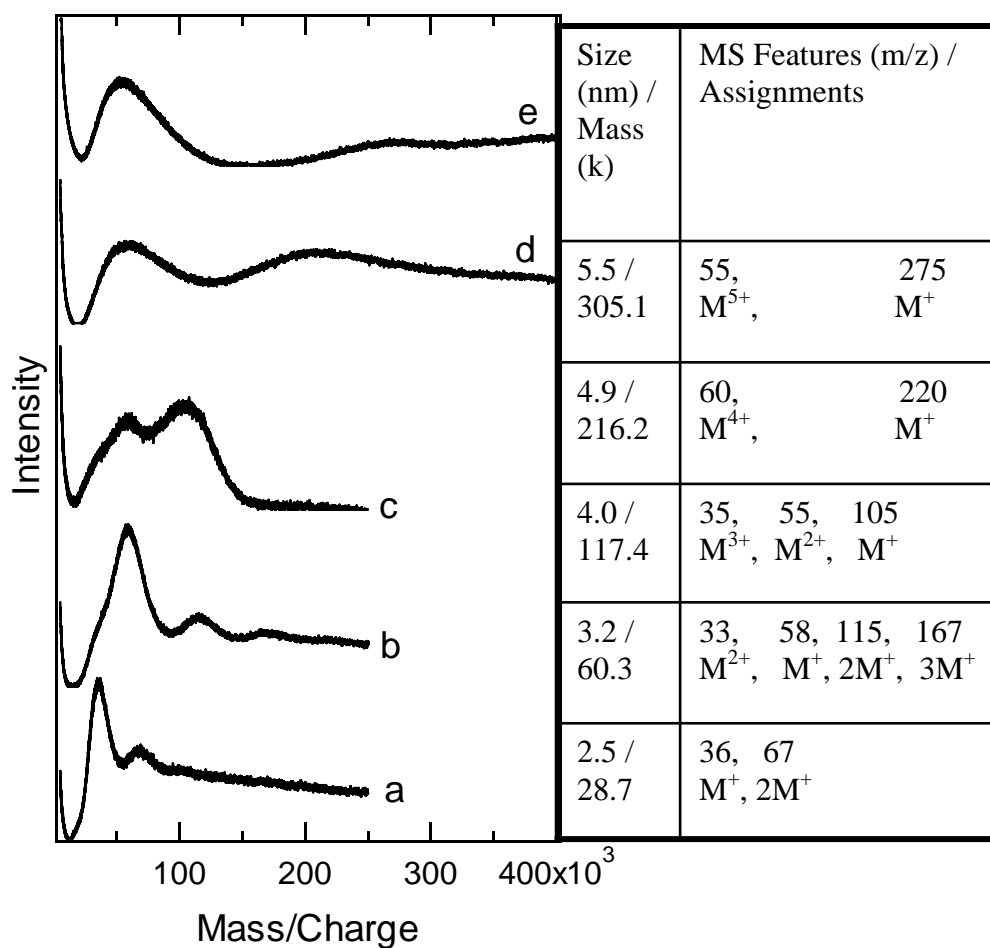


Figure 4.8. Assignment of CdSe MALDI-TOF mass spectra of (a) 2.5, (b) 3.2, (c) 4.0, (d) 4.9, and (e) 5.5 nm CdSe-HDA nanocrystals collected using dithranol and threshold laser power. Calculated mass assumes a singly charged spherical nanocrystal with no surface

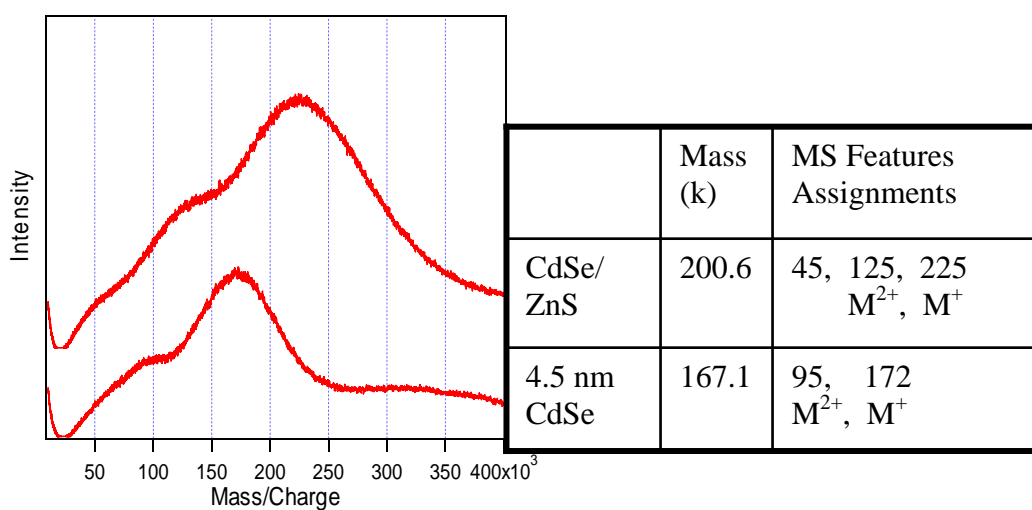


Figure 4.9. Assignment of MALDI-TOF mass spectra of 4.5 nm CdSe nanocrystals passivated with (a) TOP/TOPO, and (b) ZnSe. Calculated mass assumes a singly charged spherical nanocrystal with no organic surface passivation.

Table 4.2. Statistics for CdSe-HDA and CdSe-TOPO nanomaterials MALDI-MS Characterization.

| Size ^a (nm) | Size Dist ^a (%) | Size ^b (nm) | Size Dist ^b (%) | NC Mass ^c (k) | MS Size ^d (nm) | MS Size Dist (%) |
|---------------------------|----------------------------------|---------------------------|----------------------------------|-----------------------------|---------------------------------|------------------------|
| 2.5 | 6 | --- | --- | 36 ± 8.9 | 2.69±0.23 | 8.6 |
| 3.2 | 6 | --- | --- | 58 ± 17.9 | 3.16±0.33 | 10.4 |
| 4.0 | 5 | --- | --- | 105 ± 24.7 | 3.85±0.30 | 7.8 |
| 4.9 | 7 | --- | --- | 220 ± 46 | 4.93±0.37 | 7.5 |
| 5.5 | 5 | 5.6±0.35 | 6 | 270 ± 53 | 5.30±0.37 | 7.0 |
| 4.5 | 5 | 4.5±0.23 | 5 | 167 ± 50 | 4.50 ± 0.45 | 10.0 |
| Core- shell | -- | 4.9±0.25 | 5 | 225 ± 83 | 5.12 ± 0.63 | 12.3 |

^aEstimated from position of absorbance exciton.

^bTEM measurements in this work.

^cMALDI-MS measurements in this work.

^dCalculated from MS peak m/z assuming spherical nanocrystals.

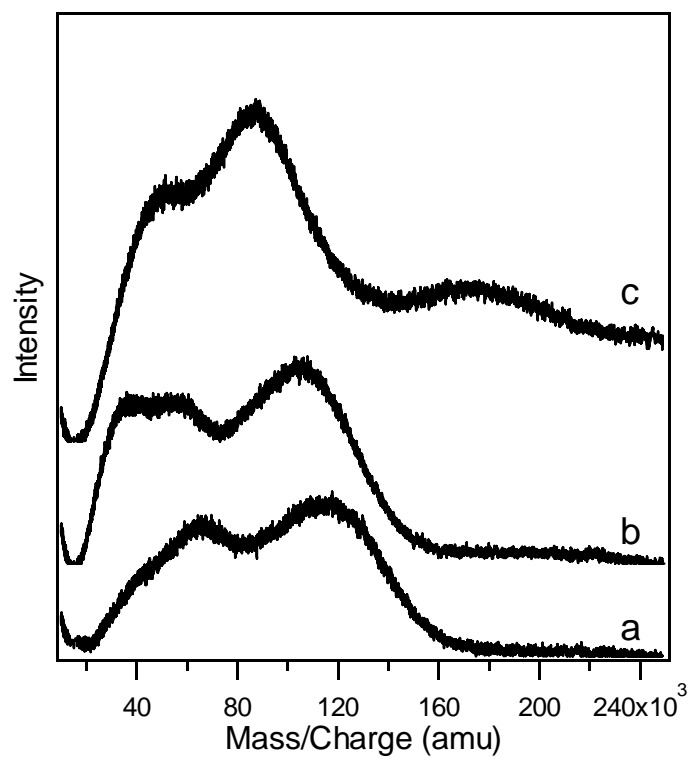


Figure 4.10. MALDI-TOF mass spectra of 4.0 nm CdSe-HDA. Concentration of the nanocrystals in the deposition solution was (a) 0.2, (b) 0.5, and (c) 2.0 mg/ml. The 2.0 mg/mL sample contained no matrix.

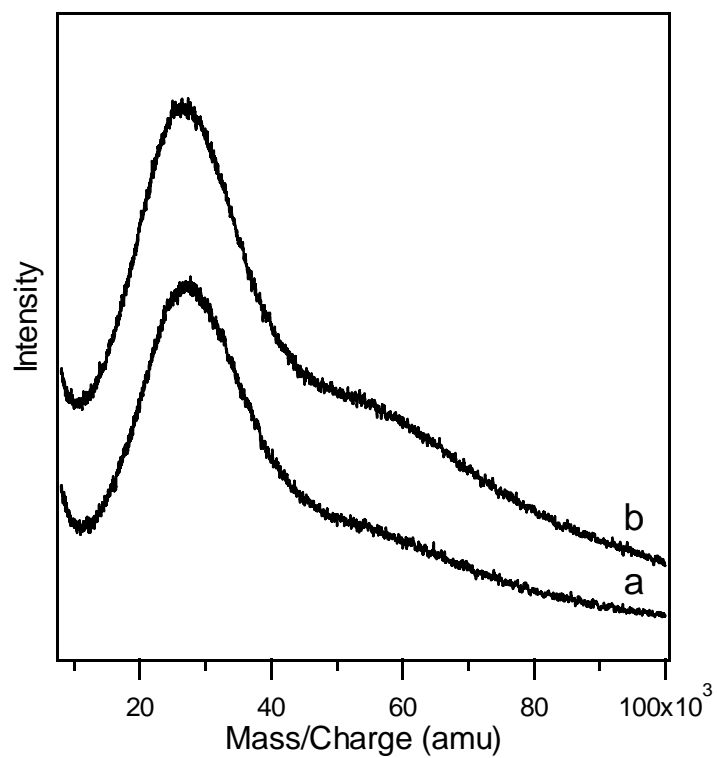


Figure 4.11. MALDI-MS spectra of 2.5 nm CdSe-HDA. Desorption/ionization laser intensity was (a) threshold and (b) 2x threshold. The CdSe concentration was 0.5 mg/ml.

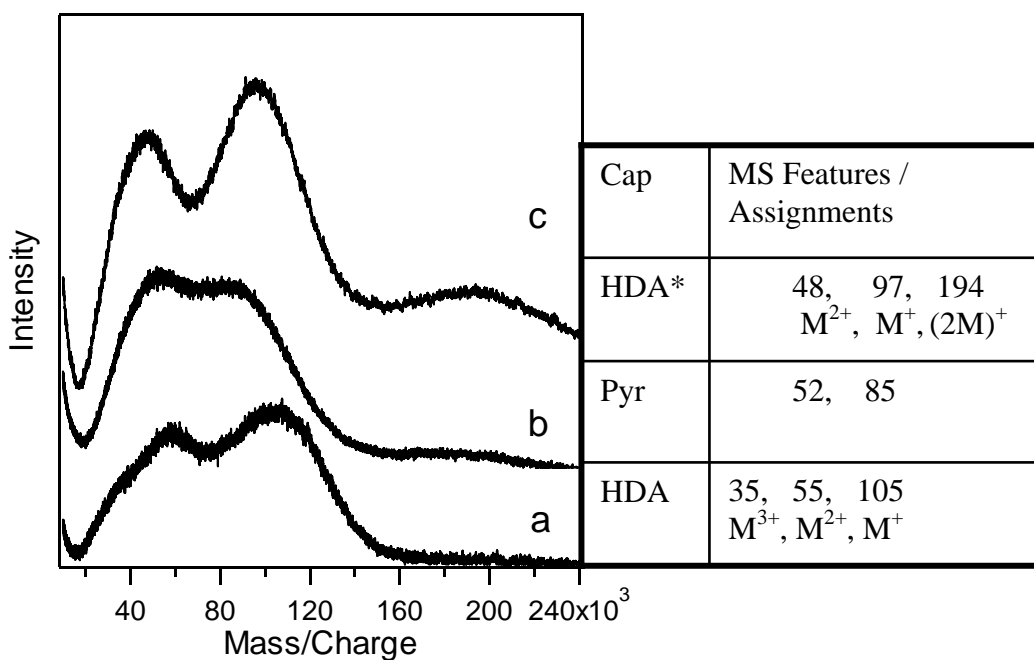


Figure 4.12a. Assignment of MALDI-TOF mass spectra of 4.0 nm CdSe nanocrystals (Calculated mass = 117.4 k) passivated with (a) HDA, (b) Pyridine, and (c) recapped with HDA. Spectra were collected using threshold laser energy. Calculated mass assumes a singly charged spherical nanocrystal with no surface passivation

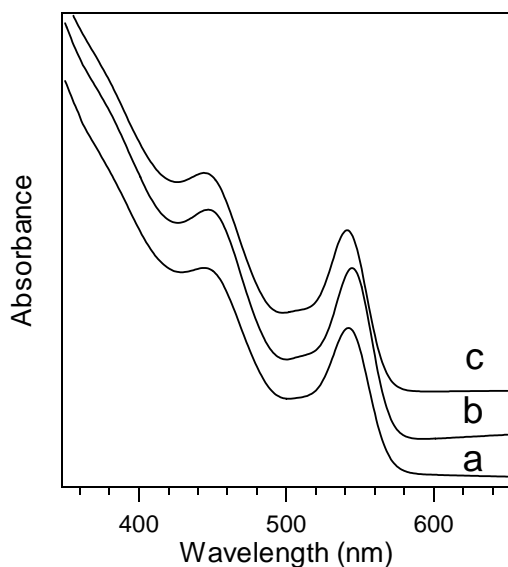


Figure 4.12b. Absorbance spectra of 4.0 nm CdSe nanocrystals passivated with (a) HDA, (b) Pyridine, and (c) recapped with HDA. Spectra were collected in chloroform under ambient conditions.

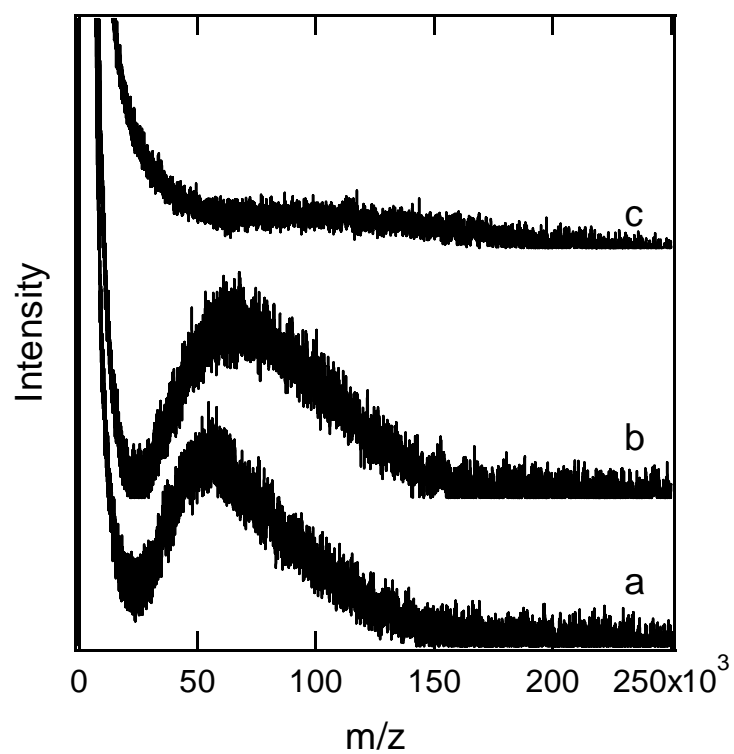


Figure 4.13. MALDI-TOF of 4.0 nm CdSe-Pyridine. Concentration of nanomaterials in the deposition solution is (a) 0.2, (b) 0.5, and (c) 2.0 mg/mL. The 2 mg/mL sample contained no matrix.

characterization. It was found that recapping HDA passivated nanomaterials with lighter pyridine ligands resulted in a shift of the primary peak to lower m/z ; while a shift to higher m/z was recorded following the restoration of the HDA capping layer (Figures 4.12a and 4.12b). It was also discovered that CdSe-Pyridine nanomaterials are more sensitive to laser induced degradation than their HDA capped counterparts (Figure 4.13) with the signal for the Pyridine capped materials disappearing at higher NC concentrations. Passivating the NCs with hexadecane thiol, on the other hand, resulted in better stability than the amines with an increase in intensity and shift to higher m/z at higher concentrations of nanomaterials in the analytical sample (Figure 4.14).

4.4 Discussion.

4.4.1 ZnS

As predicted for an increase in mass with increasing nanocrystal size, the peak shifts to higher m/z values for samples containing larger nanocrystals. Coupled to the shift, a broadening of the Gaussian peak shape is also observed due to an increase in mass distribution for larger nanocrystals with a fixed size dispersity, i.e a 10 nm diameter ZnS nanocrystal sample will have a mass distribution roughly eight times larger than a 5 nm sample if both samples exhibit a 10% size distribution. A smaller feature, centered at approximately two times the m/z value of the high intensity peak, is also observed in the spectra for each

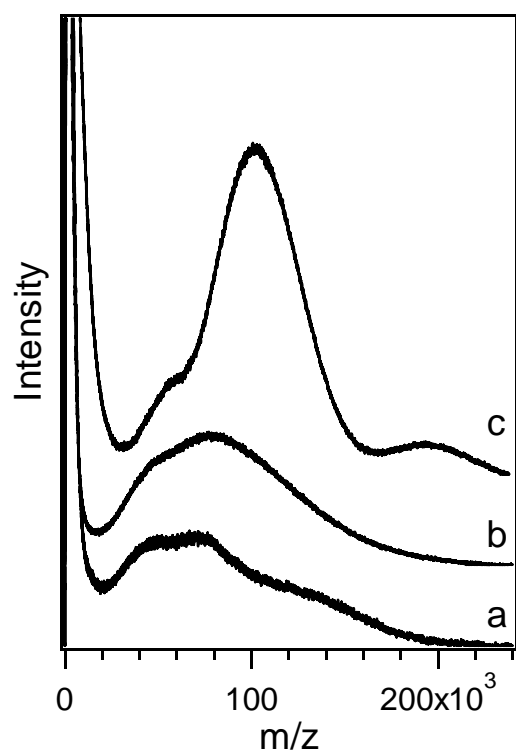


Figure 4.14. MALDI-MS of 4.0 nm CdSe nanocrystals passivated with Hexadecane thiol. Nanomaterial concentrations were (a) 0.2, (b) 0.5, and (c) 2.0 mg/mL in the sample deposition mixture.

nanomaterial. Because of the low signal to noise ratio of this feature values for the center and FWHM of the peak could not be assigned. In order to relate the observed mass spectral features to the particle size, the charge (z) for the ZnS samples must be known. The charge cannot be directly assigned from the experimental data due to the low resolution of the instrument in the linear mode. However, assuming that the structural motif for the materials is Zn blende, and that the nanocrystals exhibit a roughly spherical (or prolate) morphology, the mass and m/z ratio for the materials can be calculated using equation (1).

$$(\text{ZnS})_n = \pi/2 N_A (d^3)/(3V_m) \quad (1)$$

The quantity $(\text{ZnS})_n$ in equation (1) is the number of repeating ZnS units in the nanocrystal, N_A is Avogadro's number, d is the nanocrystal diameter obtained from absorbance or TEM measurements, and V_m is the molar volume of bulk ZnS. A value of $2.38 \times 10^{22} \text{ nm}^3/\text{mol}$ was used for V_m and was calculated from the density of bulk ZnS having the Zn blende crystal structure.⁶ To calculate the mass of a prolate nanocrystal, the d^3 term was multiplied by 1.2 to correct for the elongated axis in a prolate nanocrystal, which represents the maximum nanocrystal diameter ratio observed in the TEM studies of the 3.7 nm nanomaterial sample. Comparison of the calculated mass with the m/z value of the mass spectral feature allows the charges to be assigned.

Comparison of the MS data and calculated masses in Table 4.1 and Figure 4.3a, indicates the m/z position of the peak for each nanomaterial corresponds to roughly one half the calculated mass of either a spherical or prolate nanocrystal core

(Figure 4.3b) with the organic passivating ligands removed. The relatively small mass difference between spherical and prolate materials, and the difficulty in assigning exact morphology in the TEM do not allow the structural motif to be unequivocally assigned. The most probable assignment of this peak is, therefore, a doubly charged nanocrystal species with a nearly spherical motif and most or all passivating ligands removed. Surprisingly, the MS results produce sizes that correlate closely to the values estimated from the position of the absorbance exciton (Table 4.1) and are within the size distribution limits measured by TEM. This is further verified by direct comparison of the calculated mass distribution for a spherical, 3.7 nm diameter particle to the experimental mass measured by the MALDI-TOF technique (Figure 4.3a). The lower intensity feature at roughly two times the m/z value of the intense peak could arise from small amounts of singly charged nanocrystals or to nanocrystal aggregates. Such aggregates were previously observed in LDI studies of Au nanocrystals.⁷

The observation of doubly charged ions is not surprising; multiply charged ions are often observed in MALDI-MS measurements of high molecular weight polymers.⁸ It is unusual to only observe a double charged species in such a large system. In the mass spectrum of a polymer or biological molecule in the size range of the nanocrystal a significant presence of singly and possibly triply charged species is normally also observed. In fact MALDI-MS studies on CdSe nanomaterials result in a series of peaks that are assignable to singly, doubly, and triply charged nanocrystals species. The apparent anomalous behavior in ZnS may

be attributable to the higher ionic character of the ZnS lattice compared to CdSe, which allows the former to consistently retain more charges. It is also possible that the observation of doubly charged ZnS fragments in the MS data may be associated with the lack of direct laser absorption, while the significant absorption cross section of CdSe at 337 nm leads to the production of higher charged species in the MS data.

The possibility that the high intensity MS peak could arise from a singly charged fragment species due to laser induced ablation was investigated by observing the effects of increased laser power on the spectral features (Figure 4.4). The lack of a significant change in the peak position or shape suggests that laser ablation does not result in fragmentation of the parent ion. The lack of an m/z shift further suggests that ZnS nanomaterials are ionized without the ligand shell, which is consistent with the observation of a good correlation between the calculated and measured nanocrystal masses. The capping material is most likely lost in the laser plume, as was previously observed for Au nanocrystal measurements by LDI-TOF MS.⁷ Selective ligand ablation is particularly likely for our materials because the hexadecylamine ligand has a finite absorption cross section at 337 nm while the ZnS core does not, and the lattices of ZnS nanocrystals are more ionic in nature, which would tend to weaken the interaction of the passivating layer. This assumption is supported by previously reported ligand exchange dynamics in II-VI nanocrystals.³

The effect of changing the matrix on the observed MALDI spectra provides additional evidence for ligand loss from the ZnS nanoparticles. Comparison of the

MS data for 2.5 nm ZnS collected in anthracene (Figure 4.5) shows that the high intensity peak in anthracene is shifted relative to the dithranol for data collected at 50 and 100% laser power. This shift could be the result of a higher affinity of the less polar anthracene for the hydrophobic tails of the HDA capping groups on the nanocrystals. At the lower laser power more matrix molecules remain associated with the desorbed nanocrystal species giving rise to a larger m/z value. At the higher laser power, the closer association of the matrix and ligand results in a more efficient energy transfer leading to a more efficient removal of ligands from the surface of the nanocrystals and ablating a small amount of core material.

Assignment of the observed m/z peak as a doubly charged species without a layer of passivating ligands allows the m/z value, and therefore the size, of the nanomaterial to be discretely assigned (Table 4.1). The assumption that the average mass arises primarily from un-passivated ZnS materials allows the mass peak linewidth to be analyzed as a direct measure of the size dispersity of the nanocrystals, as long as isotope contributions and instrumental resolution are included in the calculation. This is achieved by considering the number of ZnS mass units that correspond to a measured mass in the MALDI data, and converting the FWHM for the Gaussian mass profile for each material. For example, in the 3.7 nm ZnS nanocrystals, the size distribution based on TEM imaging is $\pm 13\%$ or 0.48 nm (Figure 4.2). This size distribution corresponds to a mass distribution in the 3.7 nm ZnS sample of ± 24.5 kDa or 38% for a spherical nanocrystals (Table 4.1). Isotope contributions to the mass increase the FWHM by 0.1% of the observed linewidth

(85 Da for the 3.7 nm ZnS material), and the instrument resolution is expected to contribute another 2% of the m/z value to the FWHM or 750 Da. The combined contributions of the above factors predict a $\pm 40\%$ mass distribution on the MALDI experiment for a 3.7 nm ZnS sample which agrees well with the observed FWHM for the MS peak of ± 40 mass %. Further proof of the validity of this approximation can be seen by inspection of the theoretical mass distribution fit of the 3.7 nm MS data shown in Figure 4.3b, which exhibits a quantitative agreement with the TEM and MS results. Using the same strategy the size distributions for the other samples can be directly calculated for a spherical morphology (Table 4.1). By inspection of Table 4.1, the ZnS materials can be systematically correlated with their absolute size and size dispersity and are in full agreement with the optical and TEM results suggesting that MS could be a powerful tool for rapid sample analysis of II-VI nanomaterials.

4.4.2 CdSe

The MALDI mass spectra of 2.5, 3.2, 4.0, 4.9, and 5.5 nm diameter CdSe-HDA using dithranol as a matrix are shown in Figure 4.8. The spectrum for each sample features a peak with an m/z value that corresponds to an unpassivated nanocrystal bearing a single positive charge (M^+). This feature occurs at 36, 58, 105, 220, and 275 k, respectively. The theoretical mass of an unpassivated nanocrystal was calculated by assuming a spherical core having a wurtzite crystal structure based on the measurements reported in Chapter 2 of this thesis. The

relative intensity of the M^+ peak was observed to progressively decrease for larger nanomaterials probably as a result of the lower desorption efficiency of larger HDA capped species. The desorption efficiency appears to depend on the nature of the nanomaterial passivating ligand. As is shown in Figure 4.9, the M^+ peak is the most intense feature in the spectrum of tri-n-octylphosphine oxide (TOPO) passivated materials having 4.5 and 4.9 nm diameter cores.

As was observed for the ZnS nanomaterials, discussed earlier, the CdSe-HDA and CdSe-TOPO nanocrystals exhibit a good correlation between the average size and size distribution values obtained from traditional (absorbance, TEM) and MS methods (Table 4.2). The CdSe nanomaterial size distribution values calculated from the measured mass distribution are smaller than that observed for ZnS nanomaterials (Table 4.2). This is consistent with the trend in the FWHM of the absorbance peak of the materials (Figures 4.1 and 4.6). The size distribution values also vary consistently with the FWHM values of the absorbance spectra. The correlation between the FWHM and size distribution has been previously established.³

In addition to the M^+ feature, the mass spectra also exhibit intense peaks that were assigned to singly charged nanocrystal aggregates $((nM)^+)$ and multiply charged single nanocrystal species (M^{n+}) . The phenomenon of nanocrystal aggregation is well known in solution based nanomaterial assembly⁹ and probably occurs as the solvent evaporates during the sample deposition onto the target plate. Figure 4.8 shows more prominent $(nM)^+$ cluster peaks in the MS of 2.5 and 3.2 nm

materials because these samples have larger numbers of nanocrystals for a given concentration of CdSe than larger sizes. Spectral features assigned to $(2M)^+$ species, however, are observed for 4.0 nm particle at higher CdSe concentrations in the analyte sample (Figure 4.10) and are consistent with increased NC-NC interactions.

The MS features at m/z values lower than those of the NC^+ feature in figure 4.8 may be the result of either nanocrystal fragmentation in the laser plume or the formation of multiply charged single nanocrystals. The consistent location of the peaks at roughly even fractions of the nanocrystal mass (one half the m/z value for the 3.2 nm CdSe materials; one half and one third of the value for the 4.0 nm materials, etc.) suggests that these peaks are the result of +2, +3, +4, and +5 charged nanocrystals. The presence of higher charged nanocrystals in the CdSe spectra could be the result of photoionization by the laser which was not observed in ZnS materials because the latter do not absorb at 337 nm. The presence of higher charges on larger nanomaterials is also consistent with the increasing ability of a larger inorganic core to accommodate more charge. The possibility that the lower m/z peaks are due to fragmentation of the nanomaterials is unlikely. As can be seen in Figure 4.10, the laser induced degradation of CdSe-HDA nanomaterials takes the form of a gradual shift of the M^+ peak to lower m/z values, not the disappearance of the M^+ peak to form features at fractional m/z values. Quite predictably, this analyte degradation was successfully prevented by the use of matrix even at elevated laser intensities. As is shown in Figure 4.11, doubling the laser power has

no measurable effect on the peak position of 2.5 nm CdSe-HDA provided the sample is analyzed in a dithranol matrix.

One of the assumptions made in the analysis of the ZnS-HDA and CdSe-HDA MALDI data was that the organic capping ligands are either mostly or completely removed during the desorption / ionization process. The good correlation of the average size and size distribution measurements obtained from MS with those obtained from optical and TEM data substantiates this assumption. In an effort to test exactly what happens to the coordinating ligands, the HDA ligands of a 4 nm core were exchanged for the lighter and weaker binding pyridine ligands prior to MALDI-MS analysis. This exchange did not significantly affect the size of the nanomaterials as measured by absorption spectroscopy (Figure 4.12b), however, the M^+ MS feature shifted from m/z 105,000 to 85,000 after the ligand exchange. The feature returned to a higher m/z values when the pyridine ligands were replaced with HDA, indicating that the shift is the result of ligand exchange. This shift is most likely the result of increased nanomaterial degradation by the laser flux. The smaller, pyridine ligands allow the laser absorbing matrix molecules to come closer to the nanocrystal core and require less energy to remove than HDA ligands resulting in increased ablation of the core. This is evident in the degradation of pyridine capped CdSe at higher analyte concentrations (Figure 4.13). The same effect was observed when CdSe-HDA was analyzed in the absence of matrix analysis and when the anthracene matrix that interacted more strongly with the hydrophobic tails of the capping ligands was employed in ZnS-HDA analysis.

Another possible explanation of the M^+ feature shift with recapping is that it is the result of the replacement of 123 HDA ligands by pyridine; the mass difference between 123 HDA and pyridine ligands being 20,000 mass units. One could argue, therefore, that the most intense feature does not correspond to a bare inorganic core, but to a core with at least 123 ligands attached to it (in the case of this 4 nm CdSe). This physical picture is inconsistent with the absorbance data. The presence of 123 HDA capping ligands would have a mass of roughly 29.6 k amu. This would mean that the mass of the core was only 75 k amu which would correspond to a core diameter of 3.4 nm, while the absorbance spectrum (Figure 4.12b) clearly indicates a 4 nm core.

MALDI-MS analysis of CdSe nanomaterials recapped with hexadecanethiol (HDT) produces several unexpected results. As can be seen in Figure 4.14, the M^+ peak appears at m/z 72, 77, and 102 k at CdSe concentrations of 0.2, 0.5, and 2.0 mg/mL, all of which are lower than the values observed for CdSe-HDA nanomaterials at the same concentrations (Figure 4.10). This decrease in the m/z value of M^+ would be expected as a result of degradation with a weaker binding ligand (i.e. pyridine), or as a result of mass loss with a lower molecular weight ligand. HDT, on the other hand, is known to bind more strongly to CdSe than amines and has a molecular weight greater than that of HDA.

Furthermore, the CdSe-HDT peak assigned to the M^+ species is observed to gradually shift to higher m/z values with increasing CdSe concentration (Figure 4.14). While it is expected that the thiol head group is less likely to be removed

from the nanocrystal surface than the amine ligands, this apparent increase in analyte mass is puzzling. The only explanation for the apparent increase in mass is the selective desorption of larger nanomaterial fractions in the analyte mixture.

4.4 Conclusion

Our results show that it is possible to carry out MALDI-MS on inorganic nanomaterials. These studies allow the extrapolation of the MALDI-MS data to the analysis of size measurement and size distributions based on experimentally measured mass data. Both the observed peak position and peak width are consistent with the hexadecylamine capped ZnS or CdSe nanocrystal system being studied.

Studies with CdSe nanomaterials show that this technique can be extended to inorganic materials which absorb the incident laser radiation. Degradation is minimal if the material is mixed with a sufficient amount of matrix before analysis. Further refinements of this technique such as matrix optimization, variation of FWHM with size distribution, as well as applications to other II-VI nanomaterials are currently in progress.

This sensitivity of the nanomaterial analysis to the surface passivating ligands echoes one of the drawbacks of the HPLC method developed for fast and accurate average size and size distribution determination in nanocrystal samples. It was found that the size exclusion column, which was used to separate the nanocrystals based on their speed of migration through the column, would interact

more strongly with certain passivation ligands, and this interaction would affect the migration time, and therefore, the reported size of the nanocrystal sample. It thus appears that a successful technique (spectroscopy, TEM) for rapid and accurate size quantification of inorganic nanomaterials must be insensitive to the effects of the passivation ligands.

4.5 References

1. (a) Inoue, H.; Ichiroku, N.; Torimoto, T.; Sakata, T.; Mori, H.; Yoneyama, H. *Langmuir* **1994**, *10*, 4517-22. (b) Nanda, J.; Sapra, S.; Sarma, D. D.; Chandrasekharan, N.; Hodes, G. *Chem. Mater.* **2000**, *12*, 1018-1024.
2. Cumberland, S. L.; Hanif, K. M.; Javier, J.; Khitrov, G. A.; Strouse, G. F.; Woessner, S. M.; Yun, C. S. *Chem. Mater.* **2002**, *14*, 1576-1584.
3. Murray, C. B.; Norris, D. J.; Bawendi, M. G. *J. Am. Chem. Soc.* **1993**, *115*, 8706.
4. Hines, M. A.; Guyot-Sionnest, P. *J. Phys. Chem.* **1996**, *100*, 468-471.
Nanomaterials synthesized and isolated by Mr. Travis Jennings.
5. Instrument lease courtesy of the Waters Corporation.
6. CRC Handbook of Chemistry and Physics, 59th ed.; Weast, R. C. Ed.; CRC Press, Inc. Boca Raton, FL.
7. (a) Whetten, R. L.; Khoury, J. T.; Alvarez, M. A.; Murthy, S.; Vezmar, I.; Wang, Z. L.; Stephens, P. W.; Cleveland, C. L.; Luedtke, W. D.; Landman,

- U. *Adv. Mater.* **1996**, 8, 428-433. (b) Arnold, R. J.; Reilly, J. P.; *J. Am. Chem. Soc.* **1998**, 120, 1528-1532.
8. Belu, A. M.; DeSimone, J. M.; Linton, R. W.; Lange, G. W.; Friedman, R. M. *J. Am. Soc. Mass. Spec.* **1996**, 7, 11-24.
9. Murray, C. B.; Kagan, C. R.; Bawendi, M. G. *Ann. Rev. Mater. Sci.* **2000**, 30, 545-610.

Chapter 5. Characterization of $\text{Ti}_6\text{O}_4(\text{O}_2\text{C}_4\text{H}_5)_8(\text{OCH}_2\text{CH}_3)_8$ by electrospray time of flight Mass Spectrometry.

5.1 Introduction.

Application of ESMS techniques to inorganic molecular clusters has been a growing area of interest for studying the molecular to bulk transition in materials.¹ A titanium oxide molecular cluster prepared by hydrolysis of titanium tetraethoxide in the presence of methacrylic acid, can be characterized by electrospray time of flight mass spectrometry (ESMS-TOF). The chemistry of such systems is not well known and ESMS is a powerful technique for studying the reactions of clusters in solution. The fingerprint pattern of the cluster fragmentation suggests formation of Ti_xO_y core fragments that represent commonly observed structural constructs in bulk titanium oxide metallates. The fragmentation steps provide insight into the hydrolytic conversion of this molecular sol gel intermediate into bulk TiO_2 . While MS has been applied to the study of metal alkoxide hydrolysis mechanisms, mass spectra of isolated individual titanium oxide clusters have not previously been reported.

Furthermore, analysis of the cluster in coordinating and non coordinating solvents suggests that the effects of coordinating solvent can be successfully studied by changing the energy of the ESI source. This further expands the utility of ESMS as an investigative tool in inorganic cluster and materials chemistry.

5.2 Experimental

[Ti₆O₄(EtO)₈(McO)₈] clusters were synthesized as reported elsewhere² and kindly provided by Prof. Ulrich Schubert. The clusters were stored in a nitrogen filled drybox to minimize hydrolysis. The clusters were dissolved in dry toluene (Fisher) to yield a 3 mM solution to which 200 proof ethanol (Fisher) was added to 17 volume %. Acetone (Fisher) was added to 50 volume % for non-coordinating solvent studies. The mass analysis was performed on a Micromass QTOF2 mass spectrometer equipped with Quadrupole and time of flight (TOF) analyzers, as well as a hexapole collision cell. The sample solution was introduced by a Harvard syringe pump coupled to an infusion electrospray source. Block and desolvation temperatures were set to 120 and 150°C, respectively. Cone voltage was varied between +30 and +100 V. Nitrogen was used as the nebulizing and desolvation gas, while Argon was used as the collision gas. All gases were purchased from Air Liquide and were UHP grade. MS/MS was performed by setting the quadrupole analyzer to only pass ions of a specific m/z value, subjecting the ion to high energy collisions with Argon atoms in the collision cell, and using the TOF analyzer to study the products of degradation as the collision voltage was increased. Collision voltage was varied between +10 and +80 V depending on the ion being analyzed. At least 100 scans were averaged, and smoothed for each mass spectrum presented. All peaks with a relative intensity of 3% of the maximum or higher were assigned to molecular species. All assigned peaks in the presented mass spectra were identified by the most abundant isotope (⁴⁸Ti, 73.8% abundance). Mass analysis and isotope

modeling were performed on software provided by Micromass Inc. The instrument was externally calibrated with a standard mixture of NaI and CsI.

5.3 Results

Figure 5.1 presents the positive ion mass spectrum of the $[\text{Ti}_6\text{O}_4(\text{EtO})_8(\text{McO})_8]$ parent cluster dissolved in dry toluene containing 17 % ethanol by volume, collected with cone voltage settings of +30, +50 and +100 V. The significant observed mass peaks, their relative intensities, and the chemical species to which they were assigned appear in Table 5.1. The chemical species observed in the mass spectra were assigned to fragments of the original cluster core. The fragments can be grouped into nine families denoted by the letters (A) through (I). The fragmentation mechanism of the cluster is presented as a flowchart in Figure 5.2 with the schematic drawings of probable core structures of the nine cluster families shown in Figure 5.3. The structures adequately account for both the core atoms and the organic ligands in the assigned formulae of the MS species. Assignment of MS peaks was aided by MS/MS experiments, with representative MS/MS data is shown in Figures 5.4 and 5.5. Some of the species were assigned to water addition in the collision cell of the instrument (Figure 5.6).

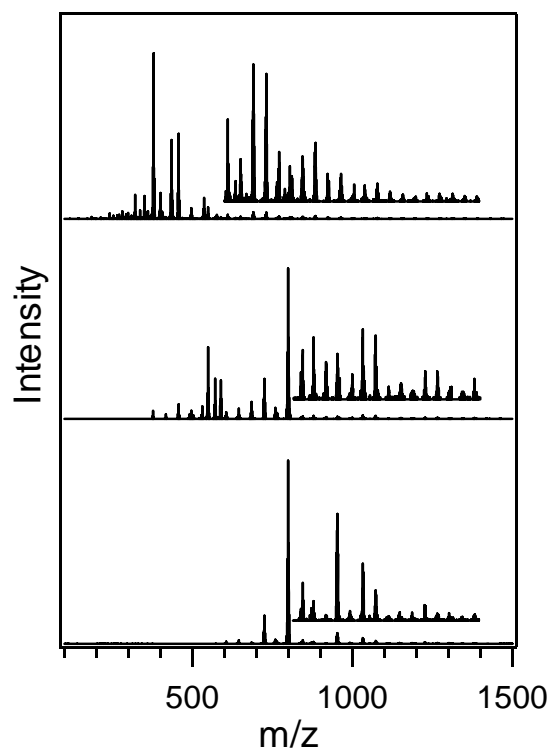


Figure 5.1. Electrospray mass spectra of $\text{Ti}_6\text{O}_4(\text{EtO})_8(\text{McO})_8$ in toluene - ethanol using cone voltage settings: (a) +30, (b) +50, and (c) +100 V.

Table 5.1. MS peak assignments for $[\text{Ti}_6\text{O}_4(\text{EtO})_8(\text{McO})_8]$ fragments in coordinating solvent.

| Core | Peak Assignment | Normalized Peak Intensity | | | Expt. m/z | Calc. m/z |
|------|---|---------------------------|-----|------|-----------|-----------|
| | | 30V | 50V | 100V | | |
| | | | | | | |
| A | $[\text{Ti}_5\text{O}_3(\text{EtO})_9(\text{McO})_4]^+$ | 3 | --- | --- | 1033.0 | 1033.20 |
| | $[\text{Ti}_5\text{O}_3(\text{EtO})_{11}(\text{McO})_2]^+$ | 6 | --- | --- | 953.1 | 953.16 |
| B | $[\text{Ti}_4\text{O}_2(\text{EtO})_9(\text{McO})_2]^+$ | 100 | 100 | --- | 799.1 | 799.17 |
| | $[\text{Ti}_4\text{O}_2(\text{EtO})_{10}(\text{McO})]^+$ | --- | 7 | --- | 759.1 | 759.15 |
| C | $[\text{Ti}_4\text{O}_3(\text{EtO})_6(\text{McO})_3]^+$ | --- | 5 | --- | 765.1 | 765.07 |
| | $[\text{Ti}_4\text{O}_3(\text{EtO})_7(\text{McO})_2]^+$ | 14 | 26 | --- | 725.1 | 725.05 |
| | $[\text{Ti}_4\text{O}_3(\text{EtO})_8(\text{McO})]^+$ | --- | 10 | --- | 685.1 | 685.03 |
| | $[\text{Ti}_4\text{O}_3(\text{EtO})(\text{McO})_2]^+$ | --- | 7 | --- | 645.1 | 645.01 |
| D | $[\text{Ti}_3\text{O}(\text{EtO})_8(\text{McO})]^+$ | --- | 4 | --- | 605.1 | 605.17 |
| E | $[\text{Ti}_3\text{O}_2(\text{EtO})_5(\text{McO})_2]^+$ | --- | 23 | --- | 571.0 | 571.06 |
| | $[\text{Ti}_3\text{O}_2(\text{EtO})_6(\text{McO})]^+$ | --- | 8 | --- | 531.1 | 531.04 |
| | $[\text{Ti}_3\text{O}_2(\text{EtO})_7]^+$ | --- | 3 | --- | 491.1 | 491.02 |
| E2 | $[\text{Ti}_3\text{O}_2(\text{EtO})_5(\text{McO})_2(\text{H}_2\text{O})]^+$ | --- | 24 | --- | 589.1 | 589.08 |
| | $\text{Ti}_3\text{O}_2(\text{EtO})_6(\text{McO})(\text{H}_2\text{O})^+$ | --- | 43 | 7 | 549.1 | 549.06 |
| I | $[\text{Ti}_4\text{O}_4(\text{EtO})_3(\text{McO})_4]^+$ | --- | --- | 4 | 730.9 | 730.97 |
| | $[\text{Ti}_4\text{O}_4(\text{EtO})_4(\text{McO})_3]^+$ | --- | --- | 5 | 690.9 | 690.95 |
| | $[\text{Ti}_4\text{O}_4(\text{EtO})_6(\text{McO})]^+$ | --- | --- | 3 | 611.0 | 610.91 |

Table 5.1. MS peak assignments for $[\text{Ti}_6\text{O}_4(\text{EtO})_8(\text{McO})_8]$ fragments in coordinating solvent.

| Core | Peak Assignment | Normalized Peak Intensity | | | Expt. m/z | Calc. m/z |
|------|---|---------------------------|---|------|-----------|-----------|
| | | 30V | 50V | 100V | | |
| | | F | $[\text{Ti}_3\text{O}_3(\text{EtO})(\text{McO})_4]^+$ | --- | --- | 3 |
| | $[\text{Ti}_3\text{O}_3(\text{EtO})_2(\text{McO})_3]^+$ | --- | --- | 13 | 536.9 | 536.96 |
| | $[\text{Ti}_3\text{O}_3(\text{EtO})_3(\text{McO})_2]^+$ | --- | 5 | 7 | 497.0 | 496.94 |
| | $[\text{Ti}_3\text{O}_3(\text{EtO})_4(\text{McO})]^+$ | --- | 8 | 51 | 457.0 | 456.92 |
| | $[\text{Ti}_3\text{O}_3(\text{EtO})_5]^+$ | --- | 3 | --- | 417.0 | 416.90 |
| F2 | $[\text{Ti}_3\text{O}_3(\text{EtO})_5(\text{H}_2\text{O})]^+$ | --- | --- | 46 | 435.0 | 434.92 |
| | $[\text{Ti}_3\text{O}_3(\text{EtO})_4(\text{OH})(\text{H}_2\text{O})]^+$ | --- | --- | 4 | 407.0 | 406.86 |
| G | $[\text{Ti}_2\text{O}(\text{EtO})_4(\text{McO})]^+$ | --- | 4 | --- | 377.1 | 377.06 |
| | $[\text{Ti}_2\text{O}(\text{EtO})_5]^+$ | --- | --- | 4 | 337.1 | 337.04 |
| H | $[\text{Ti}_2\text{O}_2(\text{McO})_3]^+$ | --- | --- | N/A | 383.0 | 382.98 |
| | $[\text{Ti}_2\text{O}_2(\text{EtO})(\text{McO})_2]^+$ | --- | --- | N/A | 343.0 | 342.96 |
| | $[\text{Ti}_2\text{O}_2(\text{EtO})_2(\text{McO})]^+$ | --- | --- | N/A | 303.0 | 302.94 |
| | $[\text{Ti}_2\text{O}_2(\text{EtO})_3]^+$ | --- | --- | N/A | 263.0 | 262.92 |
| H2 | $[\text{Ti}_2\text{O}_2(\text{McO})_3(\text{H}_2\text{O})]^+$ | --- | --- | 15 | 400.9 | 400.99 |
| | $[\text{Ti}_2\text{O}_2(\text{EtO})(\text{McO})_2(\text{H}_2\text{O})]^+$ | --- | --- | 5 | 360.9 | 360.97 |
| | $[\text{Ti}_2\text{O}_2(\text{EtO})_2(\text{McO})(\text{H}_2\text{O})]^+$ | --- | --- | 14 | 321.0 | 320.95 |
| | $[\text{Ti}_2\text{O}_2(\text{EtO})_3(\text{H}_2\text{O})]^+$ | --- | --- | 4 | 281.0 | 280.93 |
| H3 | $[\text{Ti}_2\text{O}_2(\text{EtO})(\text{McO})_3(\text{H}_2\text{O})_2]^+$ | --- | --- | 100 | 378.9 | 378.99 |
| | $[\text{Ti}_2\text{O}_2(\text{OH})(\text{McO})_3(\text{H}_2\text{O})_2]^+$ | --- | --- | 13 | 350.9 | 350.93 |
| | $[\text{Ti}_2\text{O}_2(\text{EtO})_3(\text{H}_2\text{O})_2]^+$ | --- | --- | 3 | 299.0 | 298.94 |

* Possibly obscured by m/z 379 isotope pattern.

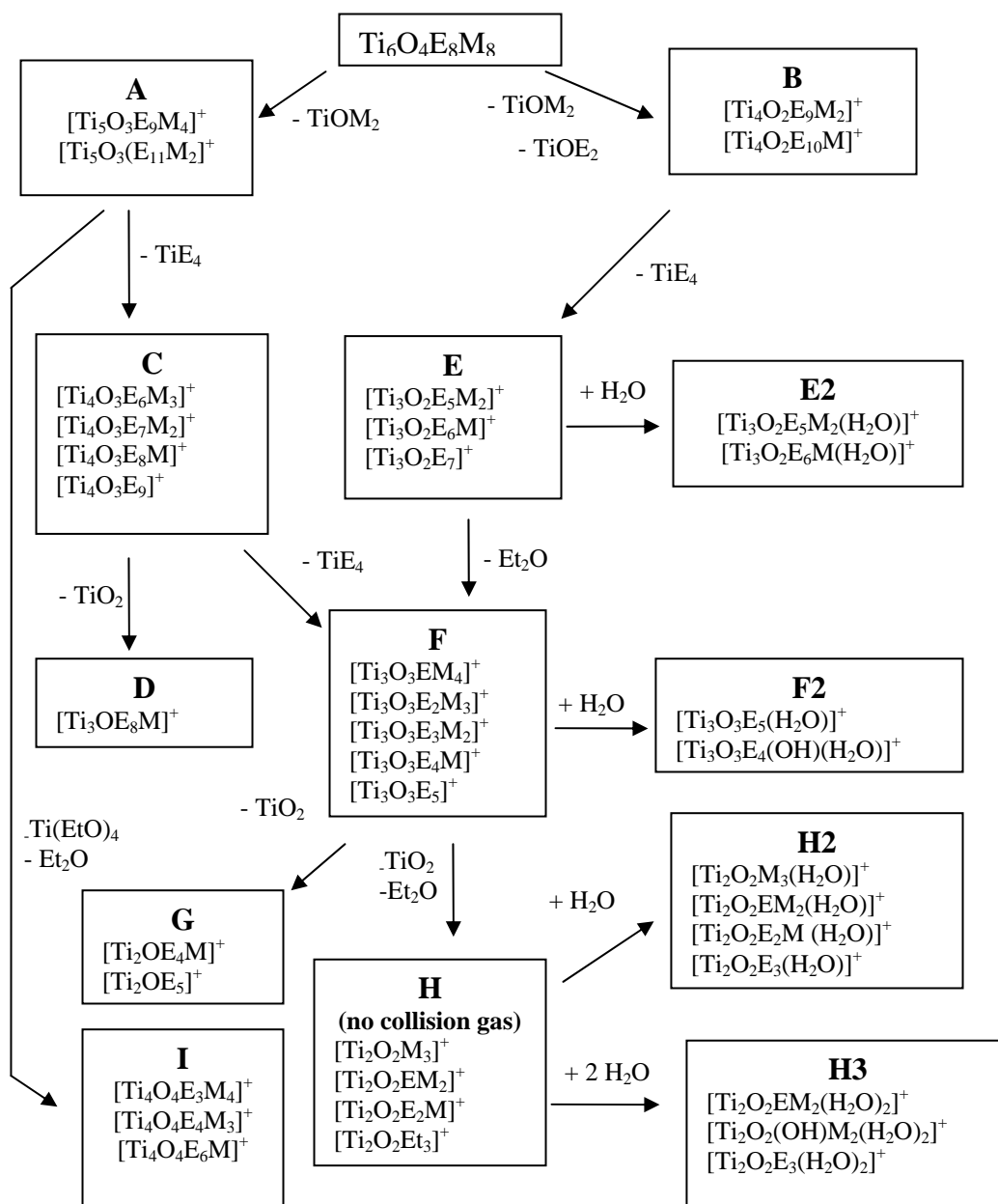


Figure 5.2. Proposed degradation pathway of the parent cluster in ethanol/toluene mixture. Abbreviations: E= ethoxy, M = methacrylate, Et_2O = diethyl ether.

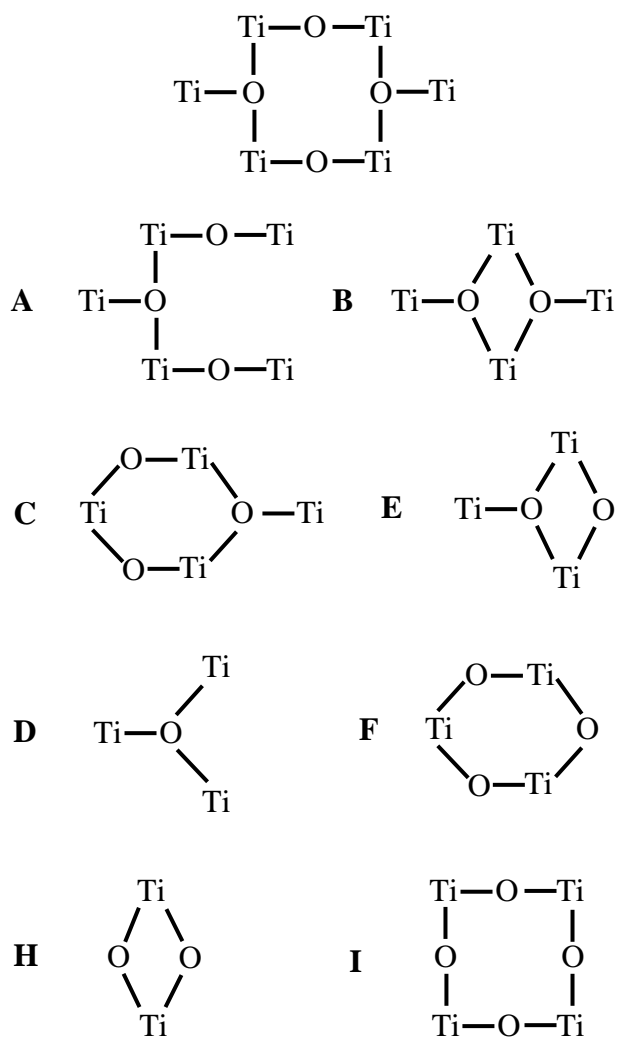


Figure 5.3. Schematic representations of the skeletal arrangements of the Ti and O atoms in the fragmentation product core structures.

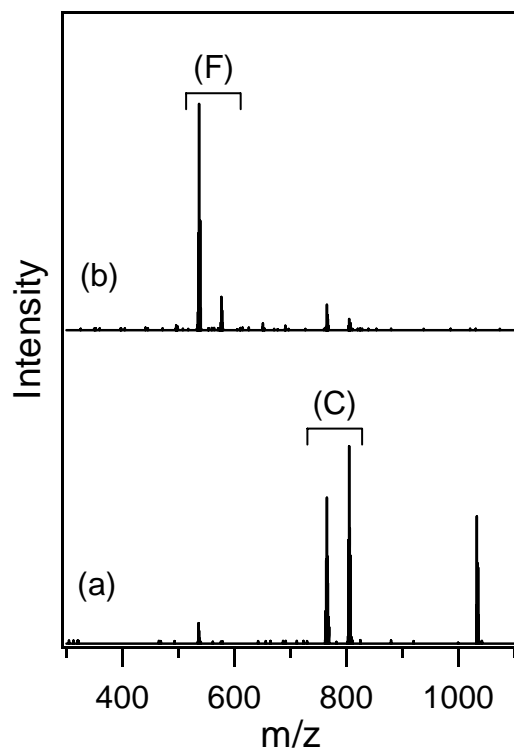


Figure 5.4. Electrospray MS/MS spectra of the parent ion at m/z 1033 using collision energy settings: (a) +20, (b) +40 V.

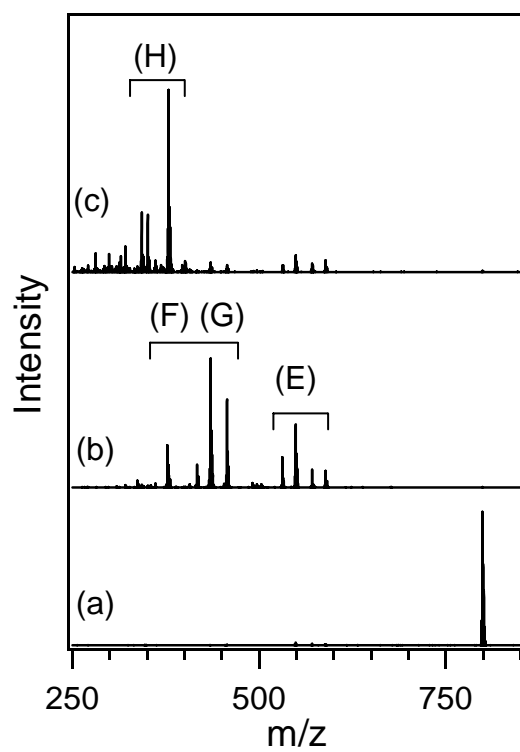


Figure 5.5. Electrospray MS/MS spectra of the parent ion at m/z 799 using collision energy settings: (a) +10, (b) +40, (c) +60 V.

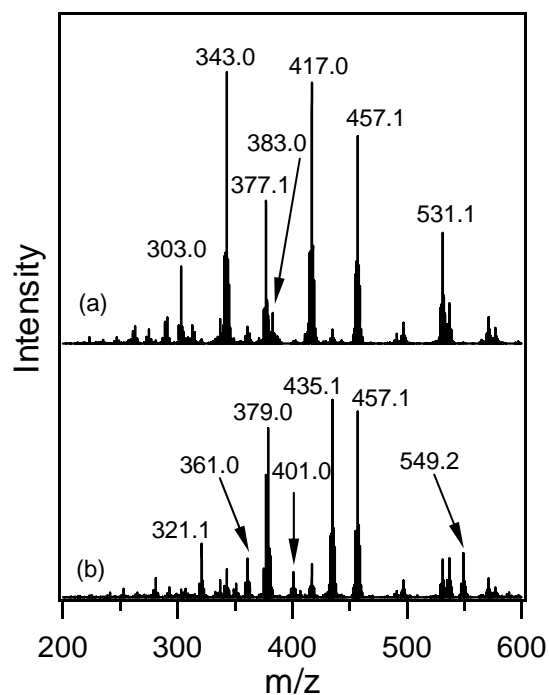


Figure 5.6. Features assigned to E, F, G, and H fragment families with the collision gas off (a), and E2, H2, and H3 families with the collision gas on (b). Spectra collected with the cone voltage set to +100 V.

Table 5.2. MS peak assignments for $[\text{Ti}_6\text{O}_4(\text{EtO})_8(\text{McO})_8]$ fragments in non-coordinating solvent.

| Core | Peak Assignment | Normalized Peak Intensity | | | Expt. m/z | Calc. m/z |
|------|---|---------------------------|------|------|-----------|-----------|
| | | 50V | 100V | 150V | | |
| | | | | | | |
| B+14 | | --- | 5 | --- | 893.0 | |
| | | --- | 13 | --- | 853.0 | |
| | | --- | 8 | --- | 813.0 | |
| B | $[\text{Ti}_4\text{O}_2(\text{EtO})_7(\text{McO})_4]^+$ | --- | 12 | --- | 879.0 | 879.22 |
| | $[\text{Ti}_4\text{O}_2(\text{EtO})_8(\text{McO})_3]^+$ | --- | 25 | --- | 839.0 | 839.19 |
| | $[\text{Ti}_4\text{O}_2(\text{EtO})_9(\text{McO})_2]^+$ | --- | 12 | --- | 799.1 | 799.17 |
| | $[\text{Ti}_4\text{O}_2(\text{EtO})_{10}(\text{McO})]^+$ | --- | 8 | --- | 759.1 | 759.15 |
| B-14 | | --- | 36 | --- | 785.0 | |
| | | --- | 43 | --- | 745.0 | |
| | | --- | 7 | --- | 705.0 | |
| C+14 | | --- | 5 | --- | 659.0 | |
| | | --- | 9 | --- | 619.0 | |
| C | $[\text{Ti}_4\text{O}_3(\text{EtO})_6(\text{McO})_3]^+$ | --- | 19 | --- | 765.1 | 765.07 |
| | $[\text{Ti}_4\text{O}_3(\text{EtO})_7(\text{McO})_2]^+$ | --- | 6 | --- | 725.1 | 725.05 |
| | $[\text{Ti}_4\text{O}_3(\text{EtO})_8(\text{McO})]^+$ | --- | 4 | --- | 685.1 | 685.03 |
| | $[\text{Ti}_4\text{O}_3(\text{EtO})(\text{McO})_2]^+$ | --- | 11 | --- | 645.1 | 645.01 |
| D | $[\text{Ti}_3\text{O}(\text{EtO})_8(\text{McO})]^+$ | --- | 17 | --- | 605.1 | 605.17 |
| | $[\text{Ti}_3\text{O}(\text{EtO})_9]^+$ | --- | 5 | --- | 565.0 | 565.14 |
| E2 | $[\text{Ti}_3\text{O}_2(\text{EtO})_5(\text{McO})_2(\text{H}_2\text{O})]^+$ | --- | --- | 11 | 589.1 | 589.08 |
| | $[\text{Ti}_3\text{O}_2(\text{EtO})_6(\text{McO})(\text{H}_2\text{O})]^+$ | --- | --- | 15 | 549.1 | 549.06 |

Table 5.2. MS peak assignments for $[\text{Ti}_6\text{O}_4(\text{EtO})_8(\text{McO})_8]$ fragments in non-coordinating solvent.

| Core | Peak Assignment | Normalized Peak Intensity | | | Expt. m/z | Calc. m/z |
|------|---|---------------------------|------|------|-----------|-----------|
| | | 50V | 100V | 150V | | |
| | | G | | --- | --- | 9 |
| | $[\text{Ti}_3\text{O}_3(\text{McO})_5]^+$ | --- | --- | 21 | 616.9 | 617.19 |
| | $[\text{Ti}_3\text{O}_3(\text{EtO})(\text{McO})_4]^+$ | --- | --- | 19 | 576.9 | 577.16 |
| | $[\text{Ti}_3\text{O}_3(\text{EtO})_2(\text{McO})_3]^+$ | --- | 13 | 70 | 536.9 | 537.14 |
| | $[\text{Ti}_3\text{O}_3(\text{EtO})_3(\text{McO})_2]^+$ | --- | --- | 78 | 497.0 | 497.12 |
| | $[\text{Ti}_3\text{O}_3(\text{EtO})_4(\text{McO})]^+$ | --- | --- | 11 | 457.0 | 457.10 |
| | $[\text{Ti}_3\text{O}_3(\text{EtO})_5]^+$ | --- | --- | 5 | 417.0 | 417.08 |
| | | --- | 5 | 13 | 551.0 | |
| | | --- | --- | 17 | 511.0 | |
| H | $[\text{Ti}_3\text{O}_4(\text{McO})_3]^+$ | --- | --- | 9 | 462.9 | 463.02 |
| | $[\text{Ti}_3\text{O}_4(\text{EtO})_1(\text{McO})_2]^+$ | --- | --- | 18 | 422.9 | 423.00 |
| | $[\text{Ti}_3\text{O}_4(\text{EtO})_2(\text{McO})]^+$ | --- | --- | 11 | 383.0 | 382.98 |
| | $[\text{Ti}_3\text{O}_4(\text{EtO})_3]^+$ | --- | --- | 4 | 343.0 | 342.96 |
| H2 | $[\text{Ti}_3\text{O}_4(\text{McO})_3(\text{H}_2\text{O})]^+$ | --- | --- | 51 | 480.9 | 481.03 |
| | $[\text{Ti}_3\text{O}_4(\text{EtO})(\text{McO})_2(\text{H}_2\text{O})]^+$ | --- | --- | 100 | 440.9 | 441.01 |
| | $[\text{Ti}_3\text{O}_4(\text{EtO})_2(\text{McO})(\text{H}_2\text{O})]^+$ | --- | --- | 49 | 400.9 | 400.99 |
| | $[\text{Ti}_3\text{O}_4(\text{EtO})_3(\text{H}_2\text{O})_2]^+$ | --- | --- | 5 | 378.9 | 378.99 |
| | $[\text{Ti}_3\text{O}_4(\text{EtO})_3(\text{H}_2\text{O})]^+$ | --- | --- | 11 | 360.9 | 360.97 |
| | $[\text{Ti}_2\text{O}_2(\text{EtO})_2(\text{McO})(\text{H}_2\text{O})]^+$ | --- | --- | 8 | 321.0 | 320.95 |
| | | --- | --- | 11 | 412.9 | |
| | | --- | --- | 12 | 372.9 | |
| I | $[\text{Ti}_4\text{O}_4(\text{EtO})_2(\text{McO})_5]^+$ | --- | 100 | --- | 771.0 | 770.99 |
| | $[\text{Ti}_4\text{O}_4(\text{EtO})_3(\text{McO})_4]^+$ | --- | 79 | --- | 731.0 | 730.97 |
| | $[\text{Ti}_4\text{O}_4(\text{EtO})_4(\text{McO})_3]^+$ | --- | 10 | --- | 691.0 | 690.95 |

Table 5.3 MS peaks collected using the toluene / acetone solvent system at CV = +30 and +50 V. These peaks could not be assigned to molecular species.

| Core | Peak Assignment | Normalized Peak Intensity | | | Expt. m/z | Calc. m/z |
|------|-----------------|---------------------------|-----|------|-----------|-----------|
| | | 30V | 50V | 100V | | |
| | | | | | | |
| | | 4 | --- | --- | 1457.2 | |
| | | 13 | 6 | --- | 1443.2 | |
| | | 24 | 9 | --- | 1429.1 | |
| | | 15 | 6 | --- | 1415.1 | |
| | | 5 | --- | --- | 1407.2 | |
| | | 5 | --- | --- | 1389.2 | |
| | | --- | 11 | --- | 1395.1 | |
| | | --- | 7 | --- | 1390.2 | |
| | | 24 | 40 | --- | 1375.1 | |
| | | 58 | 100 | --- | 1361.1 | |
| | | 54 | 87 | --- | 1347.1 | |
| | | --- | 6 | --- | 1335.2 | |
| | | 8 | 14 | --- | 1321.0 | |
| | | 9 | 21 | --- | 1307.0 | |
| | | --- | 22 | --- | 1161.1 | |
| | | --- | 22 | --- | 1121.1 | |
| | | --- | 28 | --- | 1147.1 | |
| | | --- | 26 | --- | 1107.1 | |
| | | --- | 7 | --- | 1135.1 | |
| | | --- | 12 | --- | 1093.1 | |
| | | --- | 16 | --- | 1053.1 | |
| | | --- | 18 | --- | 1079.1 | |
| | | --- | 20 | 4 | 1039.1 | |
| | | --- | --- | 7 | 999.0 | |

5.4 Discussion.

5.4.1 General Comments

The fragmentation of the parent cluster can be described as a series of substitutions of methacrylate by ethoxy ligands (Δm 40 Da); elimination of ethyl ether (Δm 74 Da); and loss of $[\text{TiO}(\text{EtO})_2]$, $[\text{TiO}(\text{McO})_2]$, and $[\text{Ti}(\text{EtO})_4]$ fragments (Δm 154, 234, 228 Da), which give rise to nine fragment families (A) – (I). In addition fragmentation that results in a 28 Da mass change was observed which is either the result of hydrolysis, or ethylene elimination by the ethoxy ligands. Many of these processes, e.g. ligand exchange, ligand hydrolysis, and ether elimination have been previously observed in the solution chemistry of titanium oxide clusters capped with alkoxy and carboxylate ligands.^{3,4-6} While the structures of the fragment clusters could not be determined, clusters with identical core stoichiometries have been previously observed as intermediates and products of hydrolysis and ligand exchange reactions of titanium alkoxide precursors.⁷⁻¹⁶ These fragments may be important in the hydrolytic formation of TiO_2 sol gel materials.

The production of positively charged species appears to occur exclusively by loss of the negatively charged ethoxy or methacrylate ligands (Δm 45 or 85). None of the MS features were assigned to species formed by proton or metal ion addition as has been observed in ESI spectra of other metallate species. This could be the result of positive ion scavenging by free ethoxy and methacrylate ions in solution.

All the members of a fragment family possess the same titanium oxide core and are produced either by fragmentation of the same larger cluster, or by ligand exchange from another family member. Proof of the former can be found in close examination of MS/MS data on members of the same family. It was found that the mass difference between principal fragmentation products was identical to the mass difference of the ions selected for controlled fragmentation. Thus the larger members of family (C) gave rise to the larger fragments in family (F). Differences between the family members lie in the number of ethoxy, methacrylate, or hydroxy ligands that surround the core.

5.4.2 Mass Spectrum at +30V.

The mass spectrum obtained with the cone voltage set to +30 V represents the ions in solution with minimal fragmentation and contains intense peaks at m/z 799.1 and 725.1, and much less intense peaks at m/z 953.1 and 1033.0. These peaks have been assigned to the species $[\text{Ti}_4\text{O}_2(\text{EtO})_9(\text{McO})_2]^+$ (B), species $[\text{Ti}_4\text{O}_3(\text{EtO})_7(\text{McO})_2]^+$ (C), and species $[\text{Ti}_5\text{O}_3(\text{EtO})_{11}(\text{McO})_2]^+$ and $[\text{Ti}_5\text{O}_3(\text{EtO})_9(\text{McO})_4]^+$ (A), respectively. Species in families (A) and (B) represent the largest fragments of the parent cluster and their assigned chemical composition and structures are consistent with the loss of Ti-O units from the cluster core (Fig. 5.3). No parent ion is observed for this material although a peak at m/z 1301 was observed when using a mass spectrometer equipped with a quadrupole analyzer only that could be assigned to the species $[\text{Ti}_6\text{O}_4(\text{EtO})_6(\text{McO})_8]^+$. This species could be

produced by the elimination of an ethanol molecule from the parent cluster in addition to the loss of an ethoxy ligand to yield the positive charge. Alternatively, the species at m/z 1301 could be the result of a neutral $[\text{Ti}(\text{EtO})_4]$ fragment addition to the species at m/z 1073 which is a member of the (A) family (see discussion at the end of the section). The (A) and (B) cores form independently since (B) does not appear in the tandem mass spectrum of (A) (Fig. 5.4). The core stoichiometries of the two families are consistent with the loss of a $[\text{TiO}(\text{McO})_2]$ fragment from the parent cluster to yield (A) species, and the loss of an additional $[\text{TiO}(\text{EtO})_2]$ fragment to yield (B) species. Both of these transformation processes were accompanied by the loss of a single methacrylate or ethoxy ligand to give the fragment a net positive charge, and the substitution of methacrylate by ethoxy groups. This ligand exchange process may have initiated the degradation of the parent cluster by lowering a core oxygen coordination number and breaking a Ti-O bond in response to replacement of chelating methacrylate ligands by non-chelating ethoxy ligands, as was previously observed in the solution chemistry of similar clusters.¹⁷ The lack of evidence for the conversion of a ligand oxygen to core oxygen atom by ether, ester, or anhydride elimination during the generation of core (A) and (B) species and the inability to assign the MS features to fragments with a different core stoichiometry suggest that the eliminated Ti-O species were part of the core. The Ti_4O_2 core structure of family (B) species¹¹⁻¹² has previously been observed in isolated products of the controlled titanium alkoxide hydrolysis. No reports of the isolation of species with the Ti_5O_3 structure were found. It is likely

that this species is relatively unstable and is easily fragmented by coordinating ethoxy ligands in the analyte solution. This hypothesis is consistent with the relatively low intensity of the MS features attributed to this family, as well as the increase in intensity observed when lower concentrations of EtOH are used in the analyte solution. The appearance of the (C) species is consistent with a loss of a $[\text{Ti}(\text{EtO})_4]$ fragment from the (A) cluster (Figs. 5.2 and 5.4). $[\text{Ti}(\text{OR})_4]$ elimination has previously been observed in the solution chemistry of $[\text{Ti}_x\text{O}_y\text{L}_z]$ type clusters¹⁷ and in MS/MS studies of metal alkoxide clusters.¹⁸ While clusters with the Ti_4O_3 core stoichiometry have not been isolated and characterized, we believe the ring structure shown in Fig. 5.3 is plausible because ring structures have been assigned to the stoichiometries of most of the other stable fragments observed in these experiments.

5.4.3 Mass Spectrum at +50 V.

Increasing the cone voltage to +50 V results in the formation of a (B) family species at m/z 759.1 which is consistent with the substitution of a methacrylate ligand on the 799.1 fragment by an ethoxy ligand. The fragmentation of (B) core species results in the appearance of peaks assigned to the (E) and (E2) fragment families (Fig. 5.5). The stoichiometry of the family (E) species is consistent with the fragmentation of (B) to produce a family with the Ti_3O_2 core structure. Clusters with this core have been observed previously¹⁶ and the structure is shown in Figure 5.3. The structure and mass differences between the two families suggest that the

(B) species undergo $[\text{Ti}(\text{OEt})_4]$ elimination to yield (E) species at m/z 571.0, 531.1, and 491.1 with the general formula $[\text{Ti}_3\text{O}_2(\text{EtO})_{5+n}(\text{McO})_{2-n}]^+$ ($n=0-2$). The (E2) fragment features appearing at m/z 589.1 and 549.1 were assigned to the general formula $[\text{Ti}_3\text{O}_2(\text{EtO})_{5+n}(\text{McO})_{2-n}(\text{H}_2\text{O})]^+$ ($n=0,1$), and share their core structure with the family (E) species. Family (E2) species are most likely the result of water addition to (E) species in the collision cell of the instrument. It is observed that (E2) features disappear and the intensities of the (E) species at m/z 571.0 and 531.1 increase when the collision gas is turned off (Fig. 5.6). Furthermore, the attempt to use the Quadrupole analyzer to select the species at m/z 589.1 for MS/MS analysis resulted in no signal being observed even at the lowest collision energies, while a peak at m/z 589.1 was observed at low collision energies when the species at m/z 571.0 was selected for MS/MS analysis.

Increasing the cone voltage to +50 V also results in the increased fragmentation of the (A) family of clusters. The (A) fragments disappear, while the peaks assigned to the family (C) species increase in number and intensity. We see three additional family (C) species peaks appearing at m/z 765.1, 685.1, and 645.1. These peaks, along with the peak at m/z 725.1, were assigned to species with the general formula $[\text{Ti}_4\text{O}_3(\text{EtO})_{6+n}(\text{McO})_{3-n}]^+$ ($n=0-3$). Because this formula has a limited number of methacrylate ligands, the peak at m/z 605.1 has been assigned to the species produced by TiO_2 elimination from the fragment at m/z 685.1 to yield $[\text{Ti}_3\text{O}(\text{EtO})_8(\text{McO})]^+$ as the lone representative of the (D) family. The structure of

Ti₃O core clusters has been previously determined by several workers⁷⁻⁹ and appears in Fig. 5.3.

The features observed at m/z 497, 457, and 417 were assigned to the general formula [Ti₃O₃(EtO)_{3+n}(McO)_{2-n}]⁺ (n=0-2) and represent the (F) family of fragments. Unlike the fragment families discussed so far, members of the (F) family are observed in the tandem MS analyses of both family (C) and family (E) species. The formation of the family's Ti₃O₃ core is consistent with ethyl ether elimination from core (E) to yield an O bridge between two Ti atoms in Ti₃O₂ followed by a structural rearrangement to form the more stable ring structure (Fig. 5.3).¹⁰ Conversely, core (F) could be produced from core (C) by the elimination of the pendant Ti atom in Ti₄O₃ as [Ti(EtO)₄]. Like the similarly structured family (C) species, the core (F) species at m/z 457.1 appears to undergo TiO₂ fragment elimination to produce a core (G) species at m/z 377.1 which was assigned to the formula of [Ti₂O(EtO)₄(McO)]⁺. This elimination is probably a minor pathway in the fragmentation of (F) species as the peak has very low intensity. Another low intensity (G) peak appears at m/z 337.1 when the cone voltage is set to +100 V. It is interesting to point out that clusters with Ti₂O cores have been observed as unstable intermediates and possible building blocks of more complex titanium oxide species.

10

5.4.4 Mass Spectrum at +100V

As the cone voltage is increased to +100 V, the MS features assigned to family (B), (C), (D), and (E) species disappear from the spectrum, while additional peaks assigned to species (F) appear at m/z 576.9 and 536.9, and are assigned to the general formula $[\text{Ti}_3\text{O}_3(\text{EtO})_{1+n}(\text{McO})_{4-n}]^+$ ($n=0, 1$). We also see the appearance of features at m/z 435.0 and 407.0 assigned to the (F2) fragment family. Like the features assigned to the (E2) family above, these features disappear when the collision gas is turned off indicating that they are the result of water addition in the collision cell. Based on this evidence, the m/z 435.0 species was assigned to the formula $[\text{Ti}_3\text{O}_3(\text{EtO})_5(\text{H}_2\text{O})]^+$. The low intensity peak at m/z 407.0 is probably the result of ethylene elimination from the species at m/z 435.0 in the high energy environment of the ion source.¹⁸

The fragmentation of family (F) continues with the appearance of (H2) fragment family features at m/z 400.9, 360.9, 320.9, and 281.0 assigned to the general formula $[\text{Ti}_2\text{O}_2(\text{EtO})_{0+n}(\text{McO})_{3-n}(\text{H}_2\text{O})]^+$ ($n=0-3$). These features disappear when the collision gas is turned off allowing the observation of core (H) features at m/z 383.0, 343.0, 303.0, and 263.0. These features were assigned to the general formula $[\text{Ti}_2\text{O}_2(\text{EtO})_{0+n}(\text{McO})_{3-n}]^+$ ($n=0-3$). This core could be produced by the elimination of TiO_2 and ethyl ether from (F) family species (Fig. 5.3). It is possible that fragment family (G) is an intermediate in the (H) core formation. Additional spectral features assigned to species having the Ti_2O_2 core and assigned to the (H3) family were observed at m/z 378.9, 350.9, and 299.0. The species at m/z 378.9 and

299.0 which may be the products of the addition of two water molecules to the species at 343.0 and 263.0, respectively. The species at 350.9 which could be the addition of two water molecules to the species $[\text{Ti}_3\text{O}_4(\text{EtO})_2(\text{OH})]^+$ which is the result of an ethylene elimination from the species at m/z 343.0.

We also observe the appearance of peaks at m/z 730.9, 690.9, and 611.0 (Table 5.1). These peaks were assigned to family (I) species having the general formula $[\text{Ti}_4\text{O}_4(\text{EtO})_{3+n}(\text{McO})_{4-n}]^+$ ($n=0,1,3$). Stable species with Ti_4O_4 cores have previously been observed¹³⁻¹⁵ and exhibit the ring structure shown in Figure 5.3. Very weak features assigned to family (I) fragments appear in the tandem MS spectra of family (A), and could be the result of $[\text{Ti}(\text{EtO})_4]$ and ethyl ether elimination from family (A) clusters. Quite unexpectedly, family (I) species do not appear in the tandem MS of family (C) even though the latter would seem to be intermediates in their formation. Perhaps the ethyl ether elimination step cannot take place in the collision cell and only occurs in solution or at the ion source. Another possible assignment of the species at m/z 730.9, 690.9, and 611.0 is to the (E) family of fragments. It is possible that at the high cone voltage, rapid ligand exchange occurs between the fragments in the source resulting the replacement of ethoxy by methacrylate ligands. Low intensity fragments that appear to be the result of this process can be observed if the higher m/z section of the +100 V data is magnified (Fig. 5.1).

There is a possibility that the fragmentation pathway described above leads not to the structures shown in Figure 5.4 but to polymeric species that form by

addition of neutral fragments ($[\text{TiO}_2]$, $[\text{Et}_2\text{O}]$, $[\text{Ti}(\text{EtO})_4]$) to small charged fragments of $\text{Ti}_6\text{O}_4(\text{McO})_8(\text{EtO})_8$ in solution. In this scenario, the cluster would quickly fragment in the coordinating solvent to form the (F) and (G) families of clusters which would gain the neutral fragments necessary to form species with core stoichiometries corresponding to all the larger cluster families. The formation of such polymer like species has previously been observed for titanium alkoxides as well as various polyoxometallate species in solution^{5, 19, 20} and is very likely. These neutral adducts would then be progressively removed from the large species at higher cone voltages to give the appearance of large cluster degradation.

5.4.5 Mass Spectrometric analysis in non-coordinating solvent mixture.

The fragmentation of the molecular cluster in non coordinating solvent (toluene/acetone mixture) results in the production of the same cluster families as the coordinating solvent fragmentation. The only differences between the two systems appear to be the higher cone voltage that is required to observe the fragments in the absence of coordinating solvent, and the ratio of methacrylate to ethoxy ligands on the fragments is somewhat higher when excess ethanol is not used (Table 5.3). The use of a coordinating solvent allows the formation of fragments at lower source voltages. The ability to mimic solution fragmentation by the simple adjustment of instrumental parameters suggests that ESI-MS is a powerful method for the investigation of the solution chemistry of such material intermediates.

The species observed at cone voltage settings of +30 and +50 V could not be assigned (Table 5.4). The species exhibit a titanium isotope pattern with masses in the range of the unfragmented molecular cluster (+30 V) or approximately 100 mass units below the molecular cluster (+50 V). The mass differences between these species are 14 mass units. This mass difference could be the result of ligand exchange or a chemical modification of the ligands.

The species observed when the cone voltage is set to +100 V show a close resemblance to those produced at +30V if 17% ethanol is used as the coordinating solvent. Members of the core (B) (C), (D), (K) and (G) families are definitely present. The clusters have higher masses due to a much lower incidence of methacrylate to ethoxy exchange. Clusters with mass differences of 14 are also present. Increasing the voltage to +150 V results in the production of (G), (H) and (I) core species as well as others. Interestingly the large family of species with mass difference of 28 is not present in the non-coordinating solvent; perhaps the smaller number of ethoxy ligands results in fewer opportunities for ethylene elimination.

5.6 Conclusion

We have studied the fragmentation of the $\text{Ti}_6\text{O}_4(\text{O}_2\text{C}_4\text{H}_5)_8(\text{OCH}_2\text{CH}_3)_8$ molecular cluster in a mixture of toluene and ethanol by ESI-MS and MS/MS. We determined that the observed fragmentation products can be explained by the combination of pathways previously reported in solution and those likely to occur in the higher energy environment of the ESI source or TOF analyzer. A fragmentation

mechanism for the cluster was proposed on the basis of the spectral feature assignments was found to be consistent with the previously reported structures and chemistry of the species involved. MS measurements carried out with the cluster sample dissolved in the non-coordinating solvent mixture of toluene and acetone result in the detection of the same cluster families as observed in the coordinating solvent indicating that energy input in the ESI source closely approximates the effects of a coordinating solvent. This result suggests that ESMS is a potentially useful method for investigating the formation mechanisms of inorganic nanomaterials from molecular precursors.

5.7 References

1. Gaumet, J. J.; Khitrov, G. A.; Strouse, G. F. *Nano Letts* **2002**, *2*, 375-379.
2. Schubert, U.; Arpac, E.; Glaubitt, W.; Helmerich, A.; Chau, C.; *Chem. Mater.* **1992**, *4*, 291-295.
3. Day, V. W.; Eberspacher, T. A.; Klemperer, W. G.; Park, C. W.; *J. Am. Chem. Soc.* **1993**, *115*, 8469-8470.
4. Soler-Illia, G. J. de A. A.; Scolan, E.; Louis, A.; Albouy, P. A.; Sanchez, C.; *New. J. Chem.* **2001**, *25*, 156-165.
5. Stenou, N.; Kickelbick, G.; Boubekeur, K.; Sanchez, C.; *J. Chem. Soc. Dalton Comm.* **1999**, 3653-3655.

6. Lover, T.; Henderson, W.; Bowmaker, G. A.; Seakins, J. M.; Cooney, R. P. *J. Mater. Chem.* **1997**, *7*, 1553-1558.
7. Barkley, J. V.; Cannadine, J. C.; Hannaford, I.; Harding, M. M.; Steiner, A.; Tallon, J.; Whyman, R. *Chem. Commun.* **1997**, 1653-1654.
8. Mijatovic, I.; Kickelbick, G.; Puchberger, M.; Schubert, U.; *New J. Chem.* **2003**, *27*, 3-5.
9. Boyle, T. J.; Tyner, R. P.; Alam, T. M.; Scott, B. L.; Ziller, J. W.; Potter, Jr. B. G. *J. Am. Chem. Soc.* **1999**, *121*, 12104-12112.
10. Carofiglio, T.; Floriani, C.; Sgamellotti, A.; Rosi, M.; Chiesi-Villa, A.; Rizzoli, C. *J. Chem. Soc. Dalton Trans.* **1992**, 1081-1087.
11. Moran, P. D.; Rickard, C. E. F.; Bowmaker, G. A.; Cooney, R. P. *Inorg. Chem.* **1998**, *37*, 1417-1419.
12. Boyle, T. J.; Alam, T. M.; Tafoya, C.; Scott, B. L. *J. Inorg. Chem.* **1998**, *37*, 5588-5594.
13. Troyanov, S. I.; Gorbenko, O. Yu. *Polyhedron* **1997**, *16*, 777-780.
14. Johnson, B. F. G.; Klunduk, M. C.; O'Connell, T. J.; McIntosh, C.; Ridland, J. *J. Chem. Soc. Dalton Trans.* **2001**, 1553-1555.
15. Willey, G. R.; Palin, J.; Drew, M. G. B. *J. Chem. Soc. Dalton Trans.* **1994**, 1799-1804.
16. Barrow, H.; Brown, D. A.; Alcock, N. W.; Errington, W.; Wallbridge, M. G. *H. J. Chem. Soc. Dalton Trans.* **1994**, 3533-3538.

17. Mijatovic, I.; Kickelbick, G.; Schubert U.; *Eur. J. Inorg. Chem.* **2001**, 8, 1933-1935.
18. Zemski, K. A.; Castelman, A. W.; Thorn, D. L.; *J. Phys. Chem. A* **2001**, 105, 4633-4639.
19. Sahureka, F.; Burns, R. C.; Nagy-Felsobuki, E. I. *Inorg. Chim. Acta* **2002**, 332, 7-17.
20. Deery, M. J.; Howarth, O. W.; Jennings, K. R. *J. Chem. Soc. Dalton Trans.* **1997**, 4783-4788.